SANDIA REPORT
SAND2006-6833
Unlimited Release
Printed October 2006

Analysis of Electromagnetic Scattering by Nearly Periodic Structures: an LDRD Report

Roy E. Jorgenson, Lorena I. Basilio, William A. Johnson, Larry K. Warne, David W. Peters, Donald R. Wilton and Filippo Capolino

Prepared by
Sandia National Laboratories
Albuquerque, New Mexico 87185 and Livermore, California 94550

Sandia is a multiprogram laboratory operated by Sandia Corporation,
a Lockheed Martin Company, for the United States Department of Energy's
National Nuclear Security Administration under Contract DE-AC04-94AL85000.

Issued by Sandia National Laboratories, operated for the United States Department of Energy by Sandia Corporation.

Available to DOE and DOE contractors from
U.S. Department of Energy
Office of Scientific and Technical Information
P.O. Box 62
Oak Ridge, TN 37831

Telephone: (865) 576-8401
Facsimile: (865) 576-5728
E-Mail: reports@adonis.osti.gov
Online ordering: http://www.osti.gov/bridge

Available to the public from
U.S. Department of Commerce
National Technical Information Service
5285 Port Royal Rd.
Springfield, VA 22161

Telephone: (800) 553-6847
Facsimile: (703) 605-6900
E-Mail: orders@ntis.fedworld.gov
Online order: http://www.ntis.gov/help/ordermethods.asp?loc=7-4-0#online

SAND2006-6833
Unlimited Release
Printed October 2006

Analysis of Electromagnetic Scattering by Nearly Periodic Structures: An LDRD Report

Roy E. Jorgenson, Lorena I. Basilio, William A. Johnson, Larry K. Warne
Electromagnetics and Plasma Physics Analysis Dept.

David W. Peters
Applied Photonic Microsystems Dept.

Sandia National Laboratories
P. O. Box 5800
Albuquerque, NM 87185-1152

Donald R. Wilton and Filippo Capolino
Department of Electrical and Computer Engineering
University of Houston
Houston, TX 77204-4005

Abstract

In this LDRD we examine techniques to analyze the electromagnetic scattering from structures that are nearly periodic. Nearly periodic could mean that one of the structure's unit cells is different from all the others - a defect. It could also mean that the structure is truncated, or butted up against another periodic structure to form a seam. Straightforward electromagnetic analysis of these nearly periodic structures requires us to grid the entire structure, which would overwhelm today's computers and the computers in the foreseeable future. In this report we will examine various approximations that allow us to continue to exploit some aspects of the structure's periodicity and thereby reduce the number of unknowns required for analysis. We will use the Green's Function Interpolation with a Fast Fourier Transform (GIFFT) to examine isolated defects both in the form of a source dipole over a meta-material slab and as a rotated dipole in a finite array of dipoles. We will look at the numerically exact solution of a one-dimensional seam. In order to solve a two-dimensional seam, we formulate an efficient way to calculate the Green's function of a 1d array of point sources. We next formulate ways of calculating the far-field due to a seam and due to array truncation based on both array theory and high-frequency asymptotic methods. We compare the high-frequency and GIFFT results. Finally, we use GIFFT to solve a simple, two-dimensional seam problem.

Intentionally Left Blank

Contents

Figures

Tables

Analysis of Electromagnetic Scattering by Nearly Periodic Structures: An LDRD Report

1 Introduction

The goal of this LDRD is to provide the critical computational analysis and design tools for developing the "science" of how Photonic Band Gap (PBG) structures operate so that they can be fielded without resorting to excessive experimental prototyping. Interest in PBG structures has increased in recent years because they have the ability to manipulate light in the optical and infrared wavelength ranges. By intentionally introducing defects in a PBG structure, the optical band gap can be modified, which leads to the possibility of new optical devices. In the remainder of this introduction we will describe the characteristics of a PBG structure, how one is built and some of its applications. We will compare and contrast PBG structures to periodic structures that are common in the microwave domain. We will define some terms useful in describing periodicity and apply these terms to describe some actual PBG structures. Finally, we will describe in detail what this LDRD is about.

1.1 Description of a PBG Structure

A PBG structure is a material that inhibits photon propagation over a narrow band of frequencies regardless of the direction of the propagation. This band of frequencies, borrowing from the terminology of semi-conductors, is known as the "band gap" or "forbidden band". Photons with frequencies outside the band gap propagate through the PBG without attenuation.

The PBG structure is made by periodically changing the material's index of refraction as a function of location. Initially this was done in the microwave regime by simply drilling regularly-spaced holes through a slab of dielectric material. Typically, the period of the PBG structure is on the order of the wavelength associated with the band gap center frequency [1]. An electromagnetic wave with a frequency in the band gap is partially reflected from each change in the index of refraction. The reflected waves add constructively, while the transmitted waves adds destructively causing the total wave to attenuate as it propagates through the material. Waves with a frequency out of the band gap are reflected and transmitted out of phase with each other and do not attenuate. The difficulty is to get this interference to occur irrespective of propagation direction. The solution thus far is to modulate the index of refraction in three dimensions based on the face-center-cubic crystalline structure found in diamond [2].

PBG applications include optical fibers where a PBG material surrounds an inner core. In contrast to conventional optical fibers, where the core has a high refractive index to confine the light by total internal reflection, the PBG material allows the core to be a low index of refraction – even a void – which allows more power and information to be passed through the fiber. In the area of light-emitting diodes, a PBG structure can extract light from the diode with greater than 50% efficiency. Titanium dioxide particles smaller than a micron can self-assemble into a PBG structure. Ordinarily, titanium dioxide is a white pigment used in paint and in making white paper. The PBG structure scatters light coherently and imparts more whiteness for less mass of titanium dioxide. Introducing a defect in a PBG structure traps light and forms a type of electromagnetic cavity. This small cavity can be used to build small nano-scale lasers. Finally, PBG structures also occur in nature in butterfly wings and opals [1].

Microwave engineering also has periodic structures that exhibit band gap behavior. One such structure is known as a frequency selective surface (FSS) [3]. FSS's are used as microwave filters, in radomes and as frequency dependent reflectors for space re-use in reflector antenna systems [4]. In the infrared, FSS's are

used as polarizers, beam splitters and mirrors [5]. It is useful to compare and contrast the PBG and FSS to see if they have any problems in common, and given that they do, if any analysis techniques from one discipline can be applied to the other. As the name implies, the FSS is a surface, usually made of thin, metallic patches (a large modulation of index of refraction) placed periodically on a thin sheet of dielectric. PBG structures, on the other hand, are inherently three-dimensional because of the requirement to have a band gap irrespective of propagation direction. In practice, however, this distinction blurs since, on the one hand, the PBG structure is usually truncated in one of its dimensions to make a slab and on the other hand, several FSS's can be stacked to engineer certain band characteristics, which give it some thickness [6]. Initially, PBG structures were made of dielectric material (or by the removal of dielectric material) to cut down on loss, but this also is not a distinguishing feature since in order to ease fabrication and reduce size, PBG structures are now also being made of metal [5]. Indeed, some of the PBG's fabricated at Sandia are made of tungsten. The main difference between FSS's and PBG structures is that the PBG has a more stringent requirement to be independent of propagation direction. In a reflector antenna application, the FSS may have a bandgap that varies as a function of incident angle, but the surface is placed at a position where the band gap requirements are satisfied. If the FSS is being used in a stealth application, where the incident angle has a greater variation, the FSS must have a more stringent bandgap versus angle requirement, more like a PBG.

PBG structures were initially studied by optical and solid-state physicists, so from an analysis point of view they are approached as optical semiconductors [2], [7], [8]. Even the language of the analysis is that of semi-conductors – so in the first PBG structure, which was created by drilling holes through a dielectric slab, filling the intersection of the holes with a dielectric was referred to as adding a donor defect and slicing through the dielectric between holes was referred to as adding an acceptor defect. In the microwave realm, the periodic structure is viewed as a scatterer of electromagnetic waves. Once the language difficulties are overcome, the analysis techniques are similar to one another in that both are geared toward structures having periods that are approximately equal to a wavelength, albeit wavelengths that are vastly different in size. Until recently, however, the two disciplines seemed to be unaware of each other. In this LDRD we will apply techniques that have been developed in the microwave regime to problems arising in the PBG structures. The tiny wavelength in the PBG regime, however, leads to problems that arise solely because of required tight manufacturing tolerances. These problems don't occur in the microwave world because of its larger wavelength and therefore, haven't been a subject of microwave research. Details will be discussed later.

In order to define some useful terms, Figure 1 shows a portion of a periodic structure, typical of an FSS. We are viewing the FSS looking down the $\widehat{z}$ axis. The unit cell, which takes the form of a parallelogram, is replicated along the lattice vectors $\widehat{S}_1$ and $\widehat{S}_2$ an infinite number of times tiling the entire $z = 0$ surface. Along $\widehat{S}_1$ the unit cells are replicated with a period a. Along $\widehat{S}_2$ they are replicated with a period b. Figure 2 shows a plane wave illumination of the periodic structure. The plane wave is represented by the wave vector $\overrightarrow{k}$, which is defined in terms of the spherical coordinates θ and ϕ as shown. The sets of three black dots at each edge of the periodic structure indicate that it is actually infinite in extent. Although these terms are commonly used to define an infinite structure, they can also be used to describe nearly-periodic surfaces. For example, if the periodic structure were truncated to a finite area, the unit cell could be replicated a finite number of times along the lattice vectors to cover the array. If a defect or seam is present, replicating the unit cell could describe the quasi-periodic area around the defect or seam.

1.2 Examples of PBG Structures

Typical PBG structures are many layers thick, as shown in Figures 3, 4 and 5. The wavelength range of interest for all these structures is between 3 and 15 μm. Figure 3 shows a PBG made by Sandia National Laboratories that consists of five layers of long, square tungsten rods. The cross-section of each rod is 1.2 μm by 1.2 μm and the rods are all approximately 1 cm long. The period of a single layer is 4.2 μm. Each

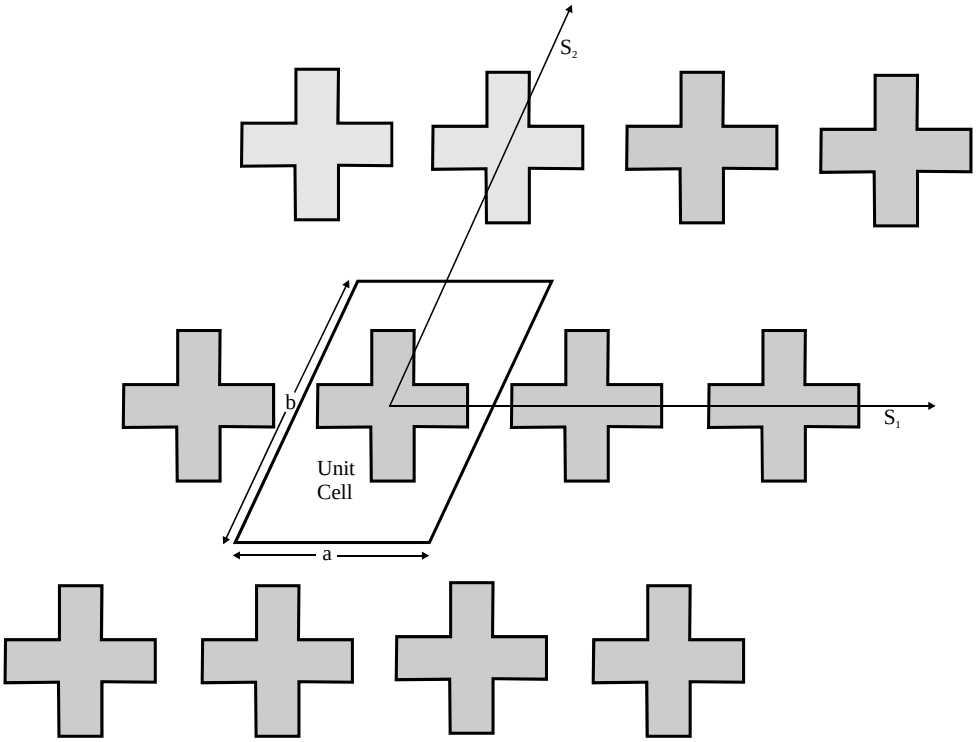

Figure 1. Definition of the unit cell and periodic lattice

layer is rotated 90^0 with respect to its neighboring layers. If we number the layers starting with layer one on the bottom and layer five at the top, layers one and five are identical to each other. Layer three has rods that are in the same direction as layer one, but offset laterally by one half a period. Layers two and four are rotated 90^0 with respect to layer one with layer four offset laterally from layer two by one half a period. This type of PBG is called a logpile. The logpile can be described using the infinite periodic slab parameters defined in Figure 1 as $\widehat{S}_1 = \widehat{x}$, $\widehat{S}_2 = \widehat{y}$, $a = b = 4.2$ μm. Note that the unit cell of the logpile is five layers thick and current continuity must be enforced across neighboring unit cells and between layers.

Figure 4 shows another example of a PBG structure – this one made of rings stacked upon each other. The rings are 4.3 μm in diameter with walls that are 0.75 μm thick. The periodic slab parameters in this case are $\widehat{S}_1 = \widehat{x}$, $\widehat{S}_2 = \widehat{y}$, $a = b = 5$ μm. Figure 5 shows a PBG structure with a "Y" shape stacked upon each other to form the unit cell.

Figures 6 through 12 show the steps needed to fabricate a logpile. The first step, as shown in Figure 6, is to deposit a 1.2 μm layer of SiO_2 on a Si substrate. The SiO_2 layer is periodically etched down to the Si substrate with grooves that are 1.2 μm wide and spaced 4.2 μm away from each other. A single example groove is shown in Figure 7. The third step is to fill all the grooves with tungsten, as shown in Figure 8. The tungsten protrudes above the SiO_2 layer presenting a rough top. Figure 9 shows that the protruding part of the tungsten is ground down to the surface of the SiO_2 layer in a chemical-mechanical polishing process known as "planarizing". This last step is essential because it creates a flat surface that serves as a base for building the next layer. These first four steps create the first layer of logs. The next layer of logs is made by repeating the first four steps, but etching grooves in a direction 90^0 with respect to the first layer. This is shown in Figures 10 and 11. This process continues for each layer until the required number of layers are made. A final step, which is shown in Figure 12, removes the SiO_2 portions and the Si substrate leaving behind the finished tungsten logpile.

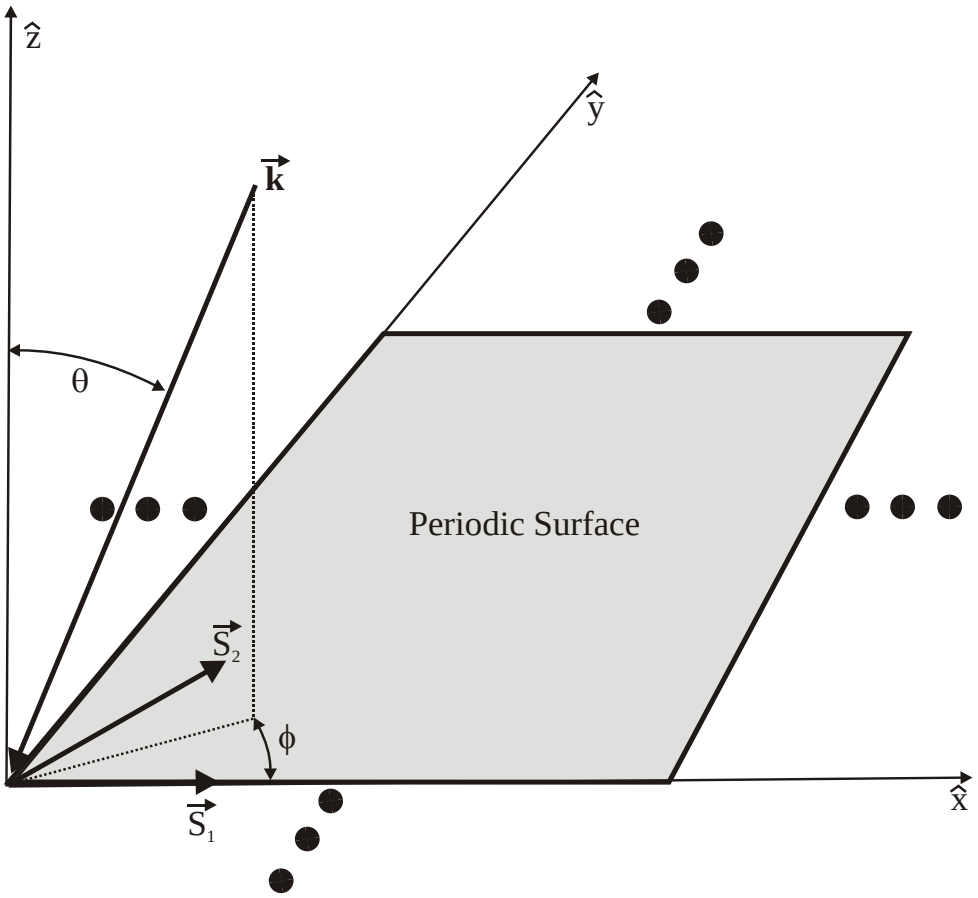

Figure 2. Oblique view of the periodic structure with an incident plane wave

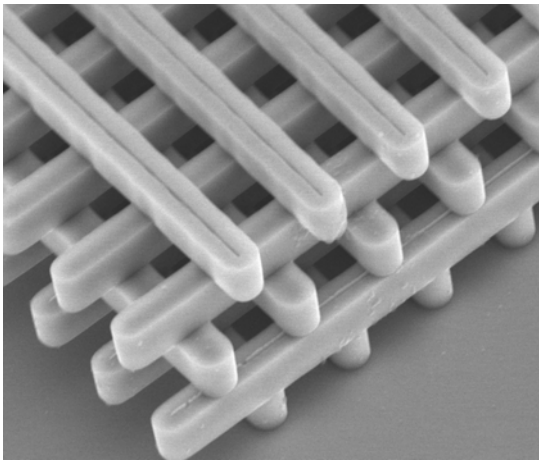

Figure 3. Example of a PBG structure – a five layer logpile

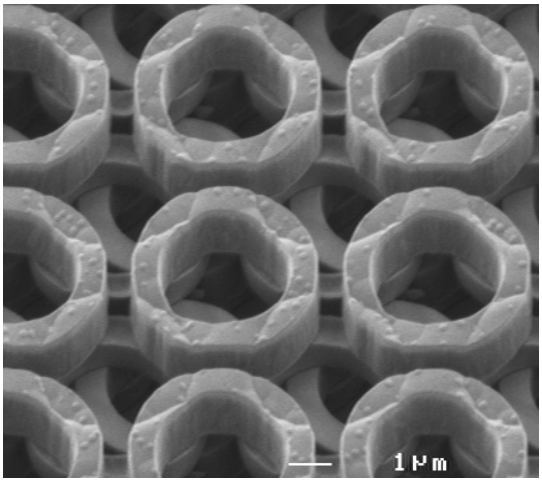

Figure 4. Example of a PBG structure – a thick ring as a unit cell

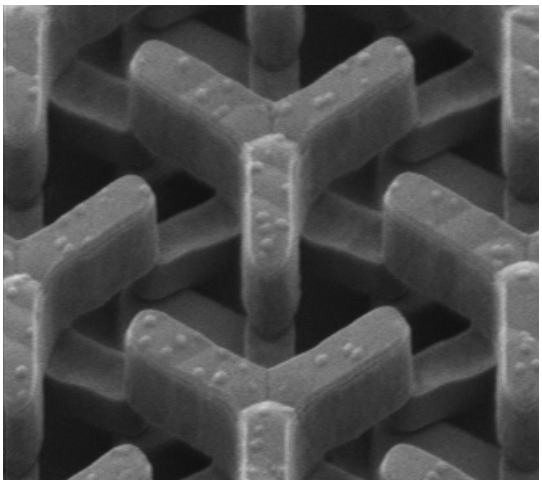

Figure 5. Example of a PBG structure – a "Y" as a unit cell

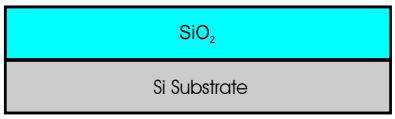

Figure 6. Logpile fabrication, step 1: Grow SiO_2 on a silicon substrate

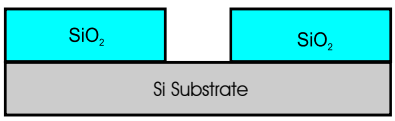

Figure 7. Logpile fabrication, step 2: Pattern and etch the SiO_2

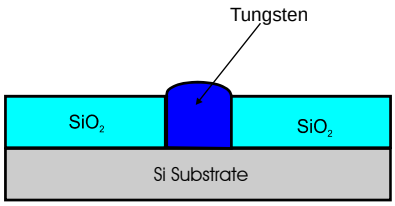

Figure 8. Logpile fabrication, step 3: Fill the etch with tungsten

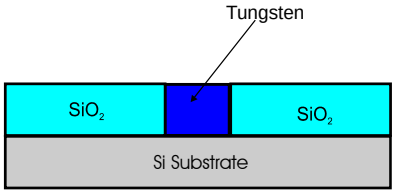

Figure 9. Logpile fabrication, step 4: Planarize

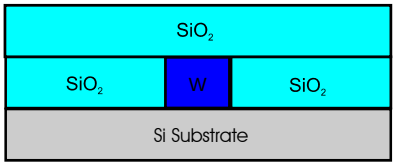

Figure 10. Logpile fabrication, step 5: Grow a SiO_2 layer, pattern 90^0 with respect to the first layer and etch

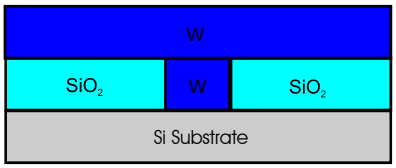

Figure 11. Logpile fabrication, step 6: Fill the etch with tungsten and planarize to create the second layer

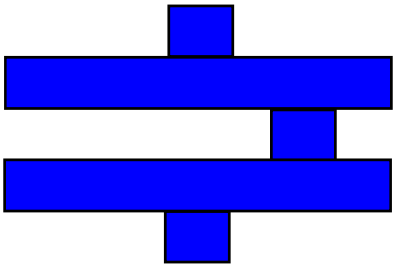

Figure 12. Logpile fabrication, steps 7 through end: Continue until the desired number of layers are achieved then remove SiO_2 and Si substrate leaving the tungsten

1.3 Scope of Work

The characteristics of a PBG structure, such as bandgap frequency, can be engineered by varying the lattice periodicity and by varying the design of the unit cell. We see from the photographs of actual PBG structures (Figures 3 - 5) that on the scale of a few unit cells, manufacturing techniques are sophisticated enough that the PBG structures are in fact locally periodic. By assuming periodicity, we can analyze the performance of a PBG illuminated by a plane wave by invoking the fact that the fields are identical from unit cell to unit cell except for a phase shift dictated by the angle of incidence of the plane wave and the distance between unit cells. If the plane wave were normally incident on the structure (incident along $\widehat{z}$), for example, there would be no phase shift at all and the fields would be identical over each unit cell. In a numerical solution, this fact allows us to devote our unknowns to modeling a single unit cell rather than the entire structure. Generally, if we invoke periodicity on a sub-wavelength sized unit cell and use approximately 10 unknowns per wavelength, we can limit the number of unknowns required to model the problem to less than 100.

In reality, however, the structure is never infinite in extent so the assumption of periodicity is always an approximation. Analyzing the effect that truncation has on the infinite structure is of concern. The PBG structure of interest is limited by manufacturing constraints to be a square patch roughly 1 cm by 1 cm (1000 by 1000 wavelengths if the wavelength is 10 μm). We can put patches together to cover a large object, but because the patches are physically so small this is difficult and leads to other departures from periodicity. Figure 13, which shows four square patch PBG's placed on a flat object, will be used to demonstrate what can happen due to poor placement. We see that the perimeter of the four patches is a straight-forward example of truncation. This type of truncation also occurs in the microwave regime because phased arrays and FSS's are also of finite extent. Extensive work has been done by the microwave community to analyze this type of truncation. Gaps between the patches, which are physically small (on the order of 100 microns), but large in terms of wavelengths, is also considered a truncation. This type of truncation doesn't occur in the microwave regime because the unit cells are physically large enough that gaps can be eliminated. Figure 14 shows the problem of truncation in greater detail.

If two neighboring patches are brought to within a half a wavelength of each other, they can form a seam. In general, a seam occurs when the characteristics of the unit cell – size, contents or both – change from one region to another. If two identical patches are carefully butted against each other so that the unit cells align, the periodicity is maintained and no seam is formed. If, however, the two identical patches are misaligned, as shown in Figure 15, a seam is formed. The size of the unit cell is the same in both patches, but the shift can be thought of as changing the contents of the unit cell from one side of the seam to the other as shown in Figure 16. Figure 17 shows a seam formed when the size of the unit cell changes thus changing the periodic spacing. If the two patches are brought close enough together, they can overlap as shown in Figure 18. In the microwave regime seams have not been studied at all because the wavelength is large enough that the unit cells can be manufactured identically and are easily aligned to a sub-wavelength tolerance.

Within the PBG patch itself, since the unit cells are physically small, unintentional defects can occur in the lattice due to manufacturing mistakes, again breaking the periodicity. Defects can also be introduced intentionally to modify the scattering characteristics of the PBG structure. If defects are introduced along a line, as shown in Figure 19, this is known as a line defect, while a single, isolated defect, as shown in Figure 20 is known as a point defect [9]. Defects can also be introduced for mechanical reasons. For example, if the logpile is made of two different materials each with its own coefficient of thermal expansion, the patch has the potential to bend and de-laminate due to thermally induced stress. One solution to this problem is to introduce periodic cuts in the bars to relieve the stress as shown Figure 21.

Maintaining periodicity becomes even more difficult when the PBG patches are applied to a non-planar

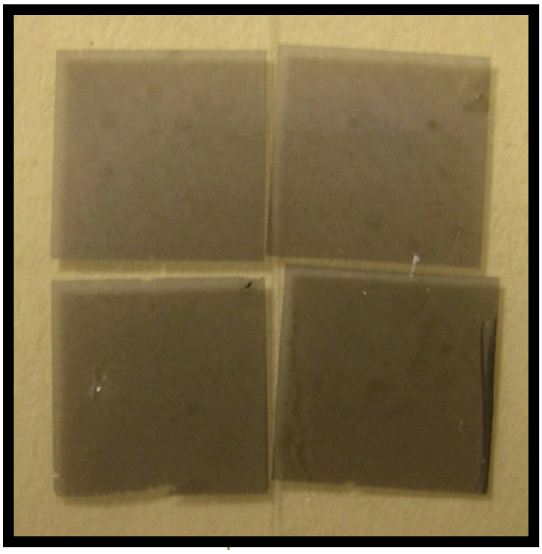

Figure 13. Four logpile PGB patches covering a flat surface

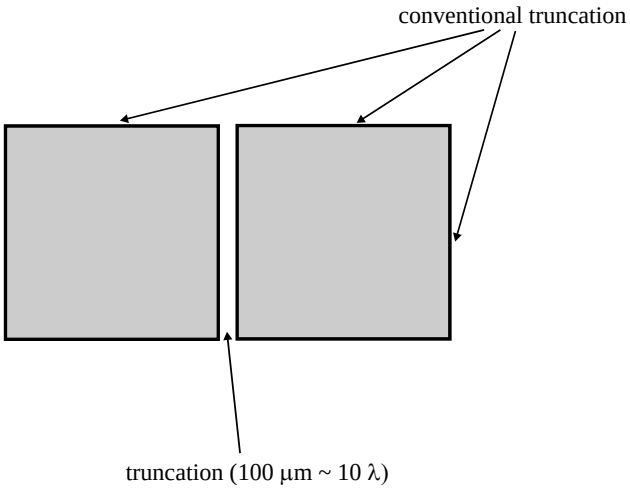

Figure 14. Truncation of periodic structures

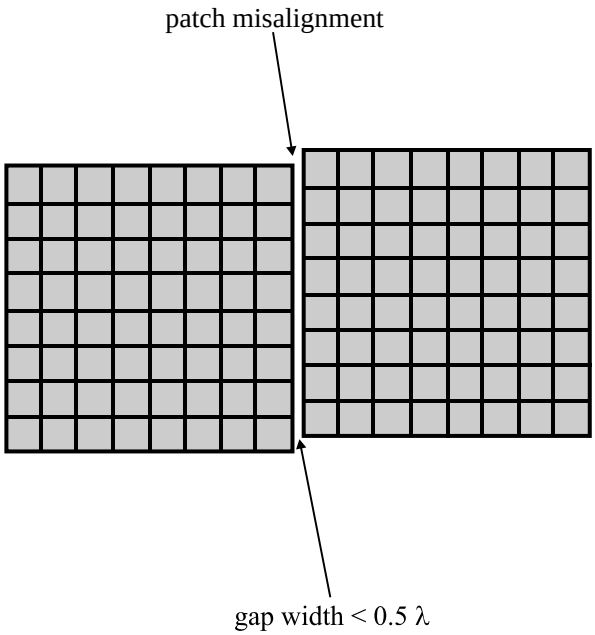

Figure 15. Seam formed by misalignment of two patches

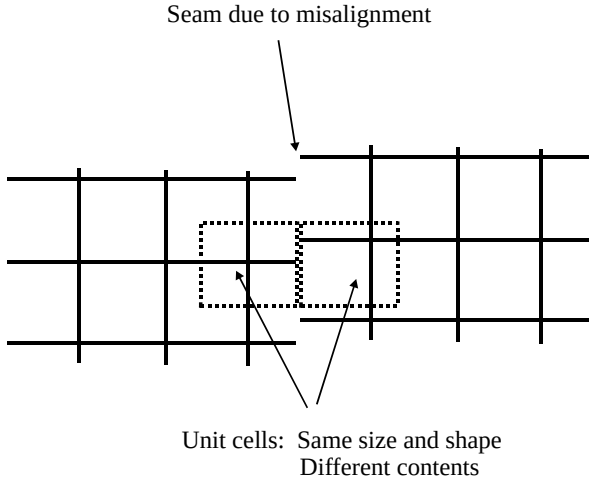

Figure 16. Detail of misalignment

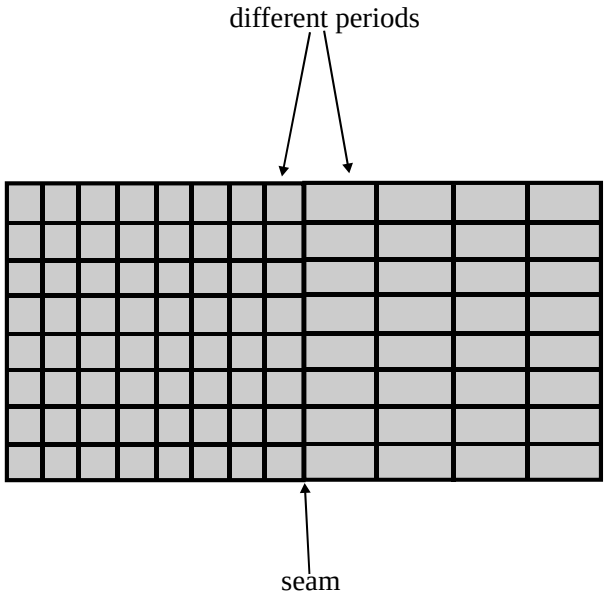

Figure 17. Seam formed by a change in period

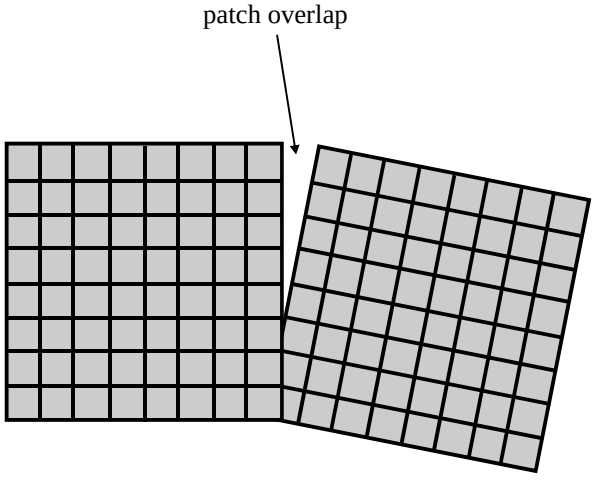

Figure 18. Overlap between two patches

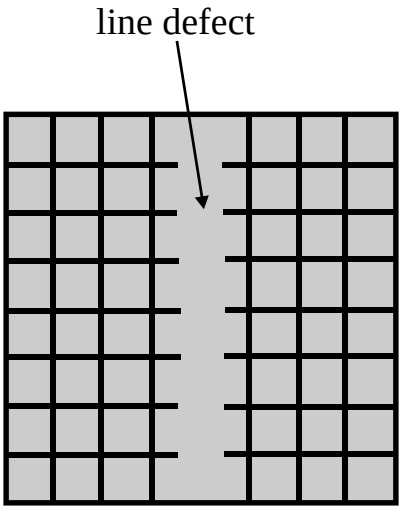

Figure 19. Line defect

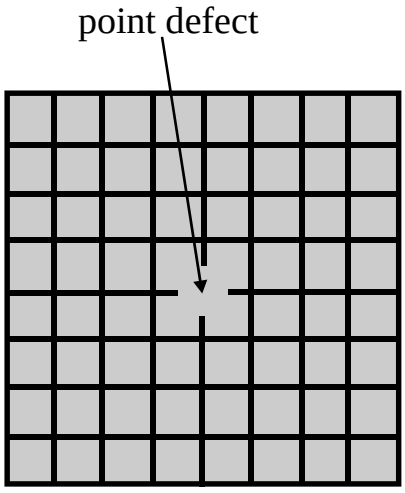

Figure 20. Point defect

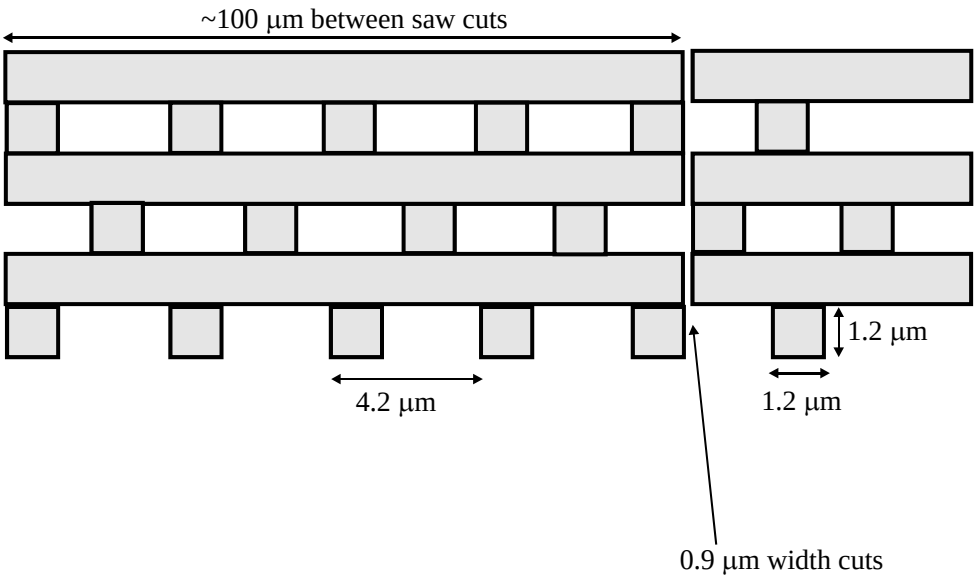

Figure 21. Periodic saw cuts introduced for thermal stability

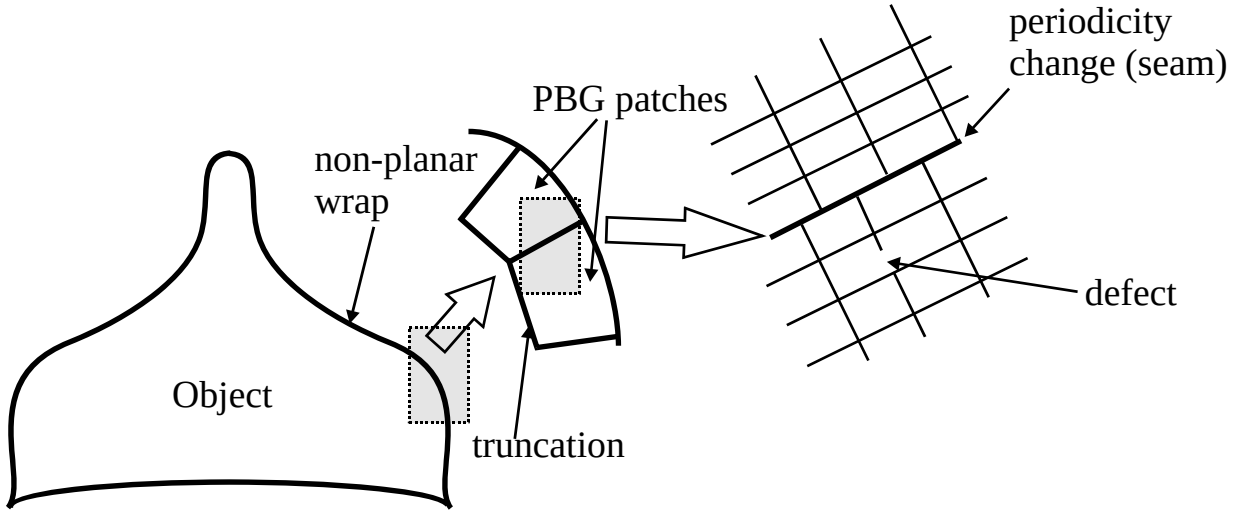

Figure 22. Practical problem leading to seams and defects

surface as shown in Figure 22. The left portion of the figure shows the overall geometry. Since the PBG patches have to wrap around the edge of the object, the lattice associated with a single patch can no longer be described by simple translations of a unit cell and the periodicity is broken. The middle portion of the figure shows the shaded region of the left portion in more detail. Since the patches have to conform to a curved surface, the surface cannot be covered with square patches. The truncation and seams are shown. The right portion of the figure shows in even greater detail the seam and defect. The seam and the truncation should be the most dominant scattering mechanism because they extend over many wavelengths.

A typical PBG patch is 1000 by 1000 wavelengths, which requires approximately 100M unknowns to solve without invoking any special techniques. Our Advanced Simulation and Computing (ASC) experience is that for a boundary-element code, 150K unknowns overwhelm the computer resources available today so there is quite a disparity between the computational resources needed to solve even a single patch and what is available.

In this LDRD we intend to explore hybrid techniques that exploit the fact that the PBG structures are mostly perfectly periodic and depart from this in local regions. We will look at three problems: introduction of a localized defect, truncation of a periodic structure and the seam between two periodic structures. Only truncation has been studied thus far in the microwave regime. We will develop the techniques using a unit cell made of perfect electric conductor (PEC) with no dielectric support, so that we don't have to deal with the effects of surface waves.

2 Previous Work

If we can invoke periodicity we can confine the unknowns to just the unit cell. Analysis of infinite and perfect periodic surfaces are well documented and won't be described here [3], [10]. If we break periodicity in any way: by truncation, by introducing defects, or by introducing seams, we must put unknowns over the entire structure in order to be accurate. The large electrical size of the PBG patches in terms of wavelength, as discussed in the above paragraph, prohibits solving the problem in this way. Thus, in the next two sections we will only review techniques that involve approximations, or rely on certain symmetries to reduce the computational effort.

2.1 Work Pertaining to Defects

Defects are important in PBG structures because they can introduce a small band of frequencies within the forbidden band across which the attenuation is reduced. Defects are purposefully introduced either by cutting a gap in the walls between a single pair of array holes drilled in a dielectric slab (an acceptor defect), or by placing a dielectric sphere in one of the array holes (a donor defect) [7]. These single-point defects are analyzed by introducing a so-called super cell where a unit cell with a defect is surrounded by unit cells without defects [9]. The entire conglomeration of unit cells is essentially treated as a new unit cell with periodic boundary conditions imposed on its exposed faces. The result is that a new period is substituted for the old. A new super cell made of eight original cells, for example, would double the original period putting a defect every other unit cell.

Although the introduction of periodic defects may be necessary to cause the desired bandgap modifications, for this project we are interested in analyzing a true single-point defect where no new periodic cell is invoked. We will do this by modifying a technique developed by Fasenfest, which was originally used to study truncation effects of phased arrays [11]. Fasenfest's technique, the Green's Function Interpolation with a Fast Fourier Transform (GIFFT), depends on the fact that the elements of the phased array, although truncated, conform to a periodic lattice. In other words, the spacing a and b in Figure 1 can not change over the array. The main features of GIFFT are that interactions between sufficiently separated array elements are performed using a relatively coarse interpolation of the Green's function on a uniform grid commensurate with the array's periodicity – thus the need for a fixed periodicity. The Green's function is approximated on the interpolated grid as a sum of separable functions (functions which are a product of a function of the source coordinates and a function of the observation coordinates) which, together with the periodic nature of the array, allows for only near interactions to be computed explicitly and thus lead to an efficient matrix fill. The interpolatory coefficients (representing sampled values of the Green's function) are of convolutional form and therefore an FFT can be used to efficiently calculate the matrix-vector product when using an iterative solver.

2.2 Work Pertaining to Seams

Seams, although potentially important, have not yet been studied in the PBG community. As previously discussed, seams really don't occur in microwave devices so they also haven't been studied by the microwave community. The microwave problem closest to the seam problem is that of truncation. To study both truncation and curvature problems, Cwik reduces the number of unknowns required to grid the entire surface by studying a two-dimensional problem – scattering from a finite array of strips – and notes two approximations that could point the way to solving the three-dimensional problem [14]. For a curved geometry he treats each strip as if it were a member of an infinite, planar, periodic surface with a normal coinciding with the normal of the strip. This approximation accounts for the curvature of the structure, but not for its truncation. The second approximation solves for the currents on strips near the array edge for a small problem and uses these edge currents to replace the edge currents in a larger problem. Ko extends Cwik's work to three dimensions by looking at an FSS that is periodic and infinite in one direction and periodic, but truncated in the other direction [15]. Like Cwik, Ko notes that the surface currents are almost identical for all the patches in the array except near the edge and postulates using the currents from the infinite periodic surface for the interior currents of the truncated surface and solving only for the currents near the edge. Based on these results, attempts were made to use the solution of the infinite, periodic structure in the center region of a finite FSS and to put subdomain unknowns only on the edge region. Difficulty arises from matching the two solutions at the boundary between the center and edge region and how one chooses the location of that boundary [16].

Philips [17] analyzes an FSS embedded in a paraboloidal, dielectric radome. He uses a ray-tracing

method to do the analysis similar to the method known as "Shooting and Bouncing Rays" (SBR) where a number of rays are launched at the mouth of an open cavity, such as a engine inlet, and the rays are individually followed as they bounce throughout the cavity to an output plane [18]. For Philips' case, whenever the ray encounters the curved wall of the radome, the dielectric and the FSS are treated as locally planar and infinite. The rays are traced as they propagate through the dielectric and encounter the FSS multiple times. The rays are tracked in the dielectric slab until they emerge from the other side or decay to where they can be ignored. By separating the FSS interaction from those of the dielectric slab, the curvature is allowed to change for each bounce and the curvature is accounted for more accurately than treating the slab and the FSS as a single unit. Since Philips only accounts for the FSS using a reflection and transmission coefficient for the specular ray (zeroth order Floquet mode) the boundary conditions are only enforced approximately. This paper shows that high-frequency ray techniques can be used for scattering type problems involving FSS's. Since each ray interacts with an infinite structure, no truncation effects are taken into account.

A large number of papers study truncated FSS's by assuming that the current distribution on each unit cell is the same as that of the infinite FSS weighted by an assumed distribution across the truncated FSS. For example, if the weighting is uniform, the current next to the edge of the truncated FSS is identical to the current in the center of the FSS. By making this approximation, the papers bypass the major computational work of the problem and are left with the much easier problem of finding the field due to the known currents. Additionally, they are free to use various approximations to simplify this task even further. We will next discuss some of the papers that use this technique.

Rahmat-Samii examines a dual-reflector antenna system which has as one of its components a doubly-curved and finite FSS subreflector. He uses the same approach as Cwik [14], but on a much more complicated problem [4]. At various points around the curved surface, he first finds the local tangent plane and then calculates the reflection and transmission coefficients of an infinite periodic FSS coincident with that plane. The reflection and transmission coefficients account for the fact that the incident wave from the feed changes orientation with respect to the FSS at different points of the curved surface, but it does not account for the fact that the current on an element near the edge of the FSS will be different from the current on an element near the middle of the FSS due to the presence of the edge. From the reflection and transmission coefficients, Rahmat-Samii finds equivalent currents on a Huygens surface surrounding the FSS and allows the fields due to the currents to radiate toward the main reflector. This step effectively truncates the current and accounts somewhat for the finiteness of the FSS. If this technique were applied to a flat, finite FSS, for example, it would consist of finding the current on a unit cell of a single, infinite FSS and then having this current exist on the unit cells making up the original FSS. The finiteness doesn't affect the current distribution, but does affect the field due to the currents.

Ishimaru solves for the active impedance of a finite array of dipole elements with progressive phasing by assuming that the current on each array element is identical except for a weighting coefficient [19]. The current on the elements are weighted by an aperture distribution function across the entire array. Through use of the Poisson Summation formula, which converts a spatial sum to a sum of Fourier transforms, and using a spatial Fourier transform to represent the impedance in terms of the impedance of an infinite array, the active impedance is expressed as a convolution between the impedance of the infinite periodic structure and the Fourier transform of the aperture distribution. The aperture distribution can theoretically be any function, but the examples all use a uniform distribution. The convolution integral is sampled at a point dictated by the element-to-element phasing.

Carin looks at the scattering from a finite array of strips [20]. After making the approximation that the current on each unit cell is identical except for a phase shift, he finds the expression for the scattered field in terms of an inverse Fourier transform of a spectral domain Green's function and the current in the spectral domain. He separates the rapidly varying part of the spectral domain Green's function from the slowly varying part and evaluates the resulting integrals asymptotically to obtain three contributions to

the far field. Two sources correspond to cylindrical waves emanating from the points where the array is truncated corresponding to edge diffraction terms from the geometric theory of diffraction (GTD). The third term is identical to the field scattered from an infinite array of strips expressed in terms of Floquet harmonics. This is an example of the simplification made possible by additional approximations. Instead of adding the contribution of each element to obtain the field, the field is calculated in the high frequency limit by merely adding three terms.

Capolino expands on Carin's work by calculating the scattering due to a half plane of periodic elementary electric dipole elements [21]. Capolino assumes that the current on each dipole is identical except for a phase shift imposed by the incident wave. He manipulates the expression for the electric field due to this known current to be a summation of Floquet modes in the direction parallel to the edge of the half-plane (because this direction has not lost its periodicity) and an integration for the direction perpendicular to the edge of the half-plane. At high frequencies, an asymptotic evaluation of the integral yields a field that is expressed in terms of two contributions: one which is a series of cylindrical waves representing diffraction from the edge and one which is a series of Floquet modes identical to the infinite periodic problem. Since Carin calculates the scattering from strips, his edge contribution is a single cylindrical wave and his center contribution is a single summation over Floquet modes. In Capolino's case, the periodicity in the direction parallel to the edge causes the edge to be the source of a series of cylindrical waves, one for each Floquet harmonic along the edge and the center contribution is a double summation over Floquet modes. Both propagating and evanescent Floquet modes are included. Capolino also looks at the physical implications of this ray interpretation and how the half-plane behaves at various limits, such as near shadow boundaries, scan blind angles and so forth [22]. If the infinitely long edge of the half-plane is truncated, one gets the contributions of three periodic edges and the contribution of two vertices in addition to the contribution of the center [23]. Thus the ray description of a rectangular, truncated periodic structure consists of nine contributions: an infinite periodic contribution from the center, four cylindrical wave contributions from the edges and four spherical wave contributions from the vertices.

Prakash solves the truncated FSS by first windowing the plane wave excitation of an infinite FSS so that only the truncated portion is illuminated [24]. This means that the incident field is expressed as an integral of a plane wave spectrum and the infinite FSS must be solved for each plane wave. This also isn't equivalent to a truncated FSS because the scattered field due to the elements of the infinite FSS outside the footprint of the windowed field will still interact with the elements just inside the footprint. Secondly, Prakash calculates the electric and magnetic currents on a Huygens surface surrounding the finite FSS and calculates the far field due to these currents. Like for Rahmat-Samii, this step effectively truncates the currents. This paper is an attempt to bring in additional information about the current distribution across the finite FSS. Rather than assume a current distribution (usually taken to be uniform), Prakash windows the incident field and calculates the distribution. Then he truncates the distribution like all the others.

The next group of papers are attempts to improve the knowledge of the current distribution. In these papers the researchers start with the solution of the infinite FSS then calculate the difference current between the actual and the infinite FSS current. We will use these methods later in Section 4.1 to scope how much the current near a seam varies from the infinite FSS current. Figure 23 shows some definitions that are useful in the discussion that follows. We have two areas A and A^* that together make up an infinite periodic surface. A covers the truncated periodic surface that we are interested in solving, while A^* covers the remaining part of the infinite periodic surface.

Munk examines plane wave scattering from an array of dipoles periodic and infinite in one direction and periodic, but finite in the other direction [29]. Although this paper is not focused on the method of solving a truncated array, he describes the solution as first finding the currents on the unit cell of an infinite array ($A \cup A^*$ in Figure 23). He then adds two semi-infinite arrays of these known currents (but in the negative direction to the original currents) in the area outside the original finite array (A^* in Figure 23) cancelling the currents in this area. The scattered field due to the semi-infinite arrays acts as a source in

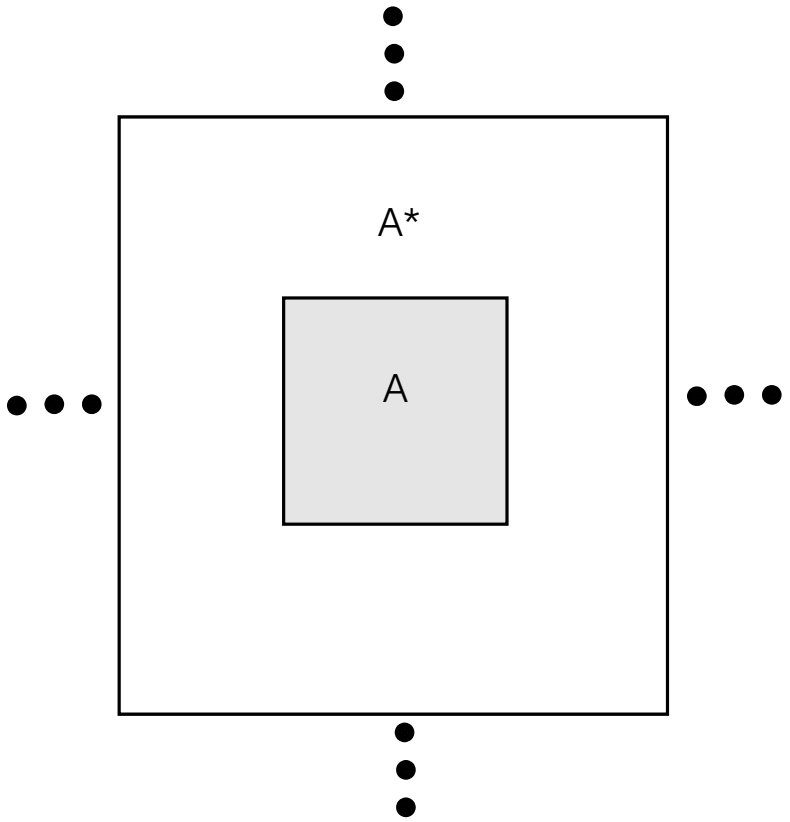

Figure 23. Definition of regions in truncation problems

addition to the original plane wave and modifies the current distribution across the finite array to take the finiteness into account. He solves for the difference current between the actual and infinite array current. Note that although the unknowns are representing a difference current instead of the actual current, the number of unknowns required hasn't changed. In fact, we have added to the work load by needing to calculate the scattered field due to the semi-infinite, known current arrays. Away from the edge of the truncation, where the current approaches that of the infinite array, the difference current is approximately zero, so the unknowns can be expended only over a few unit cells near the edge of the array. Since the current is approximated as existing only around the fringe of the truncated array, it is often called a "fringe current" This approximation is where the computational savings is realized. Munk uses the form of the solution to catalogue the effect of various parameters on the scattered field and is therefore not interested in the computational savings.

Neto solves a truncated array of slits in a ground plane by a method of moments solution of an integral equation where the unknown is the difference between the exact current distribution on the truncated array and the current distribution of the infinite array [25]. Neto follows essentially the same procedure as Munk in setting up the problem, but calculates the field due to the infinite array solution that exists on A^* asymptotically using the techniques developed by Capolino [21]. The slits are assumed to be small in terms of wavelength so that a single pulse basis function can represent the magnetic current of each slit. The difference current is due to the field diffracted from the edges of the array so the current is expanded in terms of complete domain basis functions across the entire aperture. Each complete domain basis function consists of an array of pulses at each slit location modulated by a function based on Capolino's propagating and evanescent asymptotic expansions. Each edge is represented by one propagating and two evanescent modes leading to six unknowns representing the current. Neto extends these techniques to solve a truncated, 3D array, where the radiators are discretized by many subdomain basis functions [26]. The problem is mainly one of book-keeping. The original rooftop basis functions for the infinite array solution need to be grouped to represent the more complicated variation of current across the patch composing the unit cell. Then the complete domain basis functions are formed by multiplying the current on each patch by the diffracted fields from each of four edges and vertices. Although Neto describes the full solution, he applied it to the problem of thin, half-wavelength slots. Cucini implemented Neto's techniques for a truncated array of rectangular waveguides [27].

Civi also solves a truncated array of short dipole antennas each modeled with a single basis function [28]. Unlike Neto and Cucini, Civi solves for the total current on the array. This makes things more difficult because the current is no longer confined to the array edges. In the center of the array Civi expanded in terms of a few complete basis functions based on the form of diffracted fields from the edges and vertices. Since he was working with total currents he also has to include the infinite array Floquet current. On the edges and corners, he expands in terms of subdomain basis functions.

Instead of solving for the currents on a truncated array, Hurst obtains the diffraction coefficient of a truncated FSS numerically [30]. Admittedly Hurst concentrates mostly on solving for the diffraction coefficients of a single large strip. He writes the field as a sum of geometric optics field (scattered from the center portion of the strip) and two cylindrical waves (scattered from the edges of the strip). Each of these contributions has unknown coefficients, but known behavior as a function of distance. He moves his observation point away from the specular direction so he gets contributions only from the edges (two unknowns). He then separately calculates the field due to two strips of different widths giving him two equations to solve the two unknowns. The strips must be wide enough to isolate the two edge scattering centers, but small enough to be solved numerically. He can then use the diffraction coefficients to solve larger problems. He uses this technique to obtain the diffraction coefficient of a 20 element strip array deriving the diffraction coefficients from solutions of 8 and 9 element strip arrays. The use of strips bypasses much of the complexity of a 3d array, but this technique looks promising for obtaining the scattering coefficient of a seam.

3 The Defect Problem

3.1 Description of GIFFT

Since straightforward numerical analyses of large, finite structures (i.e., explicitly meshing and computing interactions between all mesh elements of the entire structure) involve significant memory storage and computation times, much effort is currently being expended on developing techniques that minimize the high demand on computer resources. One such technique that belongs to the class of fast solvers for large periodic structures is the GIFFT algorithm, which is first discussed in [11]. This method is a modification of the Adaptive Integral Method (AIM) [13], which is a technique based on the projection of subdomain basis functions onto a rectangular grid. Like the methods presented in [32]-[35], the GIFFT algorithm extends AIM by using basis-function projections onto a rectangular grid through Lagrange interpolating polynomials. The use of a rectangular grid results in a matrix-vector product that is convolutional in form and can thus be evaluated using FFTs. Although GIFFT differs from [32]-[35] in various respects, the primary differences between the AIM approach [13] and this method is the latter's use of interpolation to represent the Green's function (GF) and its specialization to periodic structures by taking into account the reusability properties of matrices that arise from interactions between identical cell elements. In GIFFT, the GF projections serve as an approximation of the GF across the periodic structure and the projections of the basis functions are then performed by taking an inner product of the basis function with the interpolating polynomials. The GIFFT approach reduces matrix-fill time and memory requirements, since interactions between sufficiently-separated, periodic elements can be carried out using a relatively coarse interpolation of the GF and because only the near element interactions need to be explicitly calculated. The periodic grid can also be used in a 2D or 3D FFT to accelerate the computation of matrix-vector products used in an iterative solver [13] and indeed, has been shown to greatly reduce solve time by speeding the matrix-vector product computation.

Fast multipole methods (FMM) [36]-[38] have also been effectively applied to model large structures. In addition, a general numerical scheme has been introduced in [39] that uses FMM to determine the coupling between periodic cells, with the interior of each cell being analyzed by the finite element method.

The present work extends the GIFFT algorithm to allow for a complete numerical analysis of a periodic structure with defects as shown in Figure 24. Although GIFFT [11] was originally developed to handle strictly periodic structures, the technique has now been extended to efficiently handle a small number of distinct element types. Thus, in addition to reducing the computational burden associated with large periodic structures, GIFFT now permits modeling these structures with source and defect elements. Relaxing the restriction to strictly identical periodic elements is, of course, useful for practical applications where, for example, a dipole excitation may be of interest or, as is often the case for meta-materials, defective elements are introduced in the structure's fabrication process. The main extensions of the GIFFT method compared to [11] are the following:

1. Both periodic "background" and "source" or "defect" elements are now separately defined in translatable unit cells so that in the algorithm, mutual electromagnetic interactions can be computed.
2. The near-interaction block matrix must allow for the possibility of "background-to-source" or "background-to-defect" cell interactions.
3. Matrices representing projections of both "background and source" or "background and defect" subdomain bases onto the interpolation polynomials must be defined and appropriately selected in forming the matrix-vector product.

   Although here we consider a meta-material layer with a dipole-antenna excitation, as per the extended GIFFT algorithm, "defect" elements could be considered as well.

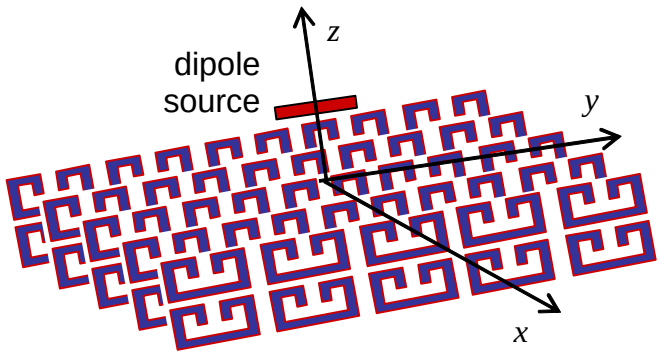

Figure 24. Typical geometry of the problems analyzed. A dipole antenna is placed over a periodic artificial material of finite size. A metamaterial structure is formed using two layers of capacitively-loaded split ring resonators (SRRs).

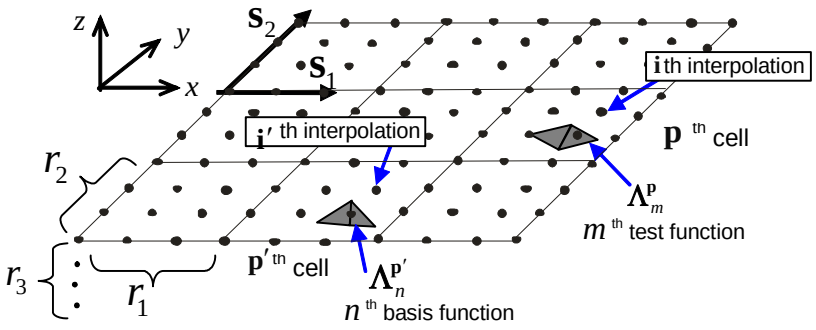

Figure 25. Cell index definitions and arbitrary skew lattice vectors. The periodic grid on which the Green's function is evaluated and sampled is shown superimposed on the cells of the periodic structure. Within a 3D cell, the Green's function is evaluated at $r_1 \times r_2 \times r_3$ points. The lattice vectors $\mathbf{s}_1$ and $\mathbf{s}_2$ shown above are along x and y, but they can, in general, be along arbitrary directions lying in the xy plane.

In [11] the GIFFT method is applied to periodic structures (arrays, in particular) with polygonal boundaries. Only one element of the array is meshed and provided as input, while all other array elements are accounted for by taking advantage of the reusability properties of periodic structures comprising identical elements. The algorithm is summarized in the following paragraphs, where we use a block-matrix notation associated with a periodic block of the array.

Referring to Figure 25, the displacement between the p' th and pth periodic structure cells is $(p_1 - p_1')\,\overrightarrow{s}_1 + (p_2 - p_2')\,\overrightarrow{s}_2$ where $\overrightarrow{s}_1$ and $\overrightarrow{s}_2$ are two arbitrary lattice vectors lying in the xy plane. (We use bold letters to denote both vectors and double indices, and a caret to denote unit vectors.) The vector $\mathbf{r} = \boldsymbol{\rho} + z\widehat{z}$, with $\boldsymbol{\rho} = x\widehat{x} + y\widehat{y}$, is in cell $\mathbf{p} = (p_1, p_2)$ and $\mathbf{r}' = \boldsymbol{\rho}' + z'\widehat{z}$ is in cell $\mathbf{p}' = (p_1', p_2')$. The structural elements within cells $\mathbf{p}$ and $\mathbf{p}'$ are discretized, for instance, using standard Rao-Wilton-Glisson (RWG) [40] basis functions, with primed and unprimed indices denoting source and testing functions, respectively.

Since in this paper we deal only with scatterers in free space, the moment matrix for the original discretized electric field integral equation (EFIE) can be written as

$$\left[Z_{mn}^{\mathbf{pp}'}\right]\left[I_n^{\mathbf{p}'}\right] = \left[V_m^{\mathbf{p}}\right] \tag{1}$$

in an obvious generalization of matrix vector products, and with

$$Z_{mn}^{\mathbf{pp}'} = -\left\langle \boldsymbol{\Lambda}_m^{p}(\mathbf{r})\,;\mathcal{G}^E(\boldsymbol{\rho}-\boldsymbol{\rho}', z, z')\,;\boldsymbol{\Lambda}_n^{p'}(\mathbf{r}')\right\rangle \tag{2}$$

where $\boldsymbol{\Lambda}_n^{p'}(\mathbf{r}')$ and $\boldsymbol{\Lambda}_m^{p}(\mathbf{r})$ are RWG basis and testing functions, respectively. For elements separated by at least one cell, i.e., with $\mathbf{p}$ and $\mathbf{p}'$ that satisfy $\left[\left|p_1 - p_1'\right|, \left|p_2 - p_2'\right|\right] \equiv \left\|\mathbf{p} - \mathbf{p}'\right\| > 1$, we approximate the GF $\mathcal{G}^E(\boldsymbol{\rho}-\boldsymbol{\rho}', z, z')$ via Lagrange polynomial interpolation as

$$\mathcal{G}^E(\boldsymbol{\rho}-\boldsymbol{\rho}', z, z') \approxeq \sum_{\mathbf{i},\mathbf{i}',j,j'} L_{\mathbf{i}}(\boldsymbol{\rho})\,L_j(z)\,\mathcal{G}^E_{\mathbf{i}-\mathbf{i}',j,j'}\,L_{\mathbf{i}'}(\boldsymbol{\rho}')\,L_{j'}(\mathbf{z}') \tag{3}$$

where the indices on $\mathcal{G}^E_{\mathbf{i}-\mathbf{i}',j,j'} \equiv \mathcal{G}^E\left(\boldsymbol{\rho}^{(\mathbf{i})} - \boldsymbol{\rho}'^{(\mathbf{i}')}, z^{(j)}, z'^{(j')}\right)$ denote sampled values of the coordinates and $L_{\mathbf{i}}(\boldsymbol{\rho})\,L_j(z)$ are Lagrange interpolation polynomials defined on the interpolation points within a cell shown in Figure 25 ($\mathbf{i}$ is a double index $\mathbf{i} = (i_1, i_2)$) . It is significant that in the evaluation of the interaction $Z_{mn}^{\mathbf{pp}'}$

between two cells $\mathbf{p}$ and $\mathbf{p}^{'}$, the interpolation scheme generally requires many fewer GF evaluations per cell than the usual case where subdomain interactions are evaluated directly, or even than the usual AIM approach requires. This becomes especially true as the complexity of the geometry within a cell increases or when GFs for layered media are used.

In the GIFFT formulation, the GF interpolation in (3) is used so that the (m,n)th element in the matrix block $Z_{mn}^{\mathbf{pp}^{'}}$ (see (2)) may be represented as

$$Z_{mn}^{\mathbf{pp}^{'}} \approx \widetilde{Z}_{mn}^{\mathbf{pp}^{'}} = -\sum_{\mathbf{i},\mathbf{i}',j,j'} \left\langle \mathbf{\Lambda}_m^{\mathbf{p}}\left(\mathbf{r}\right), L_{\mathbf{i}}\left(\boldsymbol{\rho}\right) L_j\left(z\right)\right\rangle \cdot \mathcal{G}^E_{\mathbf{i}-\mathbf{i}',j,j'} \cdot \left\langle L_{\mathbf{i}'}\left(\boldsymbol{\rho}'\right) L_{j'}\left(z'\right), \mathbf{\Lambda}_n^{\mathbf{p}^{'}}\left(\mathbf{r}'\right)\right\rangle \tag{4}$$

where $\mathbf{p}$ and $\mathbf{p}^{'}$correspond to the testing and source cells and the tilde denotes an approximated block of the impedance matrix. Since a low-order interpolation of the Green's function is not accurate near the source point, Equation 6 is not sufficiently accurate when the cell (index) separation is too small. To avoid this inaccuracy while minimizing the number of interpolating polynomials within each cell, the self-block coupling and that between adjacent neighbor blocks is found by standard Method of Moments techniques (MoM). With good accuracy, the original discretized EFIE in (1) is thus rewritten as

$$\left[\Delta Z_{mn}^{\mathbf{pp}^{'}}\right]\left[I_n^{\mathbf{p}^{'}}\right] + \left[\widetilde{Z}_{mn}^{\mathbf{pp}^{'}}\right]\left[I_n^{\mathbf{p}^{'}}\right] = \left[V_m^{\mathbf{p}}\right] \tag{5}$$

where the block Toeplitz difference matrix $\Delta Z_{mn}^{\mathbf{pp}^{'}} = Z_{mn}^{\mathbf{pp}^{'}} - \widetilde{Z}_{mn}^{\mathbf{pp}^{'}}$ is assumed to vanish for elements satisfying $\max\left[\left|p_1 - p_1^{'}\right|, \left|p_2 - p_2^{'}\right|\right] > 1$, and hence is sparse. We also note that generally $\mathcal{G}^E_{\mathbf{i}-\mathbf{i}',j,j'} = \infty$ when $\mathbf{i} = \mathbf{i}', j = j'$ in $\left[\Delta Z_{mn}^{\mathbf{pp}^{'}}\right]$ and $\left[\widetilde{Z}_{mn}^{\mathbf{pp}^{'}}\right]$. Since, for convenience, Equation 5 is applied over the entire impedance matrix, the infinite values occurring in $\left[\Delta Z_{mn}^{\mathbf{pp}^{'}}\right]$ and $\left[\widetilde{Z}_{mn}^{\mathbf{pp}^{'}}\right]$ when $\mathbf{i} = \mathbf{i}', j = j'$ are replaced with finite values, with the net contribution due to the two terms being equal to zero. To evaluate the matrix-vector product, we note that the product $\left[\Delta Z_{mn}^{\mathbf{pp}^{'}}\right]\left[I_n^{\mathbf{p}^{'}}\right]$ can be performed efficiently since $\left[\Delta Z_{mn}^{\mathbf{pp}^{'}}\right]$ is sparse, whereas $\left[\widetilde{Z}_{mn}^{\mathbf{pp}^{'}}\right]\left[I_n^{\mathbf{p}^{'}}\right]$ is of convolutional form and can be evaluated quickly using a 2D FFT. More specifically,

$$\left[\widetilde{Z}_{mn}^{\mathbf{pp}^{'}}\right]\left[I_n^{\mathbf{p}^{'}}\right] = \tag{6}$$

$$-\sum_{\mathbf{i},,j,j'} \left\langle \mathbf{\Lambda}_m^{\mathbf{p}}\left(\mathbf{r}\right), L_{\mathbf{i}} L_j\right\rangle \cdot \mathbf{MASK}_{\mathbf{i}} FFT_{\mathbf{i}}^{-1}\left[FFT_{\mathbf{i}}\left(\overline{\overline{\mathcal{G}^E_{\mathbf{i},j,j'}}}\right) \cdot FFT_{\mathbf{i}}\left(\overline{\overline{\sum_{\mathbf{p}'}\sum_{n=1}^{N}\left\langle L_i L_{j'}, \mathbf{\Lambda}_n^{\mathbf{p}'}\left(\mathbf{r}'\right)\right\rangle \mathbf{I}_n^{\mathbf{p}'}}}\right)\right]$$

where the double bars over a quantity indicate that its length is extended and appropriately zero-padded so as to obtain a circular convolutional form of vectors of length 2^k for applying the FFT. The term FFT^{-1} denotes the inverse fast Fourier transform and $MASK_i$ is a mask that restricts the result to cells within the structure's polygonal boundary. The degree to which Equation 5 approximates Equation 1 depends on how many elements are chosen to be different from zero in $\left[\Delta Z_{mn}^{\mathbf{pp}^{'}}\right]$ (the strong-interaction matrix) and on how many interpolation points are used for $\left[\widetilde{Z}_{mn}^{\mathbf{pp}^{'}}\right]$. It has been consistently found that setting $\Delta Z_{mn}^{\mathbf{pp}^{'}} = 0$ for interactions between $\mathbf{p}$ and $\mathbf{p}^{'}$ elements such that $\max\left[\left|p_1 - p_1^{'}\right|, \left|p_2 - p_2^{'}\right|\right] > 1$ provides good accuracy.

The GIFFT method has been incorporated into one version of the frequency-domain MoM EIGER code suite [42]. This was done to preserve many of the features of EIGER and to reduce development time.

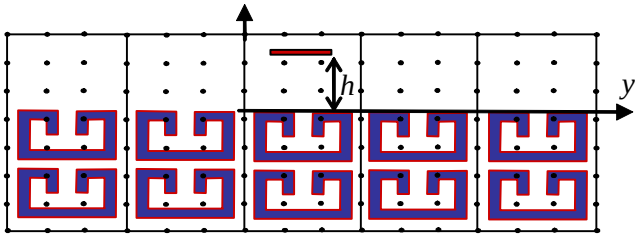

Figure 26. Periodic structure cells for a square lattice, with periods a and b that, for a metamaterial structure, are much smaller than the wavelength. The source is located at the upper right corner of the mother cell $\mathbf{p}' = (0, 0)$, and both exact and interpolated GFs are evaluated in the cell $\mathbf{p} = (1, 1)$. The dots represent Green's function sampling points over a cell cross section.

EIGER has been adapted for efficiently running large array or large FSS's with either identical or varying unit-cell geometry (allowing for the simulation of defects in the periodic structures) with the resulting code being referred to in the following sections as EIGER_GIFFT. GIFFT is presently in the process of being incorporated into the official version of EIGER.

3.2 Modeling Sources Using GIFFT

The GIFFT method requires that only distinct cell geometries be meshed and provided as input to the electromagnetic solver code. For very large structures this has the advantage of condensing the input data and reduces the chance of introducing mesh errors for complex structures. Thus, to model a dipole source over a finite meta-material layer, we provide GIFFT the geometry for two distinct structures. The first consists of the mesh geometry for unit cells making up the "background" meta-material layer. For the structure shown Figure 24, the "background" unit cell can be taken as two split-ring resonators (SRRs) oriented along the $\widehat{z}$ direction. The second geometry description is that of the unit cell containing a single dipole plus two SRR elements (the "source" element). For the GIFFT technique, only the explicit meshing of these two distinct unit cells is required, with a replication of these "mother" cells automatically occurring in the computational part of the algorithm. (For the structure shown in Figure 24, we have one "source" element and 24 "background" elements). It is significant to note that, for this implementation, the GF sampling grid has to be large enough to include both "background" and "source" elements (independently of their location) to form a large brick volume (only the yz plane is shown in Figure 26) where the FFT algorithm is then applied.

3.3 Accuracy of the Green's Function Approximation and Interpolation

To date, the GIFFT method has been applied to array antenna configurations where the distances between the antenna elements, and thus the size of the array cells, are on the order of a half wavelength. A graph of GF interpolation error for such array elements shown in [11] permits the determination of the number of GF interpolation points needed within a cell to guarantee a certain degree of GF approximation. One would expect that meta-material lattices characterized by unit cells much smaller than a wavelength should no pose particular problems since, in general, it is easier to approximate a quasi-static kernel (GF) than an oscillatory one. Hence, the data in [11] should serve as an upper bound for cell sizes that can be approximated efficiently. Furthermore, for cell sizes small relative to a wavelength, the approximation necessarily becomes frequency independent, since quasi-static approximation accuracy depends only on cell dimension to separation ratios.

The precise upper bound of the error for the meta-material geometry treated in this paper, with lattice periods $a = 1.57$ mm and $b = 5.08$ mm, has been checked by evaluating both approximated and exact GFs

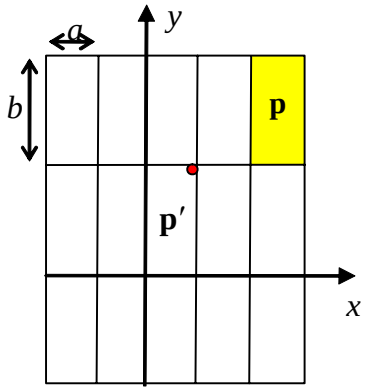

Figure 27. Periodic structure cells for a square lattice with periods a and b that, for a metamaterial structure, are much smaller than the wavelength. The source is located at the upper right corner of the mother cell $\mathbf{p}' = (0,0)$ and both exact and interpolated Green's functions are evaluated in the cell $\mathbf{p} = (2,1)$.

on the cell $\mathbf{p} = (2,1)$ depicted in Figure 27, with height (along the $\widehat{z}$ direction) equal to b, and with a source located at the upper right corner of the mother cell $\mathbf{p}' = (0,0)$. This is a worst-case scenario for our geometry where $b > a$. For a $3 \times 7 \times 7$ grid (along $\widehat{x}$, $\widehat{y}$, and $\widehat{z}$) of interpolation points per block, accuracy in the GF of at least three significant figures is obtained within the cell under consideration. Note that the SRR dimensions are such that they do not extend to the edge of the periodic cell (where we have located the source in Figure 27) and therefore the expected accuracy for our example problem is even slightly better. This check shows that the use of a $3 \times 7 \times 7$ sampling grid is sufficient to assure that $Z_{mn}^{\mathbf{pp}'}$ equals $\widetilde{Z}_{mn}^{\mathbf{pp}'}$ to at least three significant figures when either $\left|p_1 - p_1'\right| > 1$ or $\left|p_2 - p_2'\right| > 1$.

3.4 Analysis of a Dipole Over a High Impedance Surface

3.4.1 Meta-material of Infinite Periodic Extent

An infinite-periodic material made of a two layer array of capacitively-loaded SRRs is studied here for broadside plane-wave illumination propagating along the $-\widehat{z}$ direction. With the exception of the dipole excitation, the finite counterpart of this structure is shown in Figure 24. The SRR geometry is shown in Figure 28 where the dimensions are given by $W = 4.06$, $L = 2.54$, $T = 0.457$, $U = 1.65$, $S = 1.245$, $G1 = 1.02$ and $G2 = 0.508$ (units all in mm). As mentioned previously, the basic unit cell (considered the "background" unit cell in the finite array analysis) consists of two SRRs oriented along the $\widehat{z}$ direction and with the capacitive gaps facing the incoming plane wave. A similar SRR-based meta-material block, of both infinite and finite extent, has been studied by Erentok et al. in [41] and shown to provide good artificial-magnetic-conductor (AMC) performance, with demonstrated agreement between experiment and simulations. While in [41] these SRR elements were embedded in a Duroid substrate of $\varepsilon_r = 2.2$, for a preliminary application of the GIFFT method an air substrate is first considered since it permits use of the FFT in all three dimensions. The periodicity along the x and y directions of the meta-material layer are taken to be 1.57 mm and $W + G1 = 5.08$ mm, respectively.

As is well known, the reflection coefficient associated with such a periodic material is defined by the scattered dominant Floquet wave with phase reference at $z = 0$ (which in this study is coincident with the top of the SRR unit cell). For this portion of the study, a standard MoM code (EIGER [11],[42],[43]) was used to determine the reflection coefficient characterizing the infinite meta-material structure. With the results shown in Figure 29, it is evident that above 12 GHz the magnitude of the reflection coefficient is

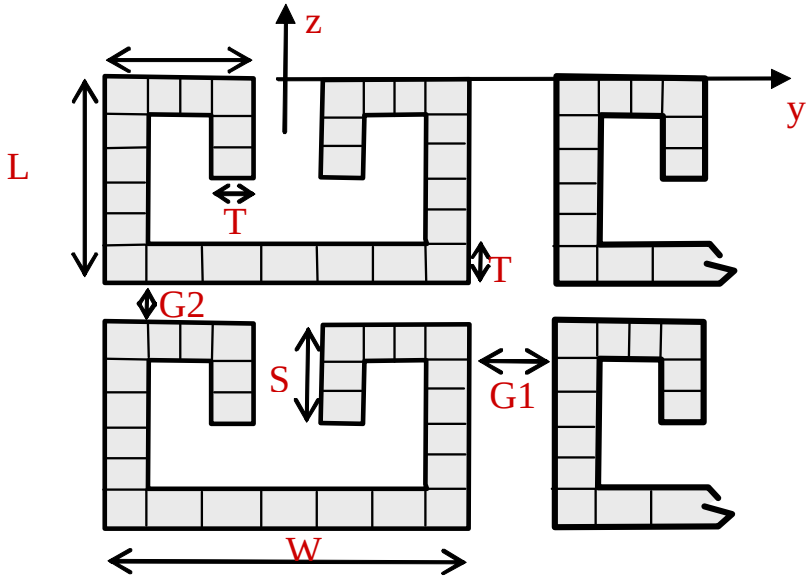

Figure 28. SRR geometry shown with dimensions and the associated mesh.

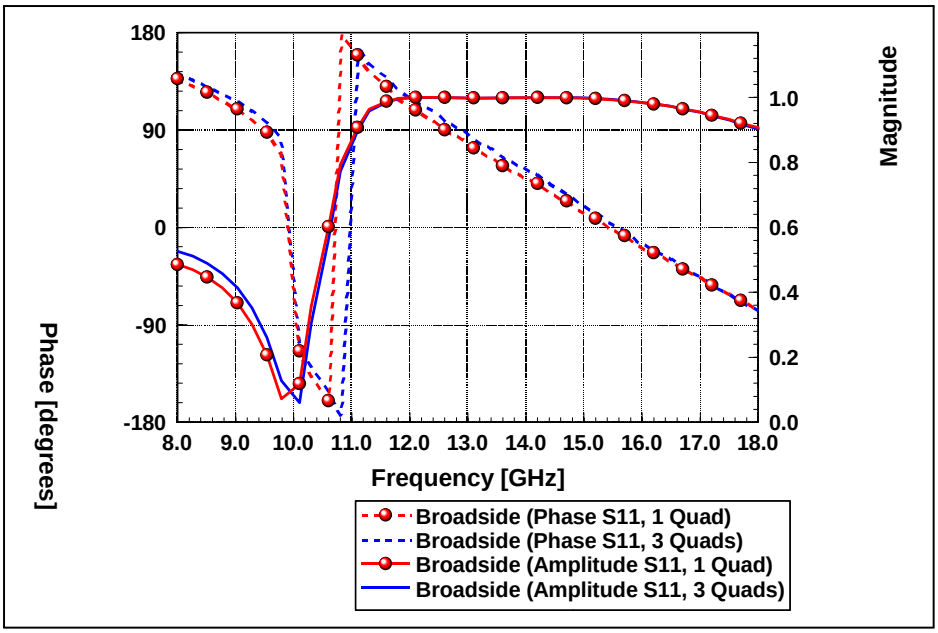

Figure 29. Results characterizing the reflection coefficient for a plane wave impinging from broadside using two meshes with a varying number of quadrilaterals modeling the SRR thickness (see Figure 28). Mesh convergence is demonstrated at $f = 15.7$ GHz, where the magnitude of the reflection coefficient is equal to unity and a zero-crossing of the phase (at a reference plane)

nearly unity, with the zero-crossing of the phase (at the reference plane $z = 0$) occurring at $f = 15.7$ GHz. Thus, at this frequency and for this particular unit-cell orientation, the SRR-based meta-material layer behaves likes an AMC. In [41] it is shown that the orientation between the SRR elements and the incident field has a significant effect on the overall layer performance (an AMC versus an artificial-electric conductor). Figure 29 shows that there is a slight difference in the reflection coefficient when a much finer mesh is used to model the SRRs. In order to ensure that the capacitive effect of the resonators was captured, the number of quadrilateral elements modeling the thickness of the SRRs (T in Figure 28) was increased from one to three. Since very little change occurs near the AMC frequency, mesh convergence is demonstrated.

3.4.2 Meta-material of Finite Extent with a Source Excitation

A short strip dipole is placed at a height h above the top of the upper SRR, as shown in Figures 24 and 26. The flat strip dipole is placed in the xy plane (zero thickness along $\widehat{z}$) and is of width $W = 0.4$ mm in the $\widehat{x}$ direction and length $L = 2.4$ mm along the $\widehat{y}$ direction. It is fed by a delta-gap voltage generator at its center and meshed with three basis functions along its length.

As a first means of assessing the performance of the GIFFT method, a moderate-sized SRR meta-material of 9×7 cells along $\widehat{x}$ and $\widehat{y}$ with two SRRs along the $\widehat{z}$ direction for each cell is analyzed using both the GIFFT technique and a standard Toeplitz MoM method. The strip dipole is placed at $h = 2.5$ mm above the top part of the top SRR. The average current density associated with each unit cell (including both the top and bottom SRR shown in Figure 28), predicted from both methods, is shown in Figure 30 at a frequency $f = 13.8$ GHz. Here the current density is plotted versus the cell number in the array, where the cell numbering in GIFFT proceeds from #1 for the lower leftmost unit-cell and proceeding across from left to right. The strip-dipole placement above the center of the meta-material block (as assumed throughout this study) is, for this structure, located in cell #32. Figure 30 demonstrates good

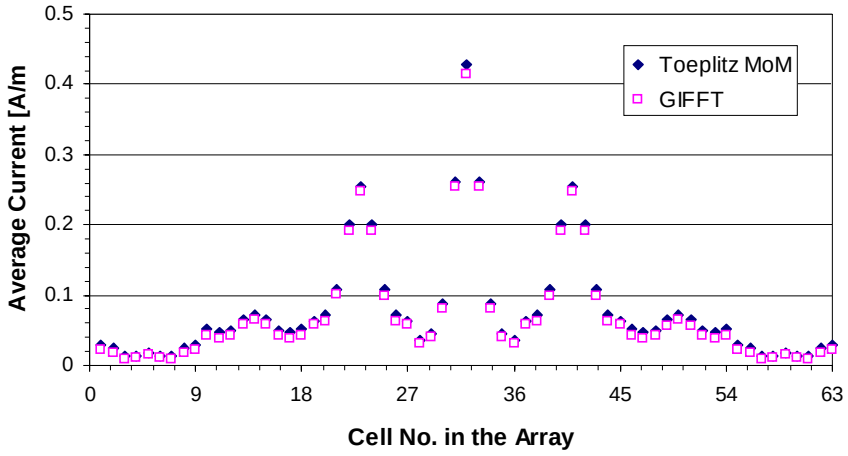

Figure 30. A comparison of the average current densities over each unit cell (including both the top and bottom SRRs) of a 9×7 SRR metamaterial block using a Toeplitz MoM method and the GIFFT technique, at a frequency $f = 13.8$ GHz.

agreement between the predicted current densities; the most obvious difference between the two methods is associated with the respective matrix fill times. On a Pentium M, 1.7 GHz processor, the matrix fill times for the Toeplitz implementation of the standard MoM and the GIFFT method were 29.7 minutes and 1.9 minutes, respectively. Note however, that most of the fill time for GIFFT is associated with the evaluation of $\Delta Z_{mn}^{\mathbf{pp}'}$ (the part that is performed classically). Note also that for even larger structures, the time to evaluate $\Delta Z_{mn}^{\mathbf{pp}'}$ would not change, and the fill time (or more appropriately, the setup time) for GIFFT would scale with the number of GF evaluations. Thus, the GIFFT method demonstrates a significant benefit in matrix fill times. For the moderate problem size considered, a comparison of the matrix solve times for both methods reveals that the GIFFT solve time is slightly slower at approximately 3.3 minutes, versus 1.7 minutes for the Toeplitz MoM technique. It is important to note however, that if N is the number of degrees of freedom, then the solve time for the Toeplitz MoM increases as N^2, the number of operations in the matrix-vector multiplication step of an iterative solution algorithm (we used a BiCGstab solver). GIFFT instead scales approximately as $N \log N$ because of the use of the FFT for each matrix-vector multiplication (see Equation 6).

An analysis of memory requirements for the standard MoM method for the problem considered above (a meta-material layer comprising 9×7 cells with 52 degrees of freedom per cell) shows that each block of $Z_{mn}^{\mathbf{pp}'}$ requires the storage of 2704 complex entries, or a total of about 1.07×10^7 entries for the entire impedance matrix. A Toeplitz storage format reduces this to about 0.77×10^6 entries. In principle, GIFFT requires the storage of only 84 GF samples per cell when we choose a $3 \times 7 \times 7$ interpolation scheme, so that a total of only 2.1×10^4 GF samples are stored. In practice, the memory requirement is slightly higher because of the zero padding to the nearest power of 2 needed to apply the FTT. For the meta-material case with 33×11 cells treated later on, the standard MoM requires the storage of 3.56×10^8 complex entries, while the MoM with Toeplitz implementation requires the storage of 4.17×10^6 complex numbers. Alternately, GIFFT requires the storage of only slightly more than 1.2×10^5 complex numbers.

Figure 31 shows the real and imaginary parts of the input impedance for a dipole located at a height $h = 2.5$ mm from the top of the SRR (as in Figure 26) for a small meta-material sample made of 7×3 (along $\widehat{x}$ and $\widehat{y}$) cells, with two SRR per cell. Although a relatively fine GF sampling grid with $4 \times 8 \times 9$ interpolation points along $\widehat{x}$, $\widehat{y}$, and $\widehat{z}$, has been considered, it produced almost identical results to the $3 \times 7 \times 7$ GF grid, confirming the a priori grid choice based on Section 3.3. Also shown in Figure 31 are the

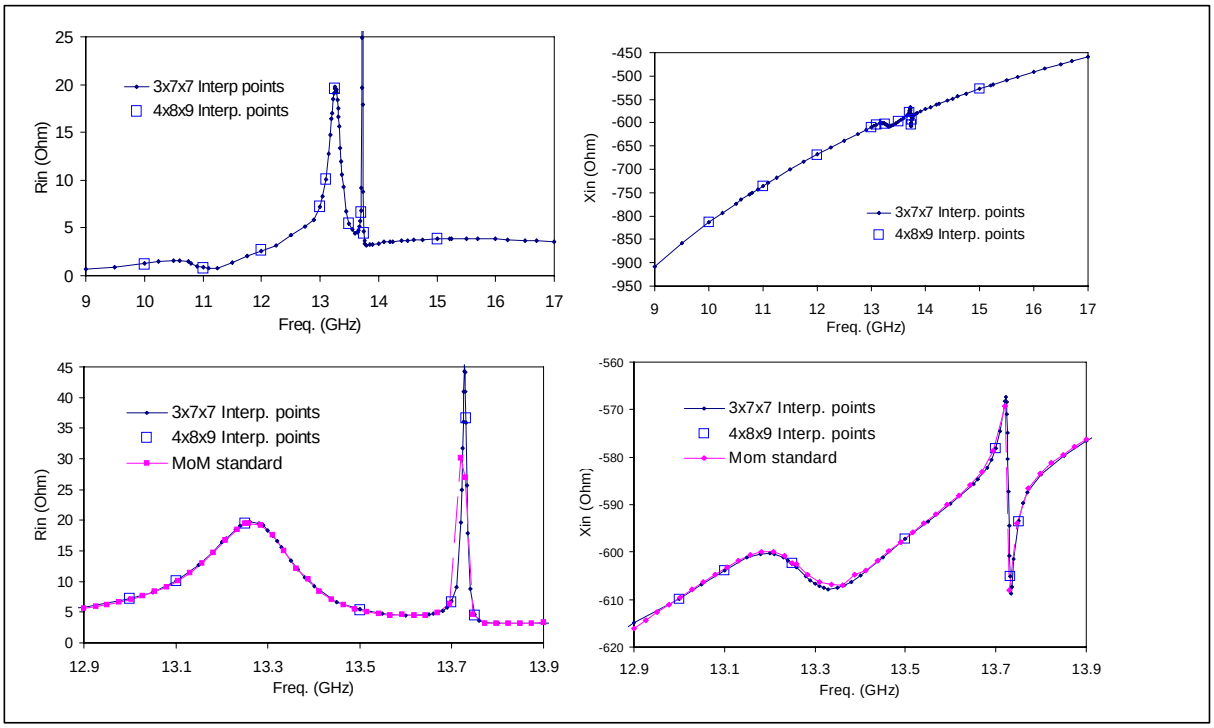

Figure 31. Input impedance for a short dipole above a metamaterial made of 7×3 periodic cells (two SRR in each cell). Two GF sampling grids have been used: $3 \times 7 \times 7$, and $4 \times 8 \times 9$, that provide the same results. A comparison with a standard MoM solution in the frequency range from 12.9 GHz to 13.9 GHz is used to validate the GIFFT method.

input impedance results obtained with EIGER, where good agreement between the methods demonstrates the validity of GIFFT. The two peaks in the real part of the input impedance are due to the material response and not to the height of the dipole as shown in Figure 32 where various dipole heights h have been considered. At a frequency $f = 14$ GHz, both height $h = 2.5$ mm and length $L = 2.4$ mm $= 0.11\lambda$ of the dipole are small compared to the free-space wavelength $\lambda = 21.4$ mm. The dipole input resistance in free space is $R_{in} = 1.06\ \Omega,\ 1.81\ \Omega,\ 2.8\ \Omega$ at the frequencies $f = 10$ GHz, 13 GHz, 16 GHz, respectively, and its reactance follows the characteristic curves in Figure 31, but without exhibiting the resonance-like irregularities around 13.3 GHz.

Figure 33 shows how the size of the SRR substrate affects the input impedance. For the large substrate case we have used the dipole height $h = 2$ mm. The trends of the real and imaginary parts of the input impedance are not changed by the size, though the exact values do vary. The radiation patterns are shown in Figure 34 for the small (7×3) and large (33×11) substrate cases, and in Figure 35 for various frequencies. Figure 35 illustrates how the radiation maximum moves with frequency, despite the very small distance between the small dipole and the ground plane. This behavior is an indication of the phase variation with frequency of the reflection coefficient of the meta-material substrate. From Figure 35, it is also evident that small back lobes in the radiation patterns occur for all the frequencies considered, where beyond about 13.75 GHz the back-lobe level increases with increasing frequency. However, it should be noted that at 13.25 GHz and at lower frequencies (not shown here) the H-plane pattern has a particularly large back lobe compared to the pattern at higher frequencies (the scale is linear). Although the E-plane patterns versus frequency are not included here, these patterns exhibit the same trend.

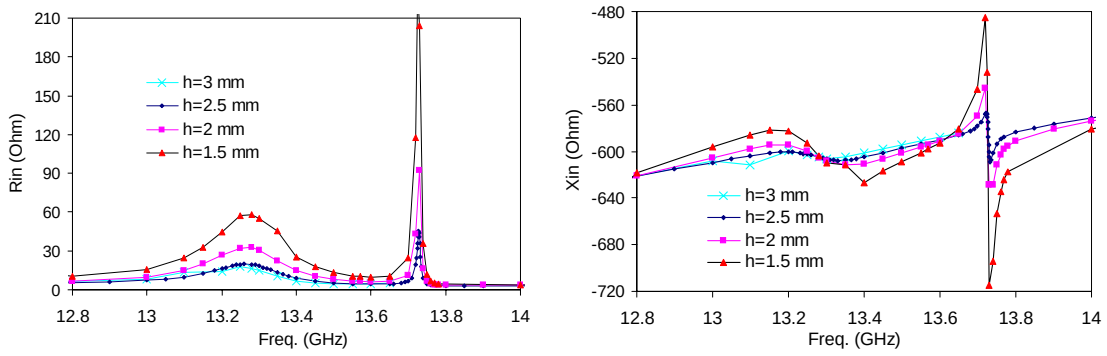

Figure 32. Input impedance of a dipole for various heights h ranging from 1.5 mm to 3 mm, for a small material made of 7×3 periodic cells. The location of the peaks is independent of h showing behavior that is expected of the structure. The input reactance remains largely capacitive due to the short length of the dipole.

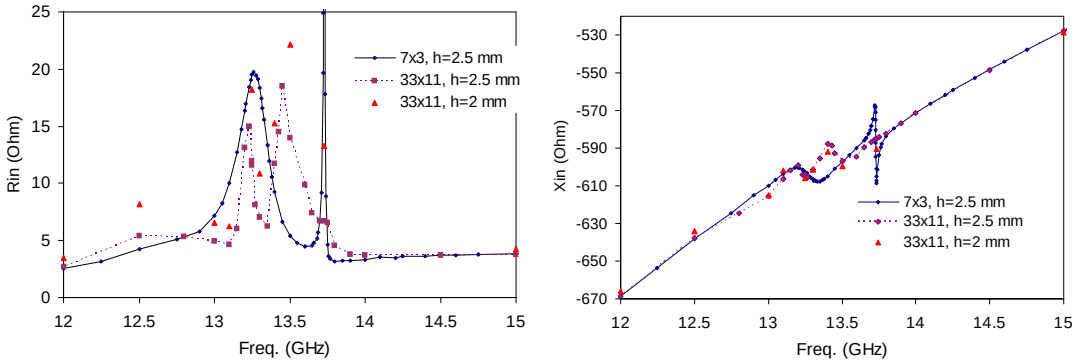

Figure 33. Input impedance for a short dipole located $h = 2.5$ mm above a metamaterial substrate made of 7×3 and 33×11 cells (two SRRs in each cell). Also, the input impedance for a dipole with $h = 2$ mm is shown.

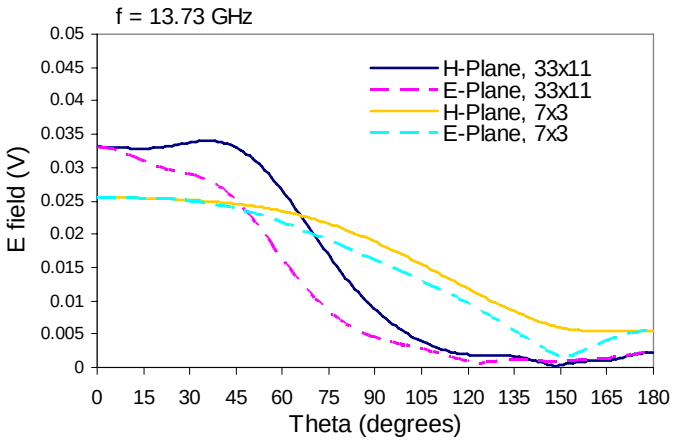

Figure 34. Radiation pattern of a dipole at a height $h = 2.5$ mm, for the small (7×3 cells) and the large (33×11 cells) metamaterial substrate, at frequency $f = 13.73$ GHz.

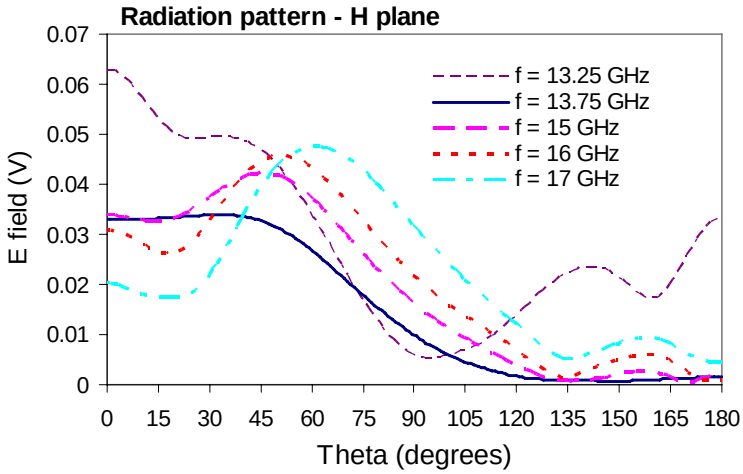

Figure 35. Radiation pattern for various frequencies of a dipole located at $h = 2.5$ mm above a large (33×11 cells) metamaterial substrate.

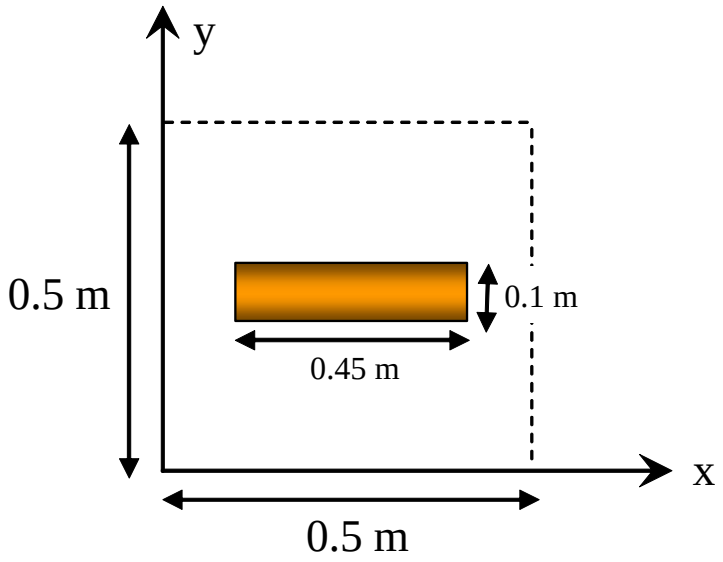

Figure 36. Unit-cell geometry used to form a planar, PEC, strip-dipole array at $z = 0$.

3.5 Analysis of a Horizontal Strip-Dipole Array

In Section 3.4 we viewed a dipole above a meta-material as a defect and performed the analysis of this using GIFFT. This section presents results for a finite, horizontal-dipole strip array that was also analyzed using the GIFFT method. We begin by examining the current at various cuts across the array and comparing it to the current calculated on an infinite array. We then study the effect of a defect caused by rotating one of the dipoles. It should be noted that in the results that follow, the EIGER code, a standard MoM code that has been thoroughly tested, has been used to verify the results.

3.5.1 Problem Description

The unit-cell geometry used in each of the planar arrays examined below is shown in Figure 36. The dipole elements in the array are numbered from left to right beginning with element #1 in the bottom-most, left-hand corner. As an example, the array element numbering for a 3×3 array is shown in Figure 37.

The input file defining the geometry and materials associated with an array element is generated using a normal preprocessor just as if only a single array element was to be simulated. (This information is contained in the .eig file associated with the standard version of EIGER.) As mentioned previously, the EIGER_GIFFT code does not require an explicit meshing of the entire array, but rather relies on a translation of the unit-cell and a Green's function interpolation to compute the results for each individual element. To define the translations and the array geometry however, an additional array input file is necessary for EIGER_GIFFT. A sample input file for a 5×5 square array of horizontal strip dipoles (with the unit-cell shown in Figure 36) is given in Table A. For the case where all elements of the array are not identical, it is possible to modify the array input file to include n types of representative elements (each one explicitly meshed), where the element numbering scheme discussed above can be used to specify the locations of the different elements. (This case is examined in a subsequent section of the report.)

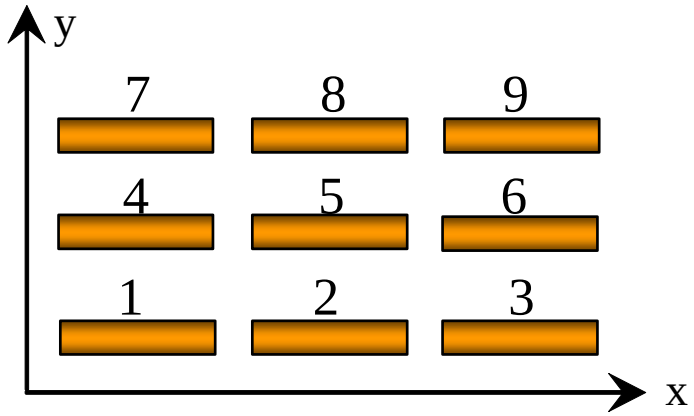

Figure 37. The element numbering scheme for an example 3×3 array.

Input	Input Descriptor
4	number of vertices of the array
0.0 0.0 0.0	The coordinates of the vertices bounding the array, vertex 1
2.5 0.0 0.0	vertex 2
2.5 2.5 0.0	vertex 3
0.0 2.5 0.0	vertex 4
0.5 0.0 0.0	Lattice vector 1 describing periodicity in xy plane
0.0 0.5 0.0	Lattice vector 2 describing periodicity in xy plane
5 5 1	The number of interpolation points to use in the x,y,z direction.
1	Flag - 1=use GIFFT, 0 =use block Toep.
0	Preconditioner type - 0 = block diag 1= all near -1 = none.
0	ArrayFull3DFlag. 0 = no FFT in z. 1 = FFT in z.
0	ArraySameExciteFlag. If 1, all right hand sides will be identical.
0	ArrayPhasedFlag. 0=no phasing added, 1=linear phasing added to RHS
0.0 0.0	The scan angle in theta and phi. This is ignored if ArrayPhasedFlag is 0
1	FastNearFlag. 1 = if using GIFFT, 0 = never use FFT for near field.
0	ArrayPortAnalysisFlag
1	Number of types of array elements in the array
10	Number of meshing elements in array element
1	Background element - this is the predominant element in the array.
0	Number of array elements which are different from the background element

Table A. Array input file for a 5X5 array of identical strip elements.

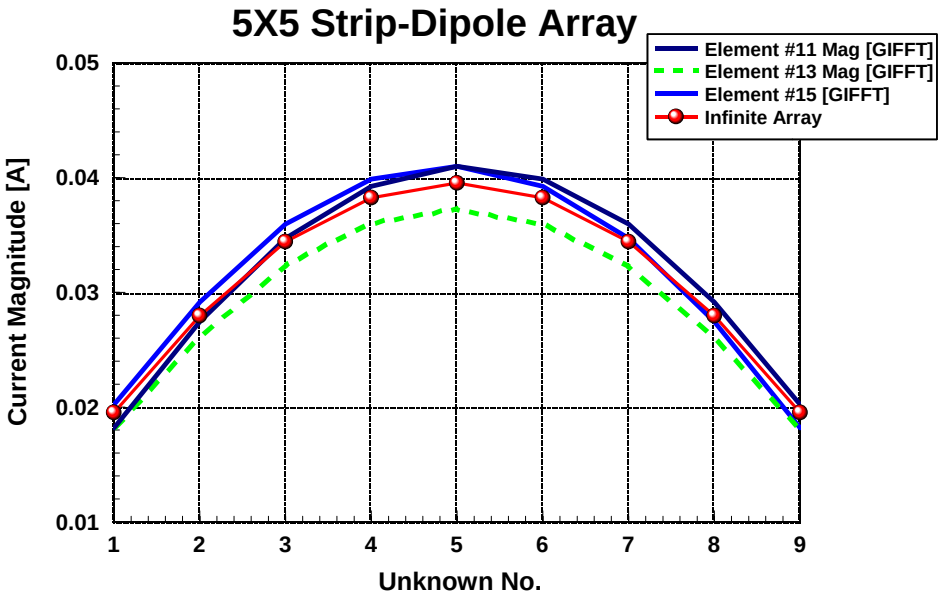

Figure 38. Current distributions for select elements of a 5×5 array.

3.5.2 Array-Current Distributions

We first examine the distribution of current along several strip dipole arrays (for various select strip elements) and compare those to the currents calculated for the array elements in an infinite strip-dipole array. In Figure 38, we show the magnitude of the $\widehat{x}$ directed current on select elements (the middle and two edge elements) in the middle row of a 5×5 array. The current magnitudes are plotted versus the length of the strip in terms of the unknown number, where the individual strips have each been gridded to have ten elements along the $\widehat{x}$ direction and correspondingly, nine unknown current values. From Figure 38, it is evident that the currents corresponding to the edge strips (elements #11 and #15) are larger than the currents on the middle element (element #13). (It is significant to note that GIFFT results were found to be identical to those found using a standard MoM technique.) Furthermore, the current associated with an infinite array of strip dipoles (having the same unit cell dimensions as the 5×5 array) falls between the currents associated with the edge and middle elements. Thus, in this particular case, it appears that the finite-nature of the array is "seen" by each individual element of the array and, as one might expect, the infinite array solution is not yet accurate for any of the strips. Although a 5×5 array is still relatively small, it is being included simply to demonstrate the effects of the edges as the array size increases.

In Figure 39 we show the current distribution for select elements in the middle two rows of a 10×10 strip-dipole array. As observed in the 5×5 array, the currents associated with the edge strips are larger than for the strips in the middle. By examining the two middle rows of the array, we also observe a symmetry in the array results with the currents characterizing the two corresponding strips along a given column being equal (e.g. elements #45 and #55 or elements #41 and #50, etc.) In this case, we find that the array has become large enough so that the truncation of the array is not reflected in the current solutions of all the strip elements. As one might expect, the elements in the middle have currents which agree very closely with that computed for the infinite array.

In order to simultaneously examine the behavior of the currents on the 10×10 array and compare them to the infinite array solution, a contour plot of the currents for each of these cases is presented in Figures 40

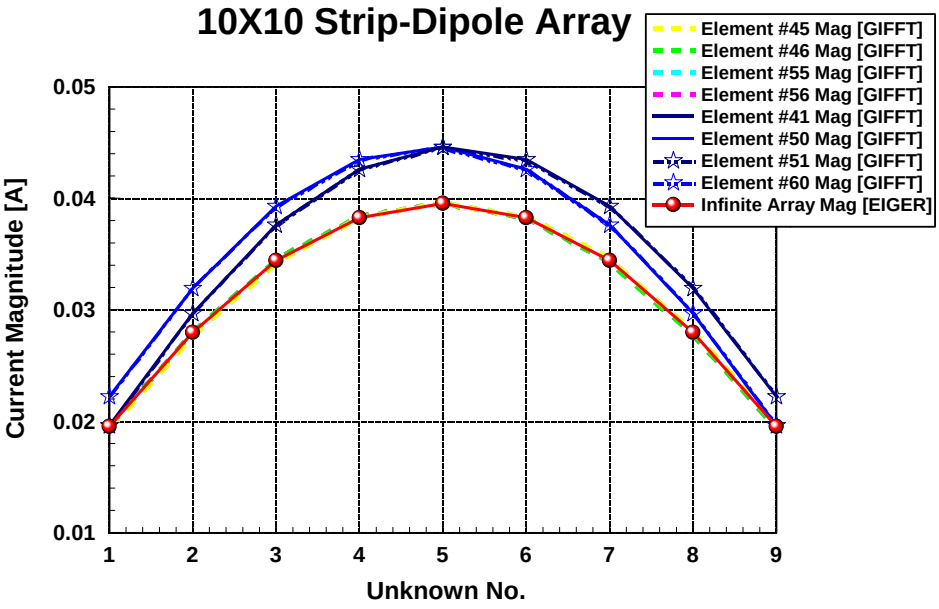

Figure 39. Current distributions for select elements of a 10×10 array.

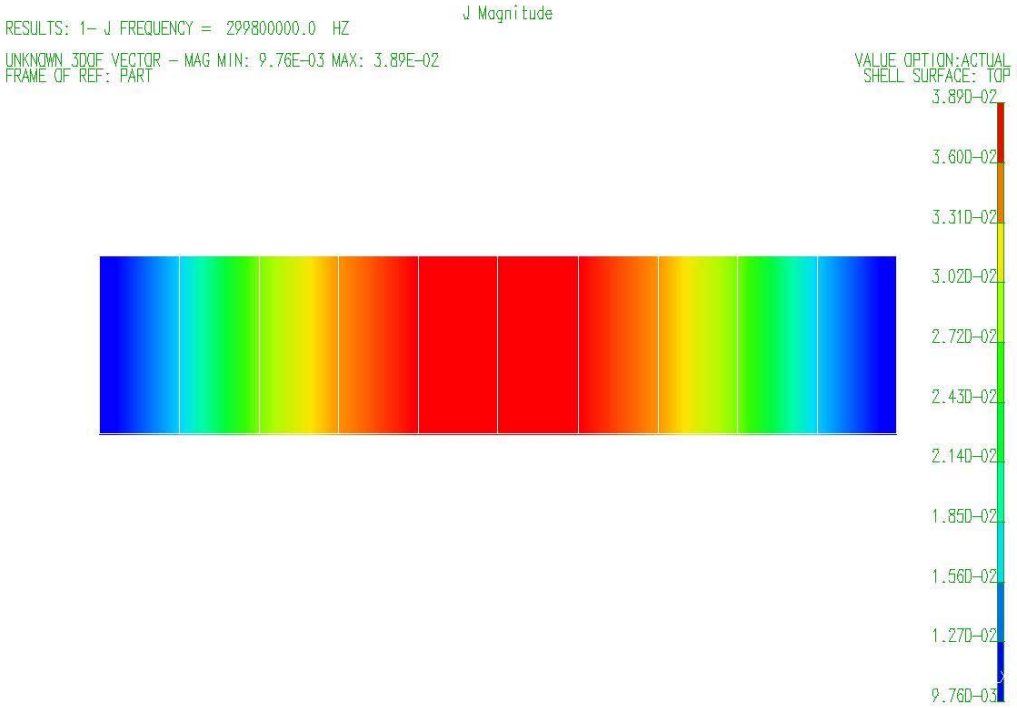

Figure 40. Contour plot of the current magnitude for an infinite array of the strip dipole shown in Figure 36.

and 41. Like the results shown in Figure 39, the currents towards the center of the array are characterized by the infinite array currents, whereas the elements closer to the edges (along $\widehat{x}$) are characterized by higher current values (note the respective scales on Figures 40 and 41). Furthermore, from the contour plot in Figure 41 it is possible to observe the current symmetry along the array (along the center of the array.)

Next we increase the size of the array even further to 40×40 elements. In Figure 42 we show the magnitude of the current at the strip centers along various rows and columns of the array. Also plotted is the current associated with the infinite strip array, where the value of the center currents are all identical. Proceeding along the middle row and middle column of the finite array (recognizing that, as shown above, the two center rows and columns have the same current distributions by symmetry), we find that the currents agree very well with the infinite array currents for the elements located towards the center of the array. However, as previously seen in the 10×10 array, as the position of the dipole gets closer to the edge of the array, the currents begin to differ from the infinite array solution, with the currents for the edge strips being the most different. Comparing the results corresponding to the first row and first column to that of the middle elements, it is interesting to note that the average of these currents approximately yields the values of the currents on the middle strips.

3.5.3 Computational Times

Table B contains some comparisons of the matrix fill and solve times for the GIFFT method and a standard MoM technique, based on the horizontal strip-array problem. These problems were all run on a PC with a XEON 3.0 GHz processor. Due to the Green's function interpolation, the matrix fill time associated with the GIFFT method is significantly lower than the fill time associated with the standard MoM. Comparing a 5×5 to a 10×10 array, it is evident that the time savings in the fill-time dramatically

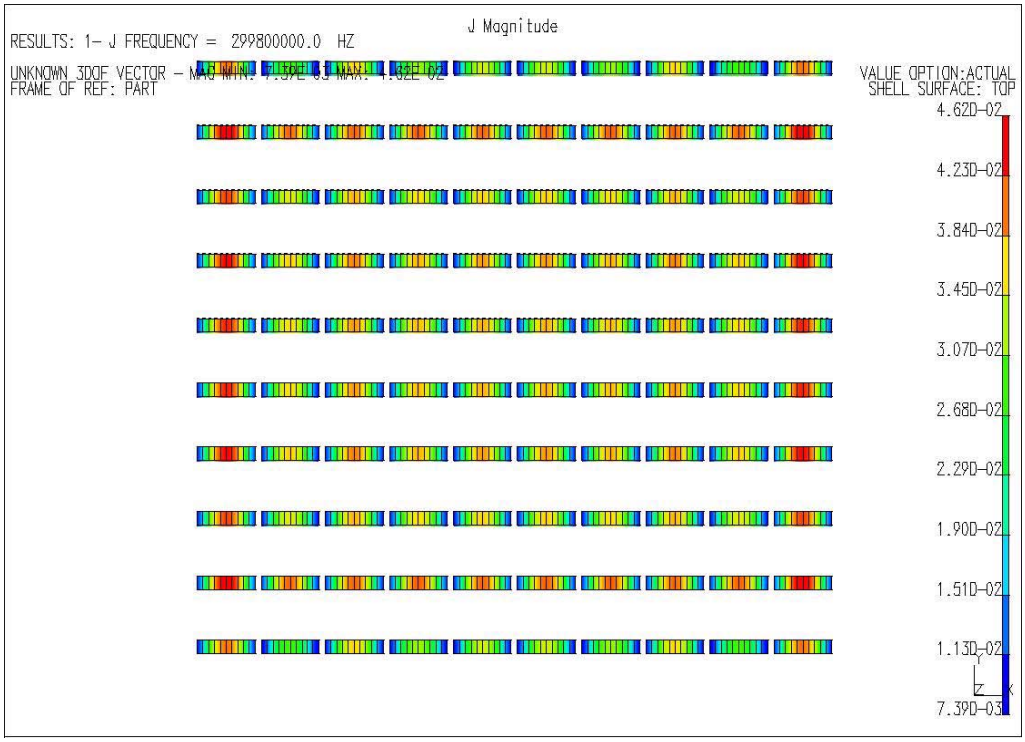

Figure 41. Contour plot of the current magnitude for a 10×10 array of the strip dipole shown in Figure 36.

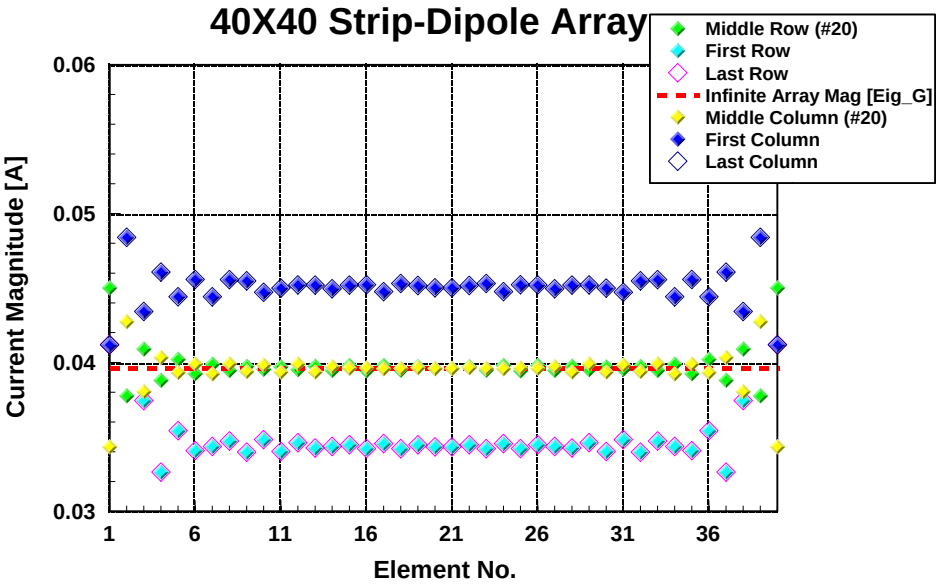

Figure 42. Current distributions for select elements of a 40×40 array.

increases as the size of the problem grows. Since the code using standard MoM has been optimized for direct solves while the iterative solver used in the GIFFT code has not, the matrix solve times for GIFFT are currently higher than for EIGER. Nevertheless, due to the significant decrease in fill times, GIFFT is an overall faster method than standard MoM (order $N \log N$ vs. N^3 for direct solve) and this is especially true for larger arrays. In addition to comparing the run times associated with the GIFFT and EIGER codes, it is important to note that the preprocessing time associated with the GIFFT code is significantly less than that for EIGER, where an explicit meshing of the array must be carried out. Since the preprocessing time increases dramatically with increasing array size, the explicit meshing of the 40×40 array and hence the time comparison for the two codes was not carried out for this case.

	Matrix Fill Time [s]	Matrix Solve Time [s]
GIFFT [EIGER_GIFFT]5×5	1.625	0.125
Standard MoM [EIGER] 5×5	89.172	0.07813
GIFFT [EIGER_GIFFT]10×10	1.531	1.484
Standard MoM [EIGER]10×10	704.39	0.1875

Table B. Matrix fill and solve times for a 5×5 and 10×10 element array using GIFFT and the standard MoM.

3.5.4 Defect in a 5×5 Element Array

In this section of the report, we examine the changes in the array current and radiation pattern as defect elements are introduced into the array. In Figure 43 the current magnitudes for the middle-row strips in the array are presented, where the center element (#13) has been rotated about $\widehat{z}$ by 45°. (The array input deck associated with this array geometry is given in Table C.) From Figure 43 we observe that, relative to the array with no defects, the current levels are decreased when keeping the same plane-wave illumination (an $\widehat{x}$ directed electric field). For comparison purposes, the current results determined using the standard MoM code (EIGER) are also shown in Figure 43, where the results are found to be in very good agreement.

In Figure 44, the θ polarization of the far-zone electric field (E_θ in the E-plane) is shown for the two cases of a perfectly-aligned 5×5 array and one where the center element has been tilted by 45°. While this single defect (a point defect) results in little change in E_θ , the presence of the defect creates an E_φ pattern where none existed previously. This is as expected due to the 45° orientation of the excited currents on the rotated dipole, where previously the currents flowed only along the $\widehat{x}$ direction. The E_φ pattern characterizing the array with the defect element is presented in Figure 45.

3.6 Conclusion and Future Work on Defects

The GIFFT method has been generalized to enable the treatment of source structures embedded in a periodic background of finite size. As an example, the GIFFT method was applied to the case of a short dipole source above an artificial material made of two layers of capacitively loaded SRRs. The problem illustrates the variety of results one can obtain with small and large meta-material substrates of finite size, structures where the large number of unknowns typically make such problems computationally challenging. In this analysis, sources (and/or defects) in other meta-materials made by a periodic arrangement of other resonant or nonresonant subwavelength structures could be treated as well. The present contribution is devoted to scatterers in free space; inclusions in a multilayer environment will be treated in future investigations. GIFFT was also used to examine large, truncated FSS's and single point defects.

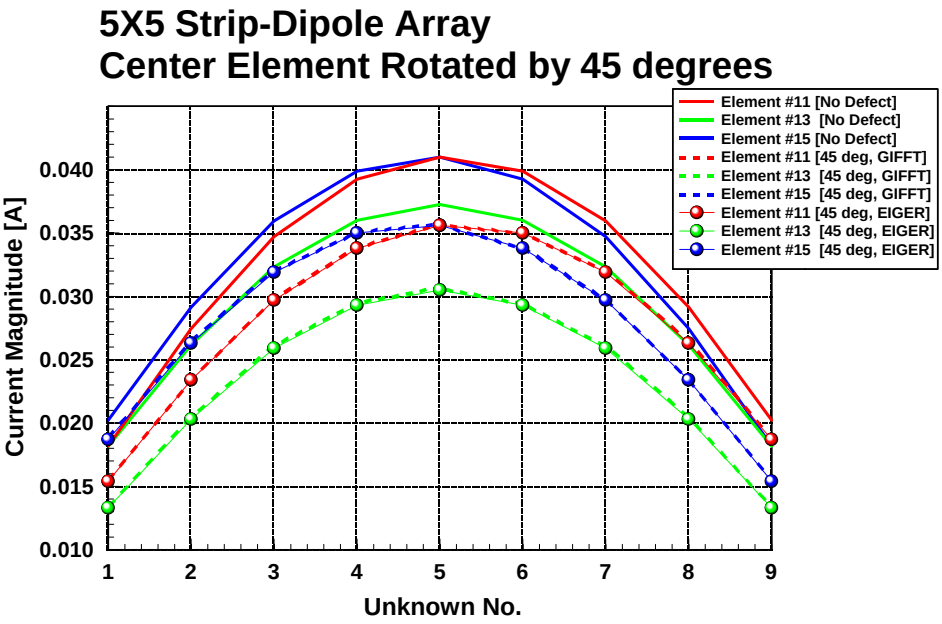

Figure 43. Effect on the current density of a 45^0 rotation of the center element of a 5×5 strip dipole array

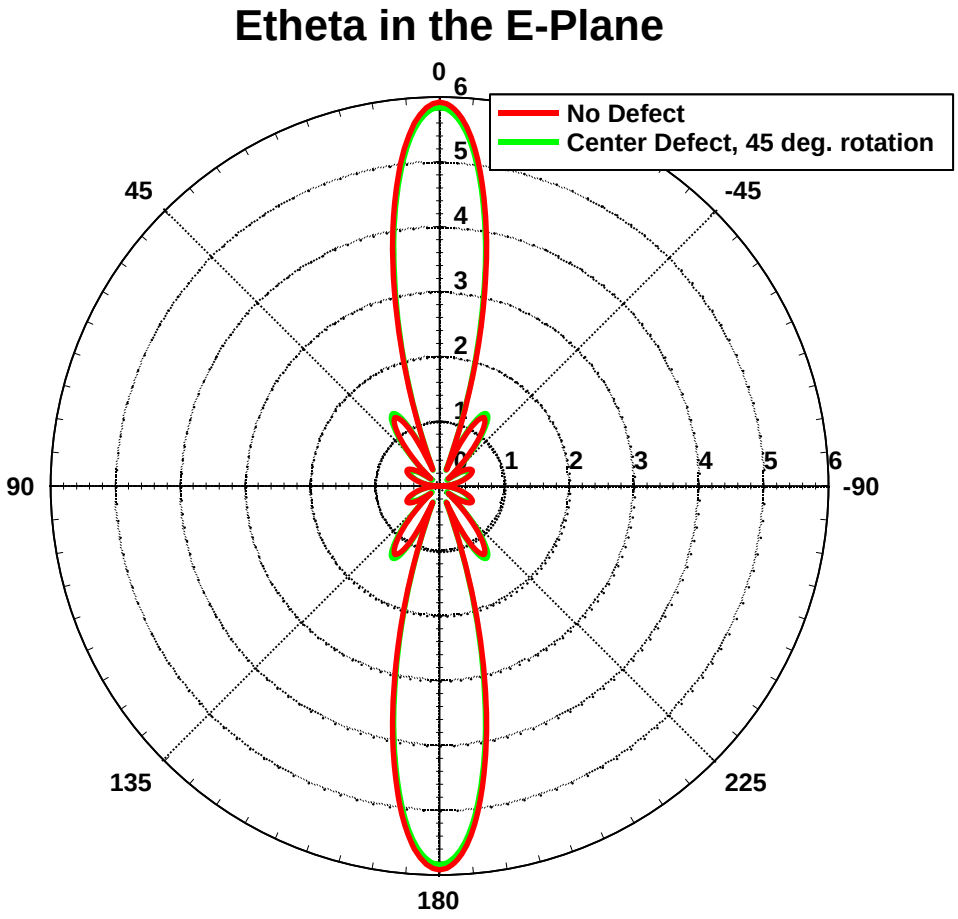

Figure 44. Effect on E_θ of a 45^0 rotation of the center element of a 5×5 strip dipole array

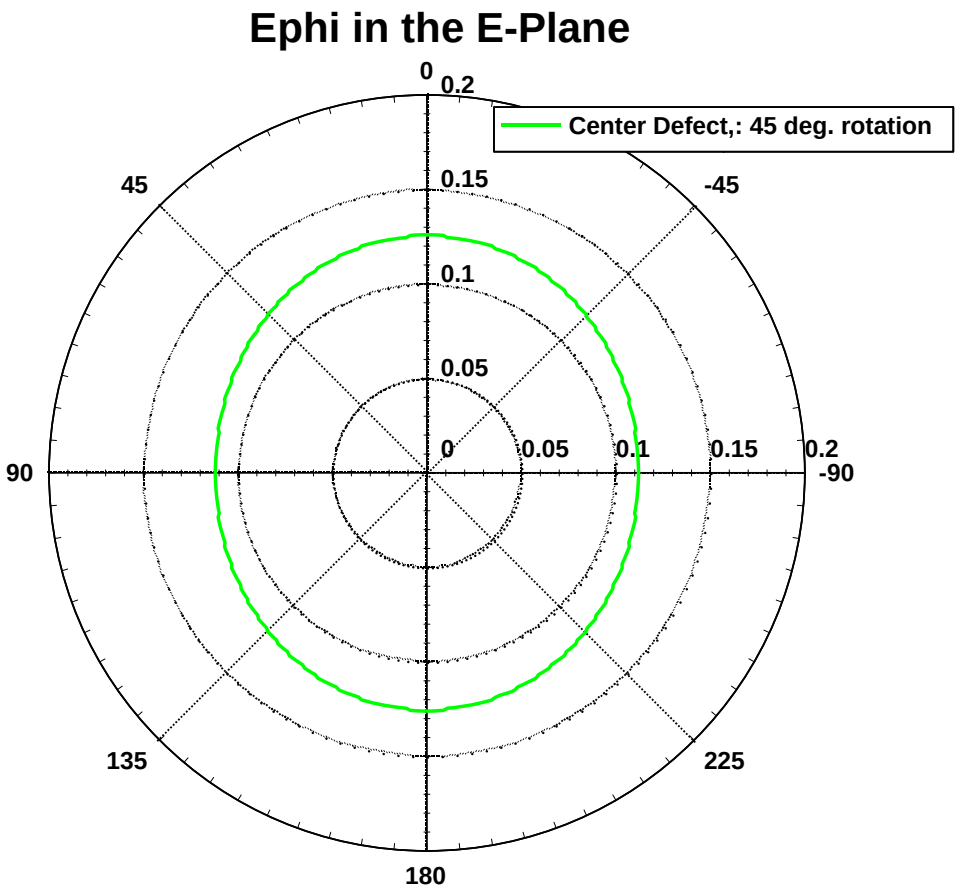

Figure 45. Effect on E_ϕ of a 45^0 rotation of the center element of a 5×5 strip dipole array

Input	Input Descriptor
4	number of vertices of the array
0.0 0.0 0.0	The coordinates of the vertices bounding the array, vertex 1
2.5 0.0 0.0	vertex 2
2.5 2.5 0.0	vertex 3
0.0 2.5 0.0	vertex 4
0.5 0.0 0.0	Lattice vector 1 describing periodicity in xy plane
0.0 0.5 0.0	Lattice vector 2 describing periodicity in xy plane
5 5 1	The number of interpolation points to use in the x,y,z direction.
1	Flag - 1=use GIFFT, 0 =use block Toep.
0	Preconditioner type - 0 = block diag 1= all near -1 = none.
0	ArrayFull3DFlag. 0 = no FFT in z. 1 = FFT in z.
0	ArraySameExciteFlag. If 1, all right hand sides will be identical.
0	ArrayPhasedFlag. 0=no phasing added, 1=linear phasing added to RHS
0.0 0.0	The scan angle in theta and phi. This is ignored if ArrayPhasedFlag is 0
1	FastNearFlag. 1 = if using GIFFT, 0 = never use FFT for near field.
0	ArrayPortAnalysisFlag
2	Number of types of array elements in the array
10	Number of meshing elements in first array element
10	Number of meshing elements in second array element
1	Background element - this is the predominant element in the array.
1	Number of array elements which are different from the background element (defect)
13 2	Indices of the defect element and array element type they are

Table C. Array input file for a 5X5 array with center defect element.

4 The Seam Problem

The most general type of seam is shown in Figure 46 where the period (b) is maintained in the $\widehat{y}$ direction, but both shape of the unit cell and the period (a) is changed in the $\widehat{x}$ direction as we cross the seam. Again we use the three dots to denote the fact that the periodic structure is not truncated and we are studying only the scattering of the seam. We begin by studying the simplest seam imaginable that retains the features of the general seam. This simple seam is made of two semi-infinite arrays of strips that change periodicity and strip width crossing the seam. We use this simple problem to understand how the fringe current magnitude compares to the magnitude of other currents in the vicinity of the seam. We then formulate the 3D seam shown in Figure 46 and find that we need to first obtain a Green's function for a 1d array of point sources. We go on to examine some useful approximations that we can exploit and finish with using GIFFT to solve one of the special seam configurations – changing the unit cell shape across the seam, but maintaining a constant periodicity.

4.1 Numerically Exact, 1D Seam Problem

Figure 47 shows a seam between two perfect electric conducting (PEC) strip arrays. The strip array in the $x > 0$ region has a periodicity of a', a strip width of $w_{a'}$ and extends to $x = +\infty$. The strip array in the $x < 0$ region has a periodicity of a, a strip width of w_a and extends to $x = -\infty$. A plane wave,

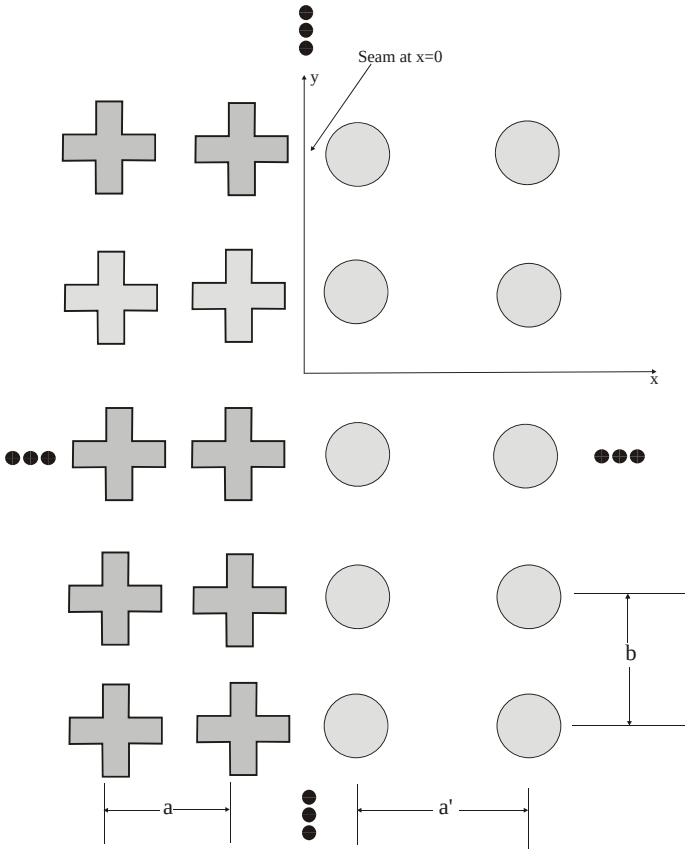

Figure 46. General seam geometry

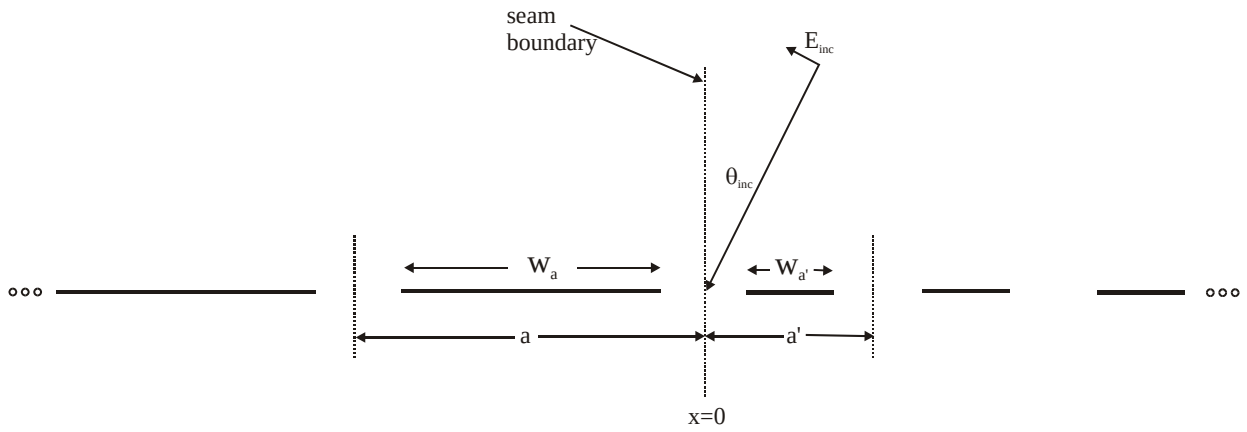

Figure 47. Geometry of a 1d seam

polarized either transverse electric (TE) (as shown) or transverse magnetic (TM) to the strip axis ($\widehat{y}$), is incident at an angle of θ_{inc} with respect to $\widehat{z}$.

We postulate that the influence of the seam on the current will extend a very short distance on either side of the seam – perhaps one or two unit cells on each side. Further away, the current will be the same as that on an infinite strip array. To check this postulate we solved for the current on a finite array of strips with a seam as shown in Figure 48. In this problem $w_{a'} = 1$ m, $a' = 2$ m, $w_a = 3$ m and $a = 4$ m. The beginning and end positions of the strips in meters are shown in Figure 48 for the first few strips adjacent to the seam. The numbers below the strips are included so we can conveniently refer to the results on each strip. The finite array consists of eight strips in all, five for $x > 0$ (m=0,1,2,3,4) and three for $x < 0$ (m=-1,-2,-3). The incident field is polarized to TE to the axis of the strips and has a strength at the origin of 1 V/m. It is incident at an angle of $\theta_{inc} = 50^0$ and has a frequency of 100 MHz.

Results are shown in Figures 49 through 53. Each result shows the current on one of the strips in the vicinity of the seam. The finite results are compared to the results from solving the infinite periodic problem (either using $w_{a'} = 1$ m and $a' = 2$ m or $w_a = 3$ m, and $a = 4$ m). Both magnitude and phase are shown. The magnitude of the difference between the finite and infinite, periodic case is also shown. Even adjacent to the seam the infinite periodic case does a good job in mimicking the finite case. One cell away from the seam it does even better. Even further away from the seam the finite case begins to deviate from the infinite periodic case because of the effect of truncation, which seems to have a bigger effect than this particular seam.

Based on the preceding examination, we will modify the solution procedure. We apply the electric field

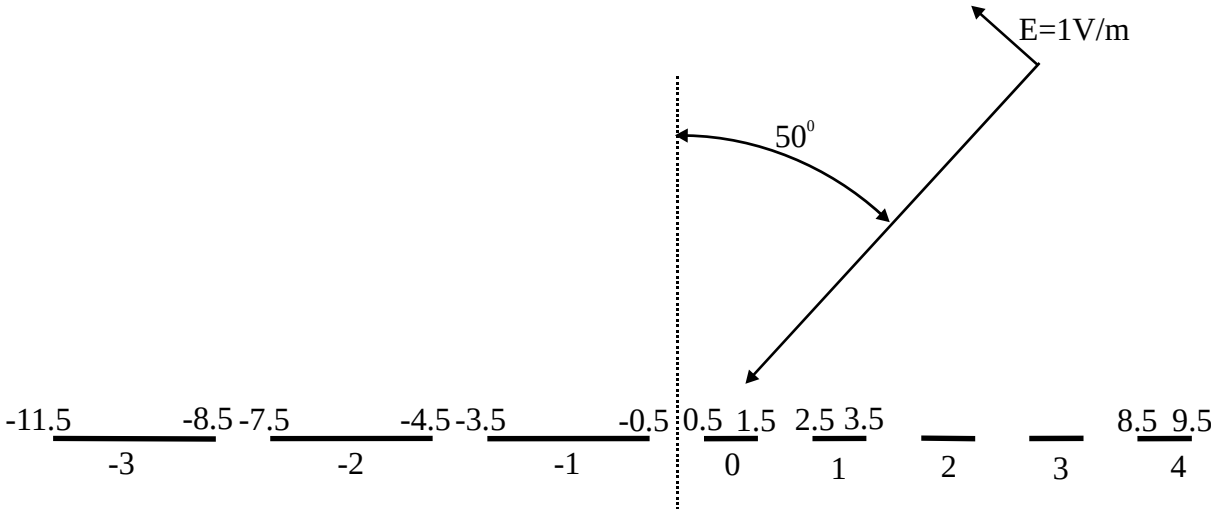

Figure 48. Finite seam

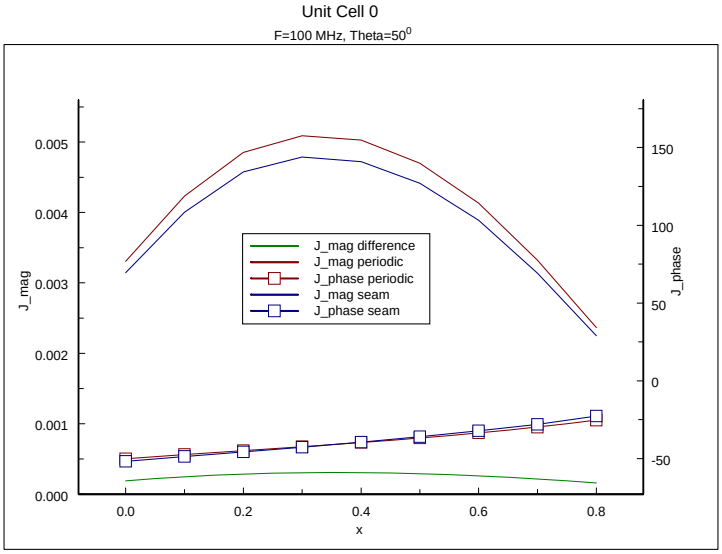

Figure 49. Current on strip at the m=0 position

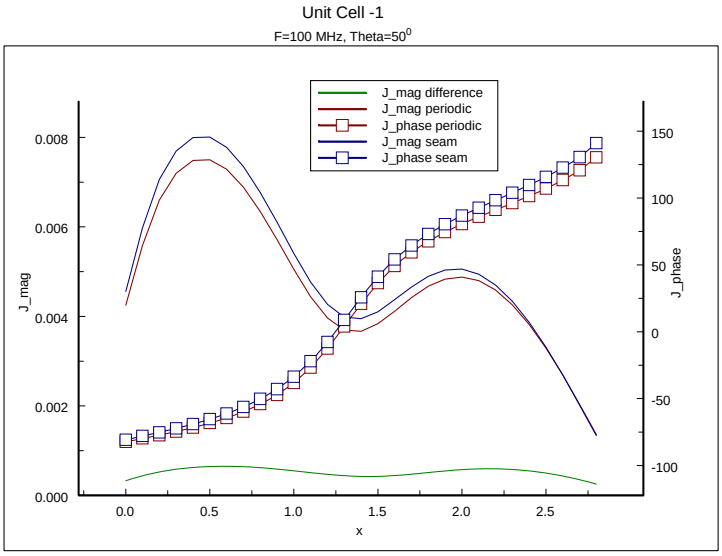

Figure 50. Current on strip at the m=-1 position

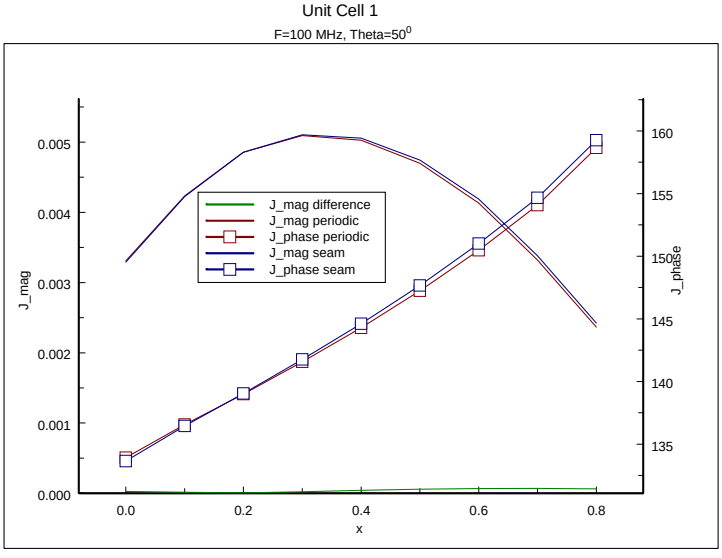

Figure 51. Current on strip at the m=+1 position

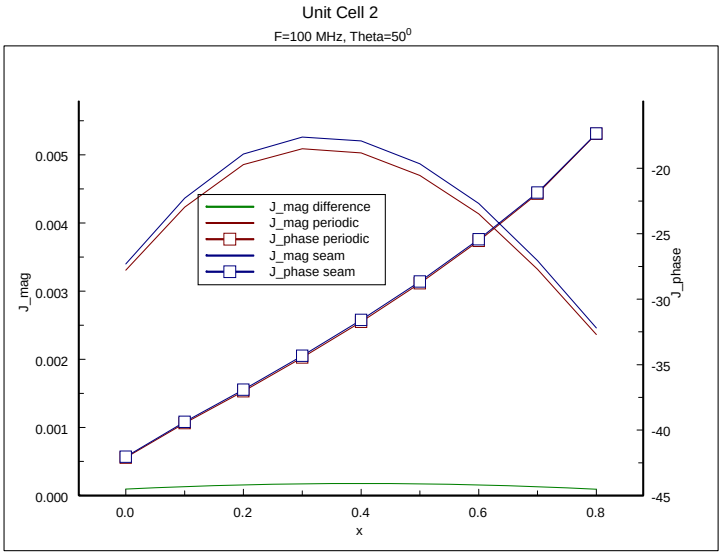

Figure 52. Current on strip at the m=+2 position

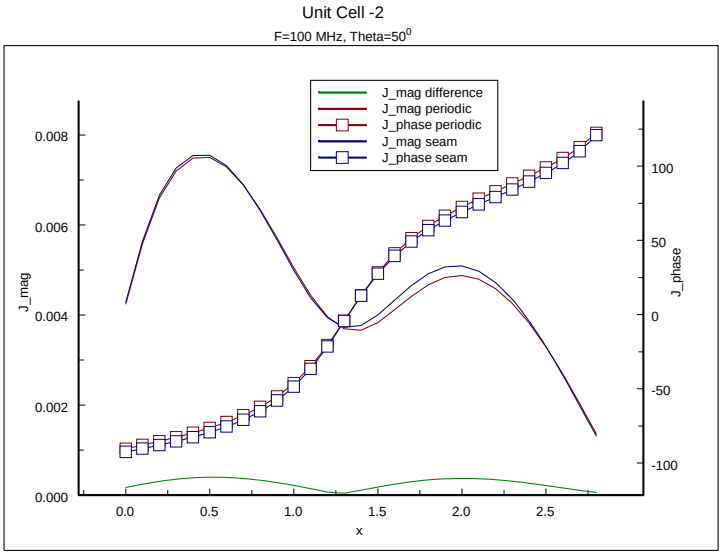

Figure 53. Current on strip at the m=-2 position

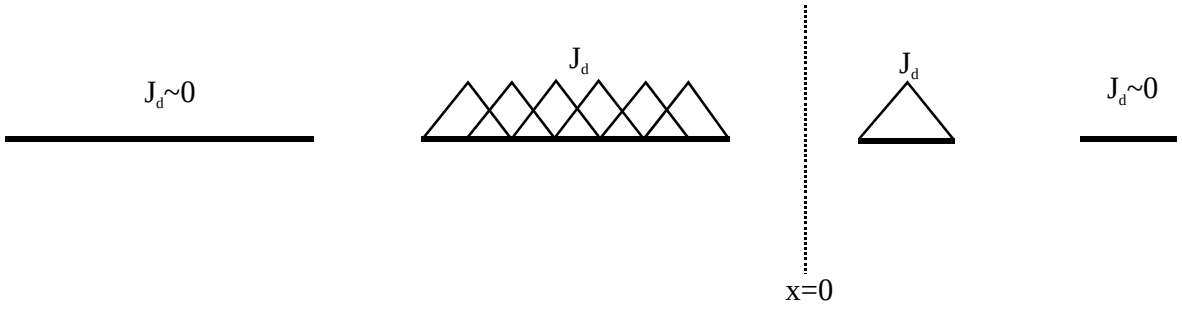

Figure 54. Basis function for the difference current (J_d)

integral equation (EFIE) to solve for an unknown difference current $J_d(x)$ on the strips near the seam.

$$J_d(x) = \begin{cases} J(x) - J_{pa'}(x) & x > 0 \\ J(x) - J_{pa}(x) & x < 0 \end{cases}$$

$J_{pa}(x)$ is known and is the solution of the infinite strip array with strip width w_a and periodicity a. $J_{pa}(x)$ exists in the semi-infinite region where $x < 0$. $J_{pa'}(x)$ is also known and is the solution of the infinite strip array with strip width $w_{a'}$ and periodicity a'. $J_{pa'}(x)$ exists when $x > 0$. The EFIE sets the total tangential electric field to be zero on the strips resulting in

$$E^s(J_d(x)) + E^s(J_{pa}(x)) + E^s(J_{pa'}(x)) = -E^{inc} \tag{7}$$

where E^{inc} is the incident electric field tangential to the strip and $E^s(J)$ is the scattered electric field tangential to the strip due to the current J. All we have done thus far is to subtract and add $J_{pa}(x)$ (or $J_{pa'}(x)$ depending on the region) and use the linearity of the electric field operator to separate out the contributions of $E^s(J_{pa}(x))$ and $E^s(J_{pa'}(x))$.

Since $J_{pa}(x)$ and $J_{pa'}(x)$ are known, we can move their contribution to the right hand side of Equation 7 and form a matrix equation by expanding J_d in terms of basis functions and testing with test functions T

$$< T, E^s(J_d(x)) >= - < T, E^{inc} > - < T, E^s(J_{pa}(x)) > - < T, E^s(J_{pa'}(x)) > \tag{8}$$

Based on our previous tests, we make the approximation that $J_d(x) = 0$ away from the seam as shown schematically in Figure 54. With this approximation we have changed the infinite problem into that of a finite problem. $J_{pa}(x)$ and $J_{pa'}(x)$ are shown in Figure 55 where m extends to $\pm\infty$ so these terms contain the effect of infinity. The left hand side has already been implemented in EIGER as has the first term on the right hand side. The only terms left to implement are the two remaining terms on the right hand side, which can be thought of as modifications of the incident field.

Let us concentrate on the term $< T, E^s(J_{pa'}(x)) >$, because the other term is calculated in a similar manner. We know $J_{pa'}(x)$ on the unit cell $m = 0$ form a solution of the infinite, periodic problem. We also know that the solution on other unit cells are

$$J_{pa'}(x + ma') = J^0_{pa'}(x)\, e^{jk_x ma'}$$

where $k_x = k_0 \sin(\theta_{inc})$. Therefore,

$$< T, E^s(J_{pa'}(x)) >=< T, \sum_{m=0}^{N} \sum_{n=1}^{n_b} E^s\left(J^0_{pa'}(x)\, e^{jk_x ma'}\right) >$$

where the summation over m represents the contribution from each of the unit cells truncated at a large number N. The summation over n represents the contribution of each of the triangular basis functions within a unit cell. Since EIGER has software to calculate the field due to a triangular basis function (line source) it was a simple matter to modify EIGER to fill and solve the matrix equation represented by

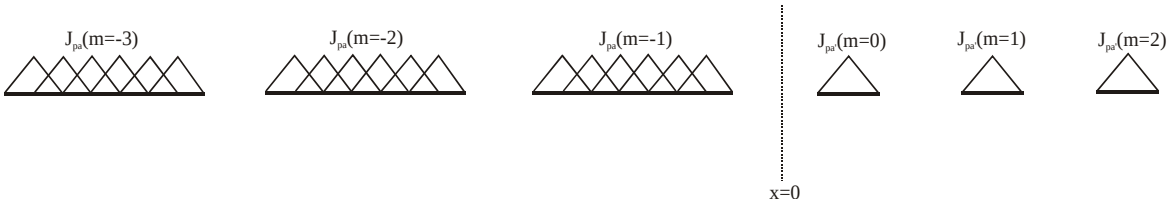

Figure 55. Basis function for the known periodic current

Equation 8.

We applied the modified EIGER to solve the infinite seam problem with the same unit cell description shown in Figure 48. The results are shown in Figure 56, which plots J_d as a function of distance away from the seam. Also shown, but only for the two cells immediately adjacent to the seam, is the infinite periodic case. Note that the ordinate is on a log scale so J_d is about one tenth the periodic current at the seam and decays rapidly away from the seam. In order to find the fields due to these currents we could first add the currents and then calculate the field or we could calculate the field only due to the fringe current and add to this the field due to the semi-infinite periodic current. The fringe current is localized and is the source of a cylindrical wave that could be described using a diffraction coefficient. The semi-infinite periodic current could be summed directly or calculated using a high frequency asymptotic solution as described by Carin [20].

EIGER already had implemented a Green's function that calculates the E field due to a line source, which we used to solve the one-dimensional seam. We can use the same formulation (Equation 8) to solve the general seam shown in Figure 46 (and shown in greater detail in Figure 57) with the following modifications. J_{pa} is now the current on the infinite array of cross shapes that occupies $x < 0$ and $J_{pa'}$ is the current on an infinite array of discs that occupies $x > 0$. Subdomain basis functions (tent shaped or Rao-Wilton-Glisson) are used to model the difference current J_d. The testing to satisfy the boundary condition is only done on the elements occupying the $n = 0$ row. Since we have periodicity in the $\widehat{y}$ direction, the J_d for each row is related to the current on row 0 by the phase dictated by the incident plane wave

$$J_d\left(x, y + nb\right) = J_d^0\left(x, y\right) e^{+jk_y nb}$$

where $k_y = k_0 \sin\left(\theta_{inc}\right) \sin\left(\phi_{inc}\right)$ referring back to Figure 2. We see that instead of needing to calculate the E field due a line source as we did to find $E^s\left(J_d\left(x\right)\right)$, $E^s\left(J_{pa}\left(x\right)\right)$, and $E^s\left(J_{pa'}\left(x\right)\right)$ for the 1d seam, we now need the E field due to a 1d, infinite array of point sources that extend along $\widehat{y}$ with a period b. EIGER doesn't have this Green's function built in yet and the next section will discuss how it is calculated.

4.2 The Green's Function for a 1d Array of Point Sources

In applying numerical full wave methods like the Method of Moments (MoM) or Boundary Integral Equations (BIE) to periodic structures made of conducting or dielectric electromagnetic scatterers, fast and accurate means for evaluating the periodic Green's function (GF) are often needed, in both microwave and optical frequencies where also other techniques could benefit by the fast evaluation of the periodic GF. The GF can also be used directly in analogous acoustic problems.

Among various techniques to accelerate computation of the periodic GF is the Ewald method, originally developed by P. P. Ewald in [45] to efficiently calculate the electrostatic scalar potential of a three-dimensional periodic distribution of point charges. The method has been applied to a large variety of problems ranging from solid state physics and chemistry to engineering.

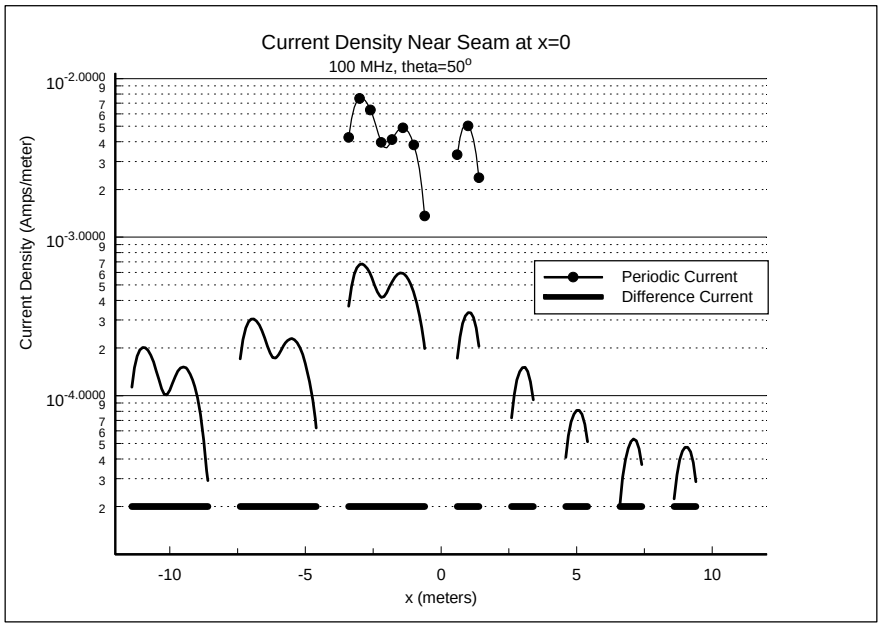

Figure 56. Current near a 1d seam

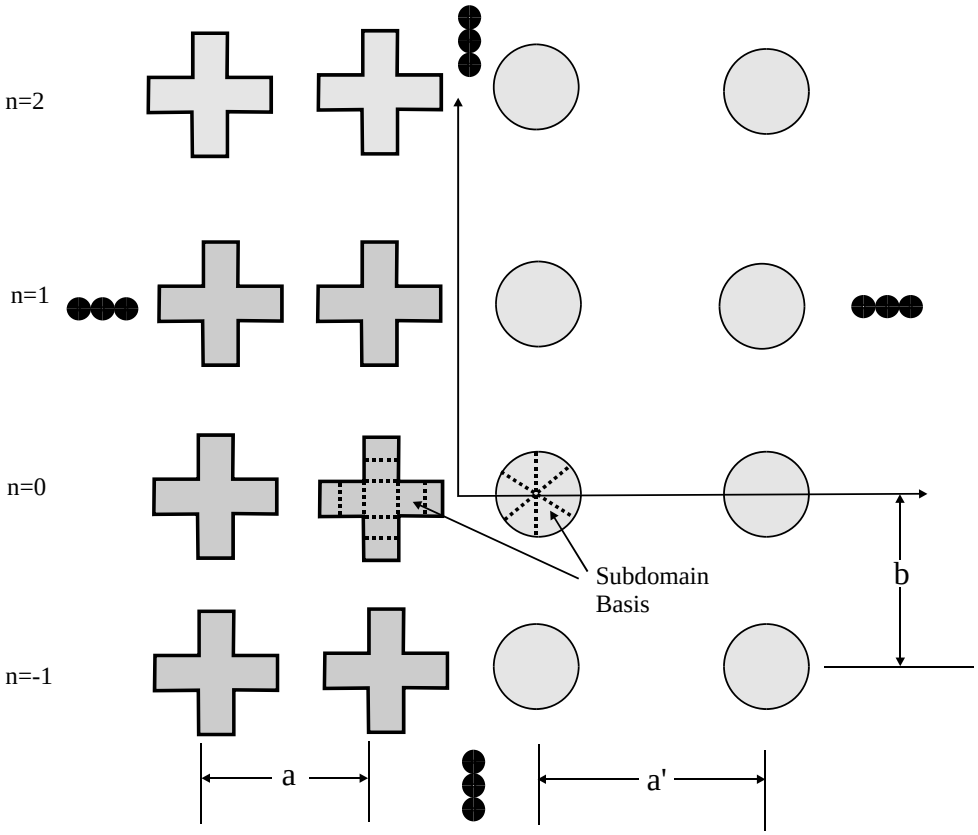

Figure 57. Detail of two-dimensional seam geometry

In the following we describe the application of the method to the electrodynamic or acoustic problems such as the solution of the Helmholtz equation with periodic boundary conditions. We list here the Ewald methods that have been previously developed, and identify our own contribution.

Jordan et al. extended the Ewald method to the case of the free space GF for three dimensional (3D) problems with 2D periodicity (i.e., a planar array of point sources) in [46]. Its application in evaluating GFs for multilayered media is treated in [47], [48], [49], [50]. The Ewald method is extended in [51],[52], [53] to 2D problems with 1D periodicity (i.e., a planar array of line sources). An analogous treatment of the GF for an array of line sources is reported in [54] where a more general view is also addressed, as well as in [55] where a Schlömilch series that may arise in diffraction theory is efficiently evaluated. We also point out that in [52] a comparison is made between various representations of the periodic GF concluding that the Ewald method is one of the most advantageous. For a mathematical review of the Ewald method in general, see [56]. For the case of a planar 2D-periodic array of point sources, the critical distance from the array plane beyond which the Ewald method is not advantageous compared to the standard spectral grating lobe series is analyzed in [57].

The evaluation of the GF for a rectangular cavity using the Ewald method is reported in [58], and its dyadic form in [59]. An application of the Ewald representation to hybrid methods involving a boundary integral equation and finite element method, for periodic structures, is given in [60]. In [61] the Ewald method is combined with another very effective method to analyze scattering by periodically etched layered conducting surfaces such as are commonly used for frequency selective surfaces.

Using the Ewald method, we accelerate for the first time the GF pertaining to a linear array of point sources (i.e., a 3D problem with 1D periodicity.) The formula representations obtained in the above mentioned studies, i.e., the GF for geometries such as the 2D-periodic array of point sources [46], and the 1D-periodic array of line sources [51],[52],[53],[54], cannot be applied to this new geometry. The standard purely spectral sum representation for the GF cannot be used for this new particular configuration because it diverges when the observation point lies on the axis of the linear array, thus further proving the utility of the Ewald method, which exhibits a Gaussian convergence. A numerical analysis of the convergence rate is also provided, supported by analytical considerations. As previously noted in [62], at high frequencies such that the wavelength is somewhat smaller than the period, computing the Ewald series using the optimal splitting parameter E_0 (see [46]) may yield inaccurate results due to the finiteness of machine precision. In [62] it is suggested that such numerical inaccuracies may be improved by increasing the value of the splitting parameter E as frequency increases, but no guidelines for choosing the parameter are given. Here we present an algorithm for choosing the Ewald splitting parameter E that extends the efficiency of the method when the wavelength is somewhat smaller than the periodicity. The proposed algorithm is efficiently applied to periodic structures when the observation point is near the axis of the linear array of point sources.

For several numerical methods such as MoM or BIE applied to periodic structures with period d along z, it may be convenient to find the scalar potential radiated by an infinite linear array of point sources located at $r'_n = nd\hat{\mathbf{z}}$, where bold symbols define vector quantities, the caret ($\hat{}$) defines unit vectors, and $n = 0, \pm 1, \pm 2, ...$ The point sources may be excited with a linear phase progression $e^{-jk_{z0}z}$, where k_{z0} is the longitudinal wavenumber, that may originate by an impinging plane wave (impressed wavenumber) or by generators within each cell with a linear phase progression. An $e^{j\omega t}$ time dependence, with $j = \sqrt{-1}$, is assumed and suppressed throughout this paper. If one adopts an $e^{-i\omega t}$ time dependence, with $i = \sqrt{-1}$, all intermediate and final formula here derived apply as well after complex conjugation.

The GF for such a problem periodic along z, with period d, is given by the outgoing solution of the Helmholtz equation $\nabla^2 G(r, r') + k^2 G(r, r') = -\delta_p(r')$, where the periodic (along z) forcing term $\delta_p(r')$ is written as $\delta_p(r') = \sum_{n=0}^{\infty} \delta(x')\delta(y')\delta(z' - nd)e^{-jk_{z0}nd}$. The GF solution of the Helmholtz equation may be

represented as the spatial sum of spherical waves

$$G(\mathbf{r},\mathbf{r}') = \sum_{n=-\infty}^{\infty} e^{-jk_{z0}nd} \frac{e^{-jkR_n}}{4\pi R_n} \tag{9}$$

where $R_n = \sqrt{\rho^2 + (z-nd)^2}$ is the distance between the observation point $r \equiv \rho\hat{\boldsymbol{\rho}} + z\hat{\mathbf{z}}$ and the nth source point $r'_n = nd\hat{\mathbf{z}}$ (see Figure 58). Because of the symmetry of the problem, we use cylindrical coordinates and denote an arbitrary point as $r = (\rho, z)$. Terms in the series (9) are of order $n^{-1}\exp(-jn\theta)$, where $\theta = (k_{z0}+k)d$ for large positive n, and $\theta = (k_{z0}-k)d$ for large negative n, so that the series is extremely slowly convergent. The series diverges for $\theta = 2m\pi$, where m is an arbitrary integer, because the spherical contributions arising from at least one side of the linear array would all add in phase. In other words, one of the Floquet waves (see what follows) is propagating at grazing.

An alternative spectral series representation of this GF may be obtained by applying to (9) the infinite Poisson sum formula [63, p.117], $\sum_{n=-\infty}^{\infty} f(nd) = \frac{1}{d}\sum_{q=-\infty}^{\infty} \tilde{f}\,(2\pi q/d)$, where

$$f(nd) = e^{-jk_{z0}nd} \frac{e^{-jkR_n}}{4\pi R_n} \tag{10}$$

and

$$\tilde{f}\left(\frac{2\pi q}{d}\right) = \int_{-\infty}^{\infty} e^{-j(\frac{2\pi q}{d})z'} f(z')dz' \tag{11}$$

is its Fourier transform. This yields the GF representation as a sum of cylindrical harmonics,

$$G(\mathbf{r},\mathbf{r}') = \frac{1}{4jd} \sum_{q=-\infty}^{\infty} e^{-jk_{zq}z} H_0^{(2)}(k_{\rho q}\rho) \tag{12}$$

but it is also slowly convergent. Here $H_0^{(2)}$ is the Hankel function of zeroth order and second kind,

$$k_{zq} = k_{z0} + \frac{2\pi q}{d} \tag{13}$$

is the qth Floquet wavenumber along z, and

$$k_{\rho q} = \sqrt{k^2 - k_{zq}^2} \tag{14}$$

is the qth transverse Floquet wavenumber, along ρ. Convergence of the field far away from the linear array requires that $\mathrm{Im}\, k_{\rho q} < 0$, as can be inferred from the large argument expansion of the Hankel function. For a real excitation wavenumber k_{z0} and for radiation in a lossless medium (real k), q-harmonics such that $k_{\rho q} > 0$, for $k_{zq} < k$, index radially propagating Floquet waves, while when $k_{\rho q} = -j[k_{zq}^2 - k^2]^{1/2}$, for $k_{zq} > k$, q indexes radially attenuating Floquet waves.

Note that the expression (12) has the important drawback that it cannot be used when the observation point lies on the axis of the array, namely when $\rho = 0$, a situation that often happens in the MoM or BIE. Here we provide a representation of the GF (9) or (12) as a rapidly converging series, that can be evaluated also when $\rho = 0$.

4.2.1 The Ewald Transformation

Following [46] the GF for a single source is represented as

$$\frac{e^{-jkR_n}}{4\pi R_n} = \frac{1}{2\pi\sqrt{\pi}} \int_0^{\infty} e^{-R_n^2 s^2 + \frac{k^2}{4s^2}} ds, \tag{15}$$

where the integration path in the complex space is shown in Figure 59. For simplicity, the homogeneous medium is assumed to have small losses and the complex ambient wavenumber $k = k_r + jk_i$ has $k_i < 0$. The particular shape of the integration path is dictated by constraints for the integrability of the integrand of (15), which is explained as follows. It is useful to write the ambient wavenumber in polar coordinates

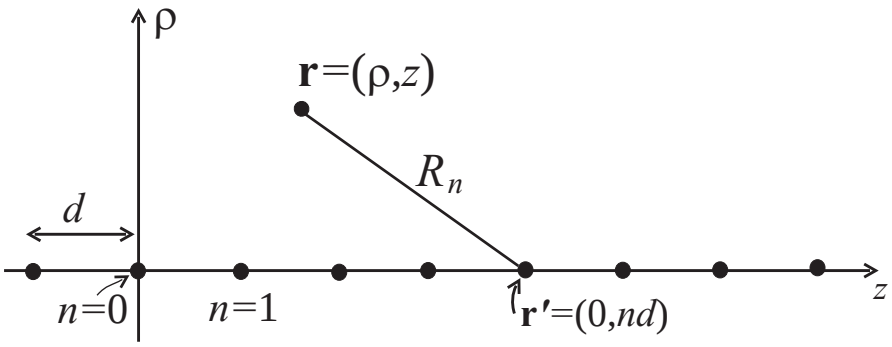

Figure 58. Physical configuration and coordinates for a planar periodic array of point sources with interelement spacing d along z. R_n is the distance between observation point $\mathbf{r} \equiv (\rho, z)$ and the nth source element $\mathbf{r}'_n \equiv (0, nd)$.

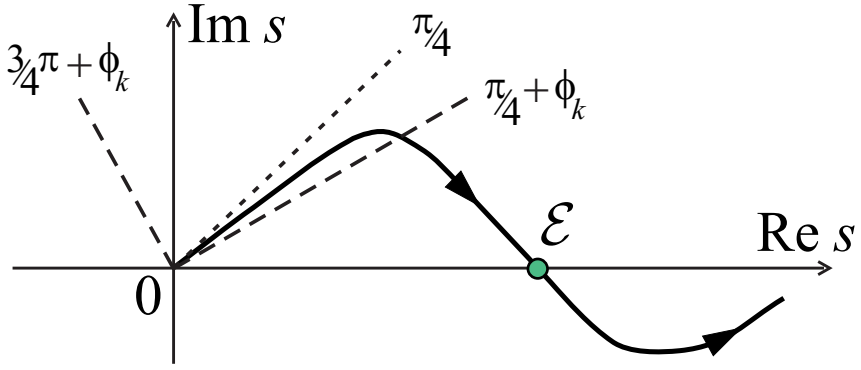

Figure 59. Path of integration. Expressing $k = |k| \exp(j\phi_k)$ (Im $k \leq 0$, thus $\phi_k < 0$), and $s = |s| \exp(j\phi_s)$, the region of convergence of (15) is given in (16) and (17).

$k = |k|e^{j\phi_k}$, with $\phi_k = \arctan(k_i/k_r) < 0$, and $s = s_r + js_i = |s|\exp(j\phi_s)$ with $\phi_s = \arctan(s_i/s_r)$. Indeed, convergence of (15) is ensured by requiring that $\mathrm{Re}[k^2/s^2] < 0$ for $s \to 0$, and $\mathrm{Re}[R_n^2 s^2] > 0$ for $s \to \infty$, i.e.,

$$\frac{3}{4}\pi + \phi_k \quad \geq \quad \phi_s \geq \frac{\pi}{4} + \phi_k, \text{for } s \to 0 \tag{16}$$

$$\frac{\pi}{4} \quad > \quad \phi_s > -\frac{\pi}{4}, \text{for } s \to \infty \tag{17}$$

which are satisfied by the path in Figure 59. The Ewald method is obtained by splitting the integral in (15) into two parts, $\int_0^\infty = \left(\int_0^{\mathcal{E}} + \int_{\mathcal{E}}^\infty\right)$, which also determines the splitting

$$G(\mathbf{r}, \mathbf{r}') = G_{\text{spectral}}(\mathbf{r}, \mathbf{r}') + G_{\text{spatial}}(\mathbf{r}, \mathbf{r}') \tag{18}$$

$$G_{\text{spectral}}(\mathbf{r}, \mathbf{r}') = \frac{1}{2\pi\sqrt{\pi}} \sum_{n=-\infty}^{\infty} e^{-jk_{z0}nd} \int_0^{\mathcal{E}} e^{-R_n s^2 + \frac{k^2}{4s^2}} ds \tag{19}$$

$$G_{\text{spatial}}(\mathbf{r}, \mathbf{r}') = \frac{1}{2\pi\sqrt{\pi}} \sum_{n=-\infty}^{\infty} e^{-jk_{z0}nd} \int_{\mathcal{E}}^{\infty} e^{-R_n^2 s^2 + \frac{k^2}{4s^2}} ds. \tag{20}$$

The spatial term G_{spatial} exhibits a Gaussian exponential convergence in n as can be inferred by noticing that $\mathrm{Re}(s) > \mathcal{E}$ on the complex integration path and for large n the integral in (20) behaves like $\frac{1}{\sqrt{\pi}} \int_{\mathcal{E}}^\infty e^{-n^2 d^2 s^2} ds = (2nd)^{-1}\mathrm{erfc}(nEd)$, where

$$\mathrm{erfc}(z) = \frac{2}{\sqrt{\pi}} \int_z^\infty e^{-t^2}\, dt \tag{21}$$

is the complementary error function. For large argument it is approximated by $\mathrm{erfc}(z) \sim e^{-z^2}/(\sqrt{\pi}z)$, which highlights the Gaussian n-convergence of (20). The spectral term (19) instead is slowly converging as $1/n$, since the original series (9) converges as $1/n$, and requires the use of the Poisson transformation to accelerate its convergence.

4.2.2 The Spectral Part of the Green's function

To accelerate the spectral part (19) of the GF in (18) we first apply the Poisson's sum formula, (cf., discussion before (10)), with

$$f(nd) = e^{-jk_{z0}nd} \int_0^{\mathcal{E}} e^{-\left[\rho^2 + (z-nd)^2\right]s^2 + \frac{k^2}{4s^2}} ds. \tag{22}$$

The evaluation of the Fourier transform $\tilde{f}(2\pi q/d)$, defined in (11), is carried out by first changing the order of integration, which is possible since $\mathrm{Re}(s^2) > 0$ on the integration path shown in Figure 59. More details on these mathematical steps are in [53, Section IV-A] where an analogous problem is treated. Then, the change of variable $(z', s) \to (u, s)$, with $u = (z - z')s$, after evaluation of the resulting u-integral, leads to

$$\tilde{f}\left(\frac{2\pi q}{d}\right) = \sqrt{\pi} e^{-jk_{zq}z} \int_0^{\mathcal{E}} e^{-\rho^2 s^2 + \frac{k_{\rho q}^2}{4s^2}}\, \frac{ds}{s}. \tag{23}$$

Note that $\mathrm{Re}(k_{\rho q}^2)$, with $k_{\rho q}^2 = k^2 - k_{zq}^2$, is negative for large q resulting in evanescent Floquet modes, hence the above integral is exponentially converging for large q. Let $u = \frac{1}{4s^2}$, with $\frac{ds}{s} = -\frac{1}{2}\frac{du}{u}$, so that the above integral is rewritten as

$$\tilde{f}\left(\frac{2\pi q}{d}\right) = \frac{\sqrt{\pi}}{2} e^{-jk_{zq}z} \int_{\frac{1}{4\mathcal{E}^2}}^\infty e^{-\frac{\rho^2}{4u} + k_{\rho q}^2 u}\, \frac{du}{u} \tag{24}$$

where the mapped integration path goes to infinity in the region between $\frac{\pi}{2}$ and $\frac{3\pi}{2}$ for real $k_{\rho q}$ (propagating modes), and in the region between $-\frac{\pi}{2}$ and $\frac{\pi}{2}$ for imaginary $k_{\rho q}$ (evanescent modes). The same argument applies when small ambient losses are present, while a deeper analysis is required for complex propagation

constants k_{zq}.

Next, following a procedure analogous to [51], [53, Section IV-B], we utilize the Taylor expansion $e^{-\rho^2/(4u)} = \sum_{p=0}^{\infty}(-1)^p(\rho/2)^{2p}/(p!u^p)$. After using the change of variable $w = 4E^2u$, an integration of the series term by term leads to

$$\tilde{f}\left(\frac{2\pi q}{d}\right) = \frac{\sqrt{\pi}}{2}e^{-jk_{zq}z}\sum_{p=0}^{\infty}\frac{(-1)^p}{p!}\left(\rho\mathcal{E}\right)^{2p}E_{p+1}(\frac{-k_{\rho q}^2}{4\mathcal{E}^2}) \tag{25}$$

in which $E_p(x)$ is the pth order exponential integral defined by [64, p. 228]

$$E_1(x) = \int_x^{\infty}\frac{e^{-t}}{t^p}dt, \quad |\arg x| < \pi, \tag{26}$$

and by the recurrence relation [64, p. 229]

$$E_{p+1}(x) = \frac{1}{p}[e^{-x} - xE_p(x)], \qquad p = 1, 2, 3, ... \tag{27}$$

The path of integration in (26) should exclude the origin and not cross the negative real axis [64, p. 229]. For evanescent waves, $-k_{\rho q}^2 > 0$ and one can also use the definition $E_p(x) = \int_1^{\infty} e^{-xt}\,t^{-p}dt$, valid for $\mathrm{Re}\,x > 0$. Substituting (25) into the Poisson transform of the original expression (19) leads to

$$G_{\text{spectral}}\left(\mathbf{r}, \mathbf{r}'\right) = \frac{1}{4\pi d}\sum_{q=-\infty}^{\infty}e^{-jk_{zq}z}\sum_{p=0}^{\infty}\frac{(-1)^p}{p!}\left(\rho\mathcal{E}\right)^{2p}E_{p+1}(\frac{-k_{\rho q}^2}{4\mathcal{E}^2}). \tag{28}$$

The exponential integral $E_1(x)$ may be evaluated using the algorithm of [64, Section 5.1.53] for $0 \le x \le 1$, or [64, Section 5.1.56]) for $1 \le x < \infty$. Though a double series, expression (28) is rapidly convergent. Indeed, only a handful of q terms and around ten p terms are necessary to reach a good accuracy, as shown in Section 4.2.8.

The exponential integral (26) has a branch cut along the negative real axis. Note that in absence of ambient losses, and for a real phasing wavenumber k_{z0} along the array, all propagating Floquet waves have $k_{\rho q}^2 = k^2 - k_{zq}^2 > 0$ and thus the argument of the exponential integral in (28) is negative real, resulting in an ambiguous branch condition.

To resolve the ambiguity we imagine small ambient losses such that $\mathrm{Im}(-k_{\rho q}^2) > 0$ and therefore the branch can be chosen automatically and one can use (26) directly. Though the assumption of losses is useful for the branch determination, in lossless media one may prefer to evaluate $E_{p+1}(x)$ obtained using the formula $E_1(-x + j0^+) = -Ei(x) - j\pi$, [64, p. 228], with

$$Ei(x) = -P\int_{-x}^{\infty}\frac{e^{-t}}{t}dt, \qquad x > 0, \tag{29}$$

where P denotes principal-value integration. For small argument the exponential integral Ei can be evaluated as $Ei(x) = \gamma + \ln x + \sum_{n=1}^{\infty}x^n/(n\,n!)$, for $x > 0$, where $\gamma \approx 0.57721566$ is the Euler constant. Note that once $E_1(-x + j0^+)$ is obtained, $E_{p+1}(-x + j0^+)$ follows from (27).

4.2.3 The Spatial Part of the Green's function

The spatial part of the GF in (20) already exhibits Gaussian convergence; here we reexpress it in terms of complementary error functions. Consider a generic n-term of the spatial series in (20)

$$I_n = \int_{\mathcal{E}}^{\infty}e^{-R_n^2s^2+\frac{k^2}{4s^2}}ds = e^{jkR_n}\int_{\mathcal{E}}^{\infty}e^{-\left[R_ns+j\frac{k}{2s}\right]^2}ds. \tag{30}$$

With the change of variable of $u = R_ns + jk/(2s)$, or $s = (u + \sqrt{u^2 - j2kR_n})/(2R_n)$, (30) is transformed

to

$$I_n = \frac{e^{jkR_n}}{2R_n}\int_{R_n\mathcal{E}+j\frac{k}{2\mathcal{E}}}^{\infty} e^{-u^2}du + \frac{e^{jkR_n}}{2R_n}\int_{R_n\mathcal{E}+j\frac{k}{2\mathcal{E}}}^{\infty} e^{-u^2}\frac{udu}{\sqrt{u^2-j2kR_n}}. \tag{31}$$

Now, the second integral is transformed by using the change of variable $w=\sqrt{u^2-j2kR_n}$, with lower end point $w_l^2=\left(R_n\mathcal{E}+j\frac{k}{2\mathcal{E}}\right)^2-j2kR_n=\left(R_n\mathcal{E}-j\frac{k}{2\mathcal{E}}\right)^2$, and $u^2=w^2+j2kR_n$, yielding

$$I_n = \frac{e^{jkR_n}}{2R_n}\int_{R_n\mathcal{E}+j\frac{k}{2\mathcal{E}}}^{\infty} e^{-u^2}du + \frac{e^{-jkR_n}}{2R_n}\int_{R_n\mathcal{E}-j\frac{k}{2\mathcal{E}}}^{\infty} e^{-w^2}dw. \tag{32}$$

Inserting this result into (20) leads finally to

$$\begin{aligned} G_{\text{spatial}}(\mathbf{r},\mathbf{r}') &= \frac{1}{8\pi}\sum_{n=-\infty}^{\infty}\frac{e^{-jk_{z0}nd}}{R_n}\left[e^{jkR_n}\,\text{erfc}\left(R_n\mathcal{E}+j\frac{k}{2\mathcal{E}}\right)\right. \\ &\quad \left. +e^{-jkR_n}\,\text{erfc}\left(R_n\mathcal{E}-j\frac{k}{2\mathcal{E}}\right)\right] \end{aligned} \tag{33}$$

where the complementary error function erfc is defined in (21). For its fast evaluation see [65]

4.2.4 The Singular Spatial Contribution

The GF often appears convolved with induced or equivalent currents within a reference cell of the periodic structure (which we take to be the $n=0$ cell), and special treatment is needed for the case when the observation point $\mathbf{r}$ is close to the source point in the cell, resulting in a vanishing R_0. From the GF representation in (9) we know that when $R_0\approx 0$, one has $G(\mathbf{r},\mathbf{r}')\approx 1/(4\pi R_0)$. This singular term is fully contained in the $n=0$ term in the spatial sum in (33), since $\text{erfc}\left(R_n\mathcal{E}\pm j\frac{k}{2\mathcal{E}}\right)\approx\text{erfc}\left(\pm j\frac{k}{2\mathcal{E}}\right)$, and $\text{erfc}\left(+j\frac{k}{2\mathcal{E}}\right)+\text{erfc}\left(-j\frac{k}{2\mathcal{E}}\right)=2$ [64].

4.2.5 Asymptotic Convergence of G_{spectral} and G_{spatial}

The convergence properties of G_{spectral} and G_{spatial}, in (28) and (33), respectively, are analyzed here. First we derive the so called "optimum" Ewald splitting parameter $\mathcal{E}_0$, and then we show that in some specific important cases this choice leads to a high-frequency breakdown.

4.2.6 The Optimum Ewald Splitting parameter $\mathcal{E}_0$

In the spectral sum G_{spectral}, for large q, we can approximate $k_{zq}\approx 2\pi|q|/d$ and $k_{\rho q}\approx -j(2\pi|q|/d)$. By using the large argument asymptotic expansion for the exponential integral $E_{p+1}(z)\sim e^{-z}/z$, the qth term of the series in (28) is asymptotically approximated for large q as

$$\sim e^{-j2\pi qz/d}\frac{e^{-(\rho\mathcal{E})^2}}{4\pi d}\frac{e^{-(\frac{\pi q}{\mathcal{E}d})^2}}{(\frac{\pi q}{\mathcal{E}d})^2} \tag{34}$$

which exhibits Gaussian q-convergence. In the spatial sum G_{spatial}, for large n, we can approximate $R_n\approx|n|d$, and the two error functions in G_{spatial} are approximated by their asymptotic expansion for large argument as in the text after (21). Thus, the nth term of the series in (33) is asymptotically approximated for large n as

$$\sim e^{-jk_{z0}nd}\frac{\mathcal{E}\,e^{(\frac{k}{2\mathcal{E}})^2}}{4\pi^{3/2}}\frac{e^{-(n\mathcal{E}d)^2}}{(n\mathcal{E}d)^2} \tag{35}$$

which exhibits Gaussian n-convergence. When truncating the two series in (28) and (33) as $\sum_{q=-Q}^{Q}$ and $\sum_{n=-N}^{N}$, respectively, resulting in a total number of terms $2Q+1$ and $2N+1$, the optimum Ewald splitting

parameter $\mathcal{E}_0$, minimizes the total number $(2Q+1)+(2N+1)$ of necessary q,n-terms.

The total number of terms needed is determined by observing that to obtain roughly the same number of significant digits of accuracy in each sum in (28) and (33), the asymptotic approximation of their terms in (34) and (35), respectively, must have the same exponential factor $e^{-\sigma^2}$, and thus we set $(Q\pi)^2/(\mathcal{E}d)^2 = (N\mathcal{E}d)^2 \equiv \sigma^2$. The minimum number of terms needed to achieve this accuracy is thus $M^{tot} = 2\sigma[1/(\mathcal{E}d) + \mathcal{E}d/\pi] + 2$. The optimum $\mathcal{E}_0$ parameter is obtained by imposing $\partial M^{tot}/\partial\mathcal{E} = 0$, which leads to

$$\mathcal{E}_0 = \frac{\sqrt{\pi}}{d}. \tag{36}$$

We note that the choice of the optimum splitting parameter $\mathcal{E} = \mathcal{E}_0$ results in both series, G_{spectral} in (28) and G_{spatial} in (33), converging asymptotically with identical Gaussian convergence rates, $\sim \exp(-\pi q^2)$ and $\sim \exp(-\pi n^2)$, respectively.

4.2.7 The High-Frequency Breakdown of the Ewald Representation

At high frequencies (large k), some of the leading terms in the Ewald representation in both series (28) and (33) can become very large but nearly cancelling, not only causing loss of accuracy but also leading to overflow errors. In particular, exponentially large terms arise from the low-q terms in the spectral sum G_{spectral} in (28) that correspond to radially propagating Floquet waves (those with *real* $k_{\rho q}$). Without loss of generality we suppose that the array is phased with a real k_{z0} and that it is in a lossless free space. The $q = 0$ term has the largest value of $k_{\rho q}$, as is often the case. The exponential integrals related to the $q = 0$ term can be approximated as

$$E_{p+1}\left(\frac{-k_{\rho 0}^2}{4\mathcal{E}^2}\right) \sim \frac{4\mathcal{E}^2}{k_{\rho 0}^2} e^{\frac{k_{\rho 0}^2}{4\mathcal{E}^2}} \tag{37}$$

which causes numerical instability when the argument $k_{\rho 0}^2/(4\mathcal{E}^2)$ is very large. These large numbers tend to cancel a large number arising from the spatial G_{spatial} in (33), with a resulting loss of significant figures. The largest counterpart terms in the spatial sum G_{spatial} in (33) is provided by the two erfc functions in (33) that asymptotically behave like

$$\begin{aligned} &\left[e^{jkR_n}\operatorname{erfc}\left(R_n\mathcal{E} + j\frac{k}{2\mathcal{E}}\right) + e^{-jkR_n}\operatorname{erfc}\left(R_n\mathcal{E} - j\frac{k}{2\mathcal{E}}\right)\right] \\ \sim\ &\frac{1}{\sqrt{\pi}} e^{k^2/(4\mathcal{E}^2) - R_n^2\mathcal{E}^2}\left[\frac{2R_n\mathcal{E}}{(R_n\mathcal{E})^2 + k^2/(4\mathcal{E}^2)}\right]. \end{aligned} \tag{38}$$

The appropriate index n in (38) is that which minimizes R_n (often $n = 0$) because the large growth $e^{k^2/(4\mathcal{E}^2)}$ is compensated by $e^{-R_n^2\mathcal{E}^2}$ when R_n is large. It should be noticed that this numerical instability arises from the Ewald splitting and is not physical. The sum of the large numbers arising from the spectral and spatial splitting of course analytically leads to the correct results, but numerically may result in loss of accuracy or overflow. Thus at high frequencies, we have a loss of precision due to cancellation of large numbers when summing G_{spectral} and G_{spatial} in (18). The cancellation problem may be avoided by requiring that $k_{\rho 0}^2/(4\mathcal{E}^2) < H^2$ in the spectral sum, and that $k^2/(4\mathcal{E}^2) - R_0^2\mathcal{E}^2 < H^2$ in the spatial sum, where H^2 is the maximum exponent permitted. This leads to

$$\mathcal{E} \ > \ \mathcal{E}_{\text{spectral}} \equiv \frac{k_{\rho 0}}{2H} \le \frac{k}{2H} \equiv \mathcal{E}_{\text{HF}} \tag{39}$$

$$\mathcal{E} \ > \ \mathcal{E}_{\text{spatial}} \equiv \frac{H}{\sqrt{2}R_0}\left(\sqrt{1 + \frac{k^2R_0^2}{H^4}} - 1\right)^{1/2} < \mathcal{E}_{\text{HF}}. \tag{40}$$

Under the approximations $k_{z0} \ll k$ and $kR_0 \ll H^2$ we have $\mathcal{E}_{\text{spectral}} \approx \mathcal{E}_{\text{HF}} \approx \mathcal{E}_{\text{spatial}}$. The fact that $\mathcal{E}_{\text{spectral}}$ and $\mathcal{E}_{\text{spatial}}$ have different expressions suggests that an algorithm where these large numbers are numerically stabilized a priori (mixing spectral and spatial terms) is not straightforward, and is considered beyond the

scope of this work.

If one desires to use the optimum parameter $\mathcal{E}_0$ in (36) (that minimizes the number of terms) with the constraint that the largest computed values in G_{spectral} and G_{spatial} are smaller than e^{H^2} that may cause loss of accuracy, one should also impose that $\mathcal{E}_0 \geq \mathcal{E}_{\text{HF}}$. For example, if we require $H^2 = 6$ we need $\mathcal{E} > \mathcal{E}_{\text{HF}} \approx k/4.9 \approx 1.28/\lambda$. In other words, for $H^2 = 6$, the choice of the optimum parameter $\mathcal{E} = \mathcal{E}_0$ is a good choice if $d < 1.38\lambda$.

Even though the exponential growth is limited by the choice $\mathcal{E} > \mathcal{E}_{\text{HF}}$, in order to have a computationally efficient algorithm we also require the p-sum in (28) to be rapidly convergent. From $(p-1)p^{-1}\,E_p(x) < E_{p+1}(x) < E_p(x)$ [64, Eq. (5.1.17), p. 229] we infer that the exponential integral does not decay significantly with p, and indeed, except for $x \ll p$ and large p, $E_p(x) \approx e^{-x}/p$ [64, Eq. (5.1.19), p. 229]. Thus convergence of (28) relies on having $(\rho\mathcal{E})^{2p}/(p+1)!$ negligible for $p \geq P$, i.e., $(\rho\mathcal{E})^{2P}/(P+1)! < \epsilon$, with ϵ the desired error and P the number of p-terms necessary to achieve convergence (typically 10 to 15). This implies that

$$\mathcal{E} < \mathcal{E}_{\text{Taylor}} \equiv \frac{[\epsilon(P+1)!]^{\frac{1}{2P}}}{\rho}. \tag{41}$$

For example, if we require $\epsilon = 10^{-6}$, and $P = 15$, we have $\mathcal{E} < \mathcal{E}_{\text{Taylor}} \approx 1.75/\rho$ that has to be considered jointly with (36). In other words, the optimum parameter in (36) can be used if $\mathcal{E}_0 < \mathcal{E}_{\text{Taylor}}$ which is, for the numerical example just given, equivalent to imposing that the Ewald sum be used up to $\rho < 1.75d/\sqrt{\pi} \approx d$. Thus for high frequencies, or equivalently for large interelement spacings $d > \lambda$, the constraint (40) forces a choice of $\mathcal{E}$ other than "optimum" (36). We therefore suggest choosing

$$\mathcal{E} = \max\{\mathcal{E}_0, \mathcal{E}_{\text{HF}}\} = \max\left\{\frac{\sqrt{\pi}}{d}, \frac{k}{2H}\right\} \tag{42}$$

for the $\mathcal{E}$ parameter in (28) and (33) whose expressions can be used for the GF evaluation up to a distance ρ determined by (41).

When the frequency is sufficiently high that the Ewald parameter has to be chosen as $\mathcal{E} = \mathcal{E}_{\text{HF}}$, one should use the Ewald algorithm under the condition $\mathcal{E}_{\text{HF}} < \mathcal{E}_{\text{Taylor}}$, which is equivalent to $\rho/\lambda < [\epsilon(P+1)!]^{1/2P}\,H/\pi$ that may further restrict the radial distance ρ where the Ewald sum is accurate.

4.2.8 Numerical Results: Convergence

Various examples describe the convergence behavior of the two sums (28) and (33), for G_{spectral} and G_{spatial}, respectively, of the Ewald splitting (18). In all cases that follow, the linear array is phased, i.e., $k_{z0} = 0.1k$ and the $n = 0$ point source is at $(\rho', z') = (0, 0)$.

In Figure 60 we analyze the convergence rate of the Ewald sums using the percent relative error defined as

$$\text{Err} = |G^{exact} - G^{Ewald}|/|G^{exact}| \times 100, \tag{43}$$

where G^{exact} is the GF reference solution evaluated via its spectral counterpart (12) with a sufficiently large number of terms to achieve accuracy up to eight decimal digits, and G^{Ewald} is the same GF evaluated using the Ewald splitting (18) with (28) and (33). For the case $\rho = 0$, the spectral series (12) cannot be used, and the reference solution is evaluated with 10^8 terms of the spatial series (9). The percentage relative error is plotted versus summation limit parameters $\pm Q$ and $\pm N$ employed in sums (28) and (33), respectively (in particular, $-Q \leq q \leq Q$, and $-N \leq n \leq N$), resulting in a total number of terms of $2P+1$ and $2N+1$. The three curves are related to three observation points at $\rho = 0.0$, $\rho = 0.01d$, or $\rho = 0.1d$, all with $z = 0.1d$, where d is the period, which is set to $d = 0.05\lambda$ or $d = 0.5\lambda$, with $\lambda = 2\pi/k$ the free space wavelength. The Ewald splitting parameter is chosen as $\mathcal{E} = \mathcal{E}_0$ given in (36). A large total number $P = 20$

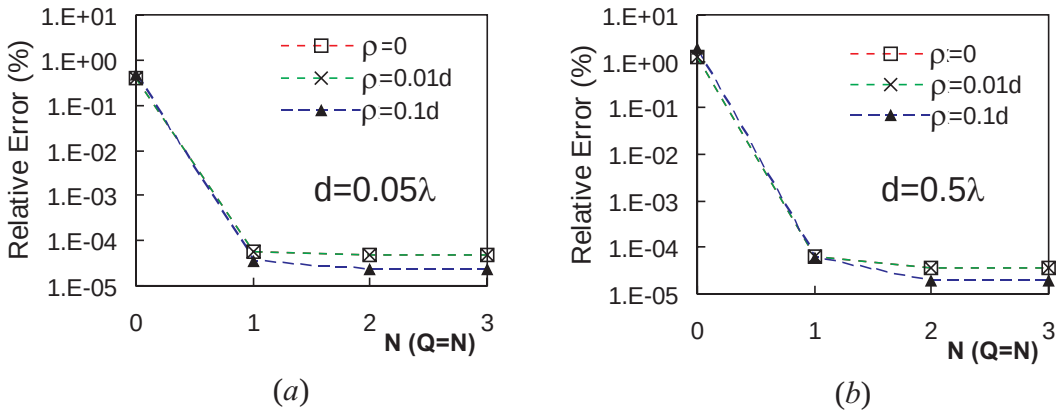

Figure 60. Convergence of the Ewald sums in (18) with (28) and (33) evaluated at three observation points with $\rho = 0.0,\ 0.01d,\ 0.1d$ and $z = 0.1d$. Percentage relative error versus number of terms N ($Q = N$) in the sums for two cases with period $d = 0.05\lambda$ and $d = 0.5\lambda$. Curves for $\rho = 0$ and $\rho = 0.01d$ are superimposed.

of p-terms in (28) has been used because we emphasize here convergence issues related only to N and Q.

Figure 60 shows that just a few terms, $Q = 1$ and $N = 1$, provide six digits of accuracy. The relative error cannot be further decreased by augmenting the number of terms Q, N in G_{spectral}, G_{spatial} because of the accuracy limits of the numerical subroutines that evaluate the error functions in G_{spatial} and the exponential integral $E_1(x)$ in G_{spectral} (see [65] for erfc(x), and [64, Secs. 5.1.53, 5.1.56] for $E_1(x)$). Note that in both cases in Figure 60 the period d is smaller than the wavelength, and that accepting exponential factors of the order of e^{H^2} with $H^2 = 9.6$, i.e., with roughly six digits of accuracy, implies $\mathcal{E}_{\text{HF}} = k/6.2 = 1.01/\lambda$. According to (36), for $d = 0.05\lambda$ and $d = 0.5\lambda$, the optimal Ewald parameter is $\mathcal{E}_0 = 35.4/\lambda$ and $\mathcal{E}_0 = 3.54/\lambda$, respectively, and thus in both cases we have $\mathcal{E}_0 > \mathcal{E}_{\text{HF}}$ justifying the use of the optimum Ewald parameter $\mathcal{E}_0$.

To gain an idea of the exceptional convergence rate of the Ewald representation, independent of the accuracy error of the evaluation of the special functions $E_1(x)$ and erfc(x), Figure 61 shows the rate of convergence of the two individual series G_{spectral} and G_{spatial} in (28) and (33), respectively, evaluated at the location $\mathbf{r} = (\rho, z) = (0.1, 0.1)d$ (we have checked that the case with $z = 0.1d$ would lead to analogous results). The relative error is defined as

$$\text{Err}_{\text{ spectral, spatial}} = \frac{|G^{Ewald,exact}_{\text{ spectral, spatial}} - G^{Ewald,P,M}_{\text{ spectral, spatial}}|}{|G^{Ewald,exact}_{\text{ spectral, spatial}}|} \times 100, \tag{44}$$

where $G^{Ewald,exact}_{\text{spectral, spatial}}$ is either G_{spectral} or G_{spatial} evaluated with a sufficient number of terms to achieve high numerical accuracy. The error is plotted versus the summation limit parameters $\pm Q$ and $\pm N$ employed in the sums in G_{spectral} and G_{spatial}, respectively. The array is the same as that in Figure 60(b), i.e., $d = 0.5\lambda$. The convergence rate is shown for three different choices of the Ewald splitting parameter $\mathcal{E}$. Note that the optimum parameter $\mathcal{E} = \mathcal{E}_0$ leads to the same convergence rate for both G_{spectral} and in G_{spatial} (Figure 61(b)), and the two series need the *same* number of terms to achieve the same accuracy. It is remarkable that so few terms are required to achieve high accuracy. For $\mathcal{E} < \mathcal{E}_0$ the spectral sum in G_{spectral} converges more rapidly than the sum in G_{spatial}. Vice versa for $\mathcal{E} > \mathcal{E}_0$, as predicted by the asymptotic expansion of the spectral and spatial sums in (34) and (35), respectively.

To determine the number P of necessary p-terms used in the Taylor expansion in (25), the percentage

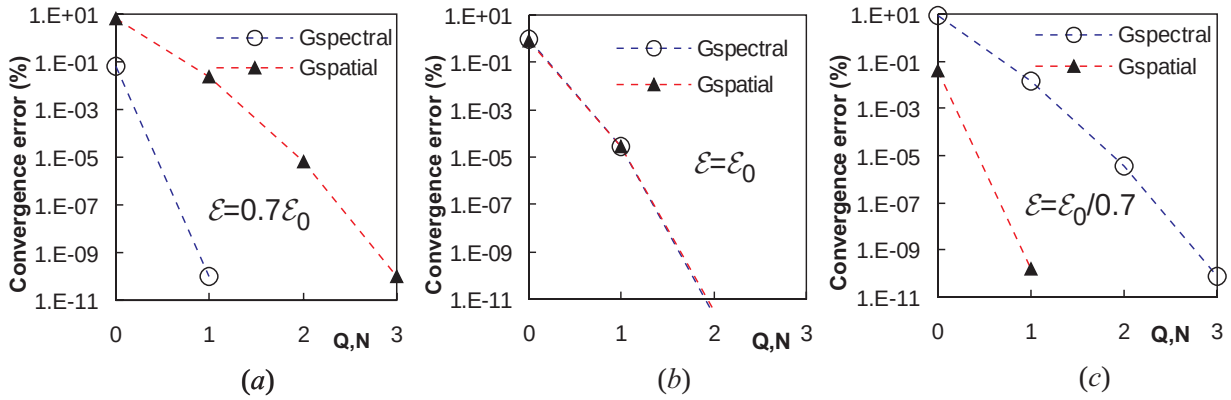

Figure 61. Convergence of the two individual series G_{spectral} and G_{spatial} in (28) and (33) for various choices of the splitting Ewald parameter $\mathcal{E}$.

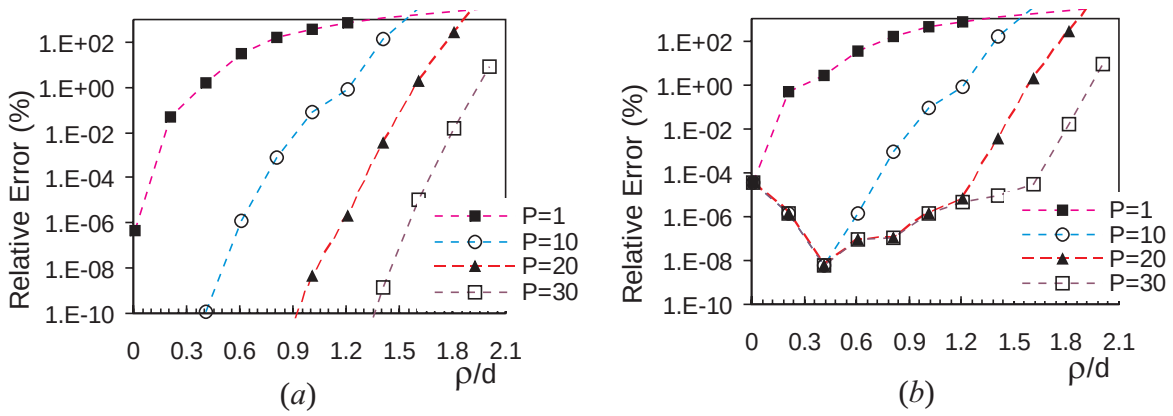

Figure 62. Convergence versus the number of terms P of p-sum in (28) for observation points ranging from $\rho = 0.01d$ to $0.2d$. The period is $d = 0.5\lambda$. (a) percentage relative error (44) of the spectral sum (28) where the reference solution is still evaluated using (28) with $P = 60$. (b) percentage relative error (43) of the Green's function G in (18) with (12) as reference solution.

relative error of the spectral part (28) of the Ewald representation is plotted in Figure 62(a) versus the radial distance ρ of the observation point from the array axis. The number of Ewald terms in (28) is kept equal to $Q = 2$, which is enough to guarantee good accuracy as shown in Figure 60. The relative error in Figure 62(a) is defined using as reference solution the same expression (28) evaluated with a large number $P = 60$ of p-terms. A larger number P of terms is necessary for larger distances ρ from the array axis. We observe that in Figure 62(a), $P = 20$ is satisfactory for good accuracy such as $10^{-4}\%$ until $\rho = 1.3d$. In Figure 62(b), for the same settings of Figure 62(a), we plot instead the percentage relative error of (18) with (28) and (33) (with $Q = N = 2$), taking as reference the spectral representation (12) of the GF, which is not affected by the accuracy limits of the numerical subroutines that evaluate the exponential integral $E_1(x)$ in (28) and the error functions erfc(x) in (33). This is why in Figure 62(b) the accuracy never falls below a certain value (determined by the accuracy limits of erfc(x) and $E_1(x)$) even for small ρ. Note that for $P = 20$ the accuracy becomes $10^{-4}\%$ at $\rho \approx 1.3d$. The trend is in accordance with the reasoning that led to (41). Repeating that discussion with $P = 20$, with a truncation error $\epsilon = 10^{-6}$, we would have $\mathcal{E}_{\text{Taylor}} = 2.2/\rho$, and the condition (41) is equivalent to $\rho < 1.24d$.

4.2.9 Extension to High Frequency

In Figure 63(a) the frequency is further increased such that $d = 5.5\lambda$ and the high frequency breakdown problem described in Section 4.2.7 occurs. In this case we cannot choose the optimum parameter $\mathcal{E} = \mathcal{E}_0$. Indeed, if we did, we would have $k/(2\mathcal{E}_0) = \sqrt{\pi}d/\lambda = 9.75$ in (33), yielding terms on the order of e^{95} that would cause overflow or at least loss of accuracy. The Ewald splitting parameter $\mathcal{E}$ must therefore be chosen according to (42). The rate of convergence of the two series in (28), (33) is then different, and more terms ($Q > N$) in G_{spectral} (28) are needed in order to maintain the same relative error in both (28) and (33). The convergence rates of the spectral and spatial sums of the Ewald representation are reported in (34) and (35), respectively. In Figure 63(a) the error is plotted versus N, with $Q = 4N$. Note that again a few terms are necessary (N=2 and Q=8) to provide a good accuracy. The error cannot further decrease than that for N=3 and Q=12 by augmenting the number of terms Q, N in G_{spectral}, G_{spatial} because of the accuracy limits of the numerical subroutines that evaluate the error functions and the exponential integral.

Figure 63(b) shows the rate of convergence of the two individual series G_{spectral} and G_{spatial} in (28) and (33), respectively, evaluated at the location $(\rho, z) = (0.1, 0.1)d$. The relative error is defined as in (44). The two series in G_{spectral} and G_{spatial} need *different* numbers of terms to achieve the same accuracy since we

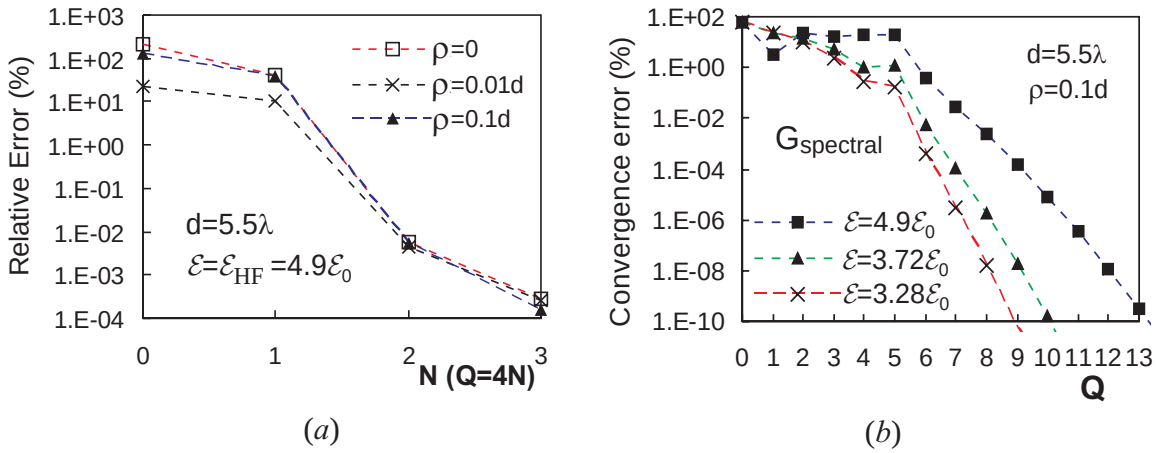

Figure 63. High frequency case (period larger than the wavelength: here, $d = 5.5\lambda$.) (a) Percentage relative error (43) versus number of terms N ($Q = 4N$). (b) Convergence rates for individual series G_{spectral} and G_{spatial}, in (28) and (33), respectively. One term ($n = 0$) in G_{spatial} is sufficient for excellent accuracy. In this case the choice of the optimum parameter $\mathcal{E} = \mathcal{E}_0$ would cause numerical errors, as explained in Section 4.2.7. Three different choices of the E parameters are analyzed here. Increasing the ratio $\mathcal{E}/\mathcal{E}_0$ results in a larger number of terms in $G_{spectral}$ to reach convergence. A smaller ratio $\mathcal{E}/\mathcal{E}_0$ would decrease the number of necessary terms in G_{spectral} but would result in a loss of accuracy.

have chosen $\mathcal{E} = \mathcal{E}_{\mathrm{HF}} > \mathcal{E}_0$. The spatial series G_{spatial} needs only the $n = 0$ term and it is accurate enough to be off the scale of the plot; hence only the number Q of terms in the spectral series G_{spectral} is given. The error in Figure 63(b) does not decrease significantly before $Q = 6$ because for this case ($d = 5.5\lambda$) spectral terms with $|q| \leq Q = 6$ are propagating and must be accounted for to obtain an accurate evaluation of the spectral part of the Ewald representation.

Note that the larger the Ewald parameter, the greater the number of terms needed to achieve the same accuracy. The three cases with $\mathcal{E} = \mathcal{E}_{\mathrm{HF}}$, are relative to $\mathcal{E}_{\mathrm{HF}} = 1.05/\lambda = 3.28\mathcal{E}_0$, $\mathcal{E}_{\mathrm{HF}} = 1.19/\lambda = 3.72\mathcal{E}_0$ and $\mathcal{E}_{\mathrm{HF}} = 1.57/\lambda = 4.9\mathcal{E}_0$, where the optimum parameter (not so optimum in this case) is $\mathcal{E}_0 = 0.32/\lambda$. According to (42), these cases correspond to choosing $H = 3, 2.64$ and 2, respectively. Clearly, as described in Section 4.2.7, choosing a larger H (i.e., smaller $\mathcal{E}_{\mathrm{HF}}/\mathcal{E}_0$) bounds the growth of the number of terms in G_{spectral}. Unfortunately, H cannot be chosen too large because it would generate values on the order of e^{H^2}. It should also be noted that choosing $\mathcal{E} = \mathcal{E}_{\mathrm{HF}}$, with decreasing $H = 3, 2.64, 2$, automatically implies that the maximum values in the series G_{spectral} and G_{spatial} become smaller. For an array with $d = 5.5\lambda$, values of $H > 3$ (i.e., $\mathcal{E}_{\mathrm{HF}}/\mathcal{E}_0 < 3.28$) would already cause a small loss of accuracy, while $H < 2$ (i.e., $\mathcal{E}_{\mathrm{HF}}/\mathcal{E}_0 > 4.9$) would require too many terms in the G_{spectral} sum.

4.2.10 Conclusions for 1d Array of Point Sources

The Green's function (GF) for a linearly-phased, 1d array of point sources has been expressed in terms of two series that exhibit Gaussian convergence as shown in Section 4.2.6. A description of the convergence properties, the analysis of the "high frequency breakdown" of the Ewald representation, and its remedy, have been analyzed theoretically and with the help of numerical experiments.

It is important to note that the purely spectral representation of the GF (12), besides being much slower than the Ewald representation, cannot be evaluated for $\rho = 0$, which is a very typical situation encountered when analyzing periodic structures of 3D elements with 1D periodicity. In this particular case ($\rho = 0$) the spatial representation in (9) (sum of spherical waves, which is in general even slower than the spectral representation in (12)) can still be used, rendering the Ewald method even more desirable. When it is required to evaluate the Green's function for complex phasings, the spatial representation cannot be evaluated because it would diverge (as well as the spectral method for $\rho = 0$), while the Ewald method can be evaluated also in this case. The Ewald representation is particularly useful for small ρ, while for large ρ (of the order of a period), one can use the well known spectral GF in (12) that is rapidly converging in this particular situation. Automatic optimal switching between these two representation for a given accuracy is beyond the scope of this work and will be investigated in the future, as well as an automatic algorithm for deciding the number of terms to be used in the series, as was done in [66] for the Ewald representation discovered in [46].

We are still in the process of adding the Green's function for the 1d array of point sources to EIGER. Until this is done, we can't solve the general seam problem. Once we have the code, we may want to approximate the terms $< T, E^s\left(J_{pa}\left(x\right)\right) >$ and $< T, E^s\left(J_{pa'}\left(x\right)\right) >$ on the right hand side of Equation 8 using a high frequency asymptotic approximation. Since the enforcement of the boundary condition all occurs in the plane of the array we need an expression for the field that is valid there. This is discussed next.

4.3 Approximation of Summation

The asymptotic form of the dipole semi-infinite array is considered on the plane without sources some distance from the edge. Time dependence $e^{j\omega t}$ is suppressed and the interelement spacings are d_x and d_z in the x and z directions. The exact integral representation is given by

$$\underline{E}\left(\underline{r}\right)=\frac{1}{4\pi d_z}\sum_{q=-\infty}^{\infty}\int_{-\infty}^{\infty}\frac{\overrightarrow{G}\left(k_x,k_{yq},k_{zq}\right)}{1-e^{jd_x\left(k_x-\gamma_x\right)}}e^{-j\left(k_xx+k_{yq}y+k_{zq}z\right)}\frac{dk_x}{k_{yq}}$$

$$\overrightarrow{G}\left(k_x,k_y,k_z\right)=\frac{\zeta}{k}\left(\widehat{x}k_xk_z+\widehat{y}k_yk_z+\widehat{z}\left(k_z^2-k^2\right)\right)$$

$$k_{\rho q}=\sqrt{k^2-k_{zq}^2}$$

$$k_{zq}=\gamma_z+\frac{2\pi q}{d_z},\ q=0,\pm1,\pm2,\pm3,...$$

$$k_{yq}=\sqrt{k^2-k_x^2-k_{zq}^2}$$

where γ_xd_x and γ_zd_z are the interelement phase advances in the x and z directions and $\zeta=\sqrt{\mu_0/\varepsilon_0}$ is the free space impedance. The integration contour is deformed above the poles of the integrand and below the branch point at $-k_{\rho q}$, but above the branch point at $+k_{\rho q}$.

Letting

$$k_x=k_{\rho q}\cos\alpha$$

$$k_{yq}=k_{\rho q}\sin\alpha$$

gives

$$\overrightarrow{E}\left(\overrightarrow{r}\right)=\frac{1}{4\pi}d_x\sum_{q=-\infty}^{\infty}\int_{C_\alpha}\overrightarrow{D}_q\left(\alpha\right)e^{-j\left[k_{\rho q}\rho\cos(\alpha-\varphi)+k_{zq}z\right]}d\alpha$$

$$x=\rho\cos\varphi$$

$$y=\rho\sin\varphi$$

$$\overrightarrow{D}_q\left(\alpha\right)=\frac{\overrightarrow{G}\left(k_{\rho q}\cos\alpha,k_{\rho q}\sin\alpha,k_{zq}\right)}{1-e^{jd_x\left[k_{\rho q}\cos\alpha-\gamma_x\right]}}$$

$$\alpha_{pq}=\arccos\left(\frac{\gamma_x+2\pi p/d_x}{k_{\rho q}}\right)=\arccos\left(\frac{k_{xp}}{k_{\rho q}}\right)$$

$$k_{ypq}=\sqrt{k^2-k_{xp}^2-k_{zq}^2}=k_{\rho q}\sin\alpha_{pq}$$

4.3.1 Asymptotic Expansion of Field

The field is written in terms of a sum of contributions from the residues of Floquet waves (FW) and a

sum of diffraction terms corresponding to the Floquet waves

$$\overrightarrow{E}(\overrightarrow{r}) \sim \sum_{p,q=-\infty}^{\infty} \overrightarrow{E}_{pq}^{FW}(\overrightarrow{r})\, U\left(\varphi_{pq}^{SB} - \varphi\right) + \sum_{q=-\infty}^{\infty} \overrightarrow{E}_{q}^{d}(\overrightarrow{r})$$

where

$$\overrightarrow{E}_{pq}^{FW}(\overrightarrow{r}) = \frac{1}{2d_x d_z k_{ypq}} \overrightarrow{G}(k_{xp}, k_{ypq}, k_{zq})\, e^{-j(k_{xp}x + k_{zq}z + k_{ypq}y)}$$

$$\overrightarrow{G}(k_x, k_y, k_z) = \frac{\zeta}{k}\left(\widehat{x}k_x k_z + \widehat{y}k_y k_z + \widehat{z}\left(k_z^2 - k^2\right)\right)$$

and

$$\overrightarrow{E}_{q}^{d}(\overrightarrow{r}) = \int_{SDP} \overrightarrow{D}_q(\alpha)\, e^{-j[k_{\rho q}\rho\cos(\alpha-\varphi) + k_{zq}z]} d\alpha$$

$U(\varphi)$ is the unit step function truncating the Floquet waves when the particular pole lies on the steepest descent path (SDP) and the corresponding observation angle is at the shadow boundary. The shadow boundaries for the propagating Floquet waves (PFW) and evanescent Floquet waves (EFW) are

$$\varphi_{pq}^{SB} = \alpha_{pq} = \arccos\left(\frac{k_{xp}}{k_{\rho q}}\right) \text{ for real } k_{ypq}\,(PFW)$$

$$\varphi_{pq}^{SB} = \arccos\left(\frac{k_{\rho q}}{k_{xp}}\right) \text{ for imaginary } k_{ypq}\,(EFW) \text{ and real } k_{\rho q}$$

$$\varphi_{pq}^{SB} = \frac{\pi}{2} \text{ for imaginary } k_{ypq}\,(EFW) \text{ and imaginary } k_{\rho q}$$

Note that $0 \le \varphi \le \pi$ (the extension is obtained from symmetry arguments).

4.3.2 Diffraction Terms

The evaluation of the diffraction terms is now given. First the function

$$\overrightarrow{W}_q(\alpha) = \sum_{p=-P}^{P} \left[\overrightarrow{w}_{pq-}(\alpha) + \varepsilon_p \overrightarrow{w}_{pq+}(\alpha)\right],\ \varepsilon_p = \operatorname{sgn}(k_{xp})$$

where

$$\overrightarrow{w}_{pq\mp}(\alpha) = \frac{-1}{2jk_{ypq}d_x} \frac{\overrightarrow{G}(k_{xp}, \pm k_{ypq}, k_{zq})}{\sin\left(\left(\alpha_{pq} \mp \alpha\right)/2\right)}$$

is subtracted from the integrand function $\overrightarrow{D}_q(\alpha)$ with which it shares the same poles and residues. In addition the integral of the function $\overrightarrow{W}_q(\alpha)\, e^{-jk_{\rho q}\rho\cos(\alpha-\varphi)}$ can be expressed in the closed form on the SDP. Note that the poles extracted include not only those associated with the physical PFW and EFW, but also those associated with improper waves whose presence may influence the behavior of the integrand. In particular $w_{pq+}(\alpha)$ contains the improper poles. This leads to the asymptotic form

$$\overrightarrow{E}_q^d(\overrightarrow{r}) \sim \frac{1}{4\pi d_z}\sqrt{\frac{2\pi j}{k_{\rho q}\rho}}e^{-j(k_{\rho q}\rho+k_{zq}z)}$$

$$\left[\overrightarrow{T}_q(\varphi)+\sum_{p=-P}^{P}\left\{\overrightarrow{w}_{pq-}(\varphi)F\left(\delta_{pq-}^2\right)+\varepsilon_p\overrightarrow{w}_{pq+}(\varphi)F\left(\delta_{pq+}^2\right)\right\}\right]$$

and

$$\overrightarrow{T}_q(\alpha)=\overrightarrow{D}_q(\alpha)-\overrightarrow{W}_q(\alpha)$$

This result can be rearranged as

$$\overrightarrow{E}_q^d(\overrightarrow{r}) \sim \frac{1}{4\pi d_z}\sqrt{\frac{2\pi j}{k_{\rho q}\rho}}e^{-j(k_{\rho q}\rho+k_{zq}z)}$$

$$\left[\overrightarrow{D}_q(\varphi)+\sum_{p=-P}^{P}\left\{\overrightarrow{w}_{pq-}(\varphi)\left(F\left(\delta_{pq-}^2\right)-1\right)+\varepsilon_p\overrightarrow{w}_{pq+}(\varphi)\left(F\left(\delta_{pq+}^2\right)-1\right)\right\}\right]$$

The error function F is the transition function of the UTD

$$F(x)=2\sqrt{x}e^{jx}\int_{\sqrt{x}}^{\infty}e^{-jt^2}dt \text{ with } -\frac{3\pi}{2}<\arg(x)\leq\frac{\pi}{2}$$

whose arguments are given by

$$\delta_{pq\pm}=\sqrt{2k_{\rho q}\rho}\sin\left(\frac{\alpha_{pq}\pm\varphi}{2}\right)$$

Note that

$$F\left(\delta^2\right)=\pm\sqrt{\pi}e^{j\pi/4}\delta e^{j\delta^2}\operatorname{erfc}\left(\pm e^{j\pi/4}\delta\right),\ \operatorname{Re}\left(e^{j\pi/4}\delta\right)\ \begin{matrix}>\\<\end{matrix}\ 0$$

We can also write

$$F\left(\delta^2\right)=\sqrt{\pi}e^{j\pi/4}\delta e^{j\delta^2}\left[\operatorname{erfc}\left(e^{j\pi/4}\delta\right)-2U\left(-\operatorname{Re}\left(e^{j\pi/4}\delta\right)\right)\right]$$

4.3.3 Evaluation

We are interested here in evaluating the expression near the plane surface $\varphi=0,\pi$.

$$\delta_{pq\pm}=\sqrt{2k_{\rho q}\rho}\sin\left(\frac{\alpha_{pq}\pm\varphi}{2}\right)$$

$$\overrightarrow{E}_q^d(\overrightarrow{r}) \sim \frac{1}{4\pi d_z}\sqrt{\frac{2\pi j}{k_{\rho q}\rho}}e^{-j(k_{\rho q}\rho+k_{zq}z)}$$

$$\left[\overrightarrow{D}_q(\varphi)+\sum_{p=-P}^{P}\left\{\overrightarrow{w}_{pq-}(\varphi)\left(F\left(\delta_{pq-}^2\right)-1\right)+\varepsilon_p\overrightarrow{w}_{pq+}(\varphi)\left(F\left(\delta_{pq+}^2\right)-1\right)\right\}\right]$$

$$\overrightarrow{D}_q(\alpha)=\frac{\overrightarrow{G}\left(k_{\rho q}\cos\alpha,k_{\rho q}\sin\alpha,k_{zq}\right)}{1-e^{jd_x\left[k_{\rho q}\cos\alpha-\gamma_x\right]}}$$

$$\overrightarrow{w}_{pq\mp}(\alpha)=\frac{-1}{2jk_{ypq}d_x}\frac{\overrightarrow{G}\left(k_{xp},\pm k_{ypq},k_{zq}\right)}{\sin\left(\left(\alpha_{pq}\mp\alpha\right)/2\right)}$$

$$k_{\rho q}=\sqrt{k^2-k_{zq}^2}$$

$$k_{zq}=\gamma_z+\frac{2\pi q}{d_z},\ q=0,\pm1,\pm2,\pm3,...$$

$$k_{ypq}=\sqrt{k^2-k_{xp}^2-k_{zq}^2}=k_{\rho q}\sin\alpha_{pq}$$

$$\alpha_{pq}=\arccos\left(\frac{\gamma_x+2\pi p/d_x}{k_{\rho q}}\right)=\arccos\left(\frac{k_{xp}}{k_{\rho q}}\right)$$

$$F(x)=2j\sqrt{x}e^{jx}\int_{\sqrt{x}}^{\infty}e^{-jt^2}dt\ \text{with}\ -\frac{3\pi}{2}<\arg(x)\le\frac{\pi}{2}\ ,\ -\pi<\arg(jx)<\pi\ ,\ -\frac{\pi}{2}<\arg\sqrt{jx}<\frac{\pi}{2}$$

$$\sqrt{\pi jx}\left[e^{jx}\text{erfc}\left(\sqrt{jx}\right)\right]=\sqrt{\pi jx}e^{jx}\frac{2}{\sqrt{\pi}}\int_{\sqrt{jx}}^{\infty}e^{-t^2}dt$$

$$=\sqrt{jx}e^{jx}2\int_{e^{j\pi/4}\sqrt{x}}^{e^{j\pi/4}\infty}e^{-t^2}dt=2j\sqrt{x}e^{jx}\int_{\sqrt{x}}^{\infty}e^{-jt^2}dt=F(x)$$

4.4 Array Approach to the Seam Problem

As stated in Section 2.2 a common approximation for calculating the field due to a truncated array is to truncate the infinite periodic current at the edge of the patch. The edge is assumed not to affect the current distribution. We found in Section 4.1 that if two patches are brought together to form a seam, the difference current between the actual current and the truncated infinite current approximation is quite small (see Figure 56). Therefore, it appears that a valid approximation for the seam is to truncate the infinite current solution for each patch and use superposition to calculate the field due to these currents. Since under this approximation a given patch doesn't affect the current distribution on surrounding patches, we can treat them as if they are independent truncated patches and use the techniques developed to solve the truncation problem. For example, if we are interested in the far-field of a group of patches with a current we could use array theory [67]. The magnetic vector potential due to an electric current in the far field is given by

$$\overrightarrow{A}\approx\frac{e^{-jkr}}{4\pi r}\int J(r')\,e^{jk\hat{r}\cdot\overrightarrow{r}'}dr'$$

where $\overrightarrow{r}'$ is the variable that describes the source location and $\overrightarrow{r}$ describes the observation point. The

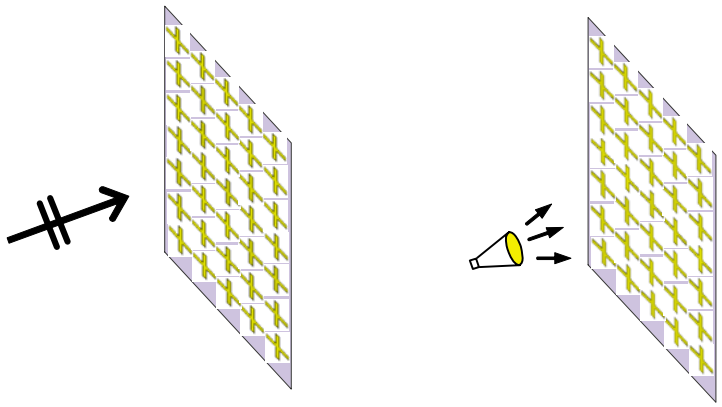

Figure 64. FSS illuminated by a plane wave or by a beam source

electric field is related to the vector potential by

$$\begin{aligned} E_\theta &= -j\omega\mu A_\theta \\ E_\phi &= -j\omega\mu A_\phi \end{aligned}$$

If the current on every element of a patch are identical except for a complex constant (I_n) – a phase progression, for example – then we can write the field due to the patch as

$$E_\theta = \frac{-j\omega\mu e^{-jkr}}{4\pi r}\left[\int J_\theta\left(r'\right) e^{jk\hat{r}\cdot\overrightarrow{r}'} dr'\right]\left[\sum_{n-1}^{N} I_n e^{jk\hat{r}\cdot\overrightarrow{r}_n}\right] \tag{45}$$

where $\overrightarrow{r}_n$ the location of the reference point of each element and N is the number of elements on the patch. The expression for E_ϕ has a similar form. The second factor of Equation 45 (the integral) is the pattern for a single element of the array and the third factor (the summation) is the array factor. This means that the far-field for the patch can be computed using a single integration over one of the elements and a simple summation over the N elements in the array. The far-field for a number of patches is a sum of the field from each patch. A further simplification is to use a high frequency expansion like Capolino [21],[23] to calculate the array factor. This reduces the number of summation terms from N per patch (typically on the order of a million) to nine per patch. This method is taken up in the following section for truncated arrays. The diffraction from a seam is a sum of the two truncated edges diffraction contributions bearing in mind that the angle to the observation point are supplementary angles for the two edges.

4.5 High Frequency Approach to the Seam Problem

In this section, we consider a truncated FSS and an FSS having a seam. The scattered fields produced by the edges in such surfaces are described by diffraction phenomena, whose effects are highlighted here. We first consider an FSS illuminated by a plane wave, as shown in Figure 64. It should be noted that the discussion that follows can also, in principle, be applied to the case of an incident field produced by proximate antennas or beam sources, assuming that the FSS is in the far field of the radiating antenna or beam source (this restriction may also be removed with a more detailed analysis). For the case of an incident plane wave, we consider an observation point in the near field of the FSS structure.

The diffraction effects from the edges of the truncated periodic structures are the same as those for a PEC plate. The effect of the periodic elements is to weight the amplitude of the various ray species that arise from the edges and the corners of the FSS, relative to the simple PEC contributions. For example, the

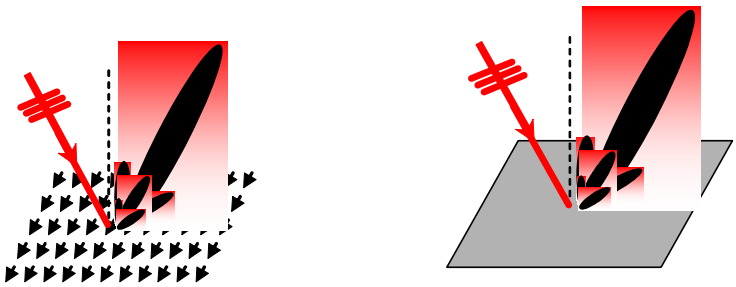

Figure 65. Two equivalent problems from a phenomenological point of view

scattered beam in the far field of the two structures shown in Figure 65 is comprised of the same physical constituents. (The same holds true in the near field.) The phenomenological behavior arising in both cases is shown in Figure 66 where a plane wave impinging on a flat and finite FSS generates a specularly reflected field plus fields diffracted from the edges and corners of the FSS. These same ray contributions would arise from a plane wave impinging on a flat PEC surface.

Solving the associated integral equations and then evaluating the field radiated by the induced currents on the FSS structure yields the diffracted ray contributions. As discussed previously in Section 4.4, a good approximation of the radiated field is obtained by evaluating the currents on an infinite periodic structure and then evaluating their radiation contribution assuming they exist only on the finite surface of the FSS (via a windowing procedure). Therefore, we assume that the currents are the same on every FSS cell, except for the relative phase differences in the periodic elements dictated by the plane wave angle of incidence. In the far field this procedure is equivalent to determining the element radiation pattern of an FSS element and multiplying it by the array factor (AF) of the planar FSS of finite size. In the near field this approximation leads to diffracted rays that can be expressed in simple form. The accuracy of this approximation is equivalent to that of a physical optics (PO) approximation compared to the evaluation of the field by using the Uniform Theory of Diffraction (UTD). The PO solution, and its asymptotic approximation, are very good estimates in the forward and backward regions but loses accuracy when the field is evaluated on the plane containing the finite structure (either a flat PEC plate or a flat FSS). For optical fields, or for very high frequencies, the PO approximation is generally satisfactory.

4.5.1 Ray Field Constituents

The field expressions associated with the diffracted rays are evaluated by solving two canonical problems with impressed dipole currents. The physical situation, along with the two canonical problems, are shown in Figure 67. This kind of Green's function, often called an Array Green's Function (AGF), is useful to determine the field produced by a more general set of currents, like those on a FSS, via the procedure explained below. This same field formalism can be applied to the case of a FSS illuminated by a more general field, such as a beam, as long as the incident field does not vary rapidly along the surface of the FSS. In this case, the wave species are simply weighted by the local amplitude of the incident field.

Omitting the details, the total field expression at a finite distance from the FSS can be expressed as

$$\vec{E}^{tot} \sim \sum_{p,q} \vec{E}^{FW}_{pq} \bar{U}_{pq} + \sum_{i=1}^{4} \left(\sum_{u} \vec{E}^{d,i}_{u} U^{0}_{u} U^{L}_{u} \right) + \sum_{i=1}^{4} \vec{E}^{v,i}$$

where the individual field contributions are given by

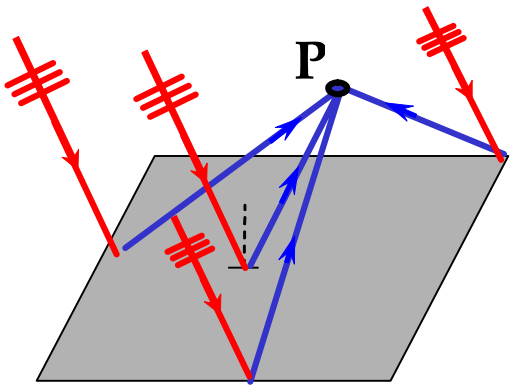

Figure 66. A plane wave impinging on a flat FSS generates a reflected field and diffracted fields from the edges and corners of the FSS at the observation point P.

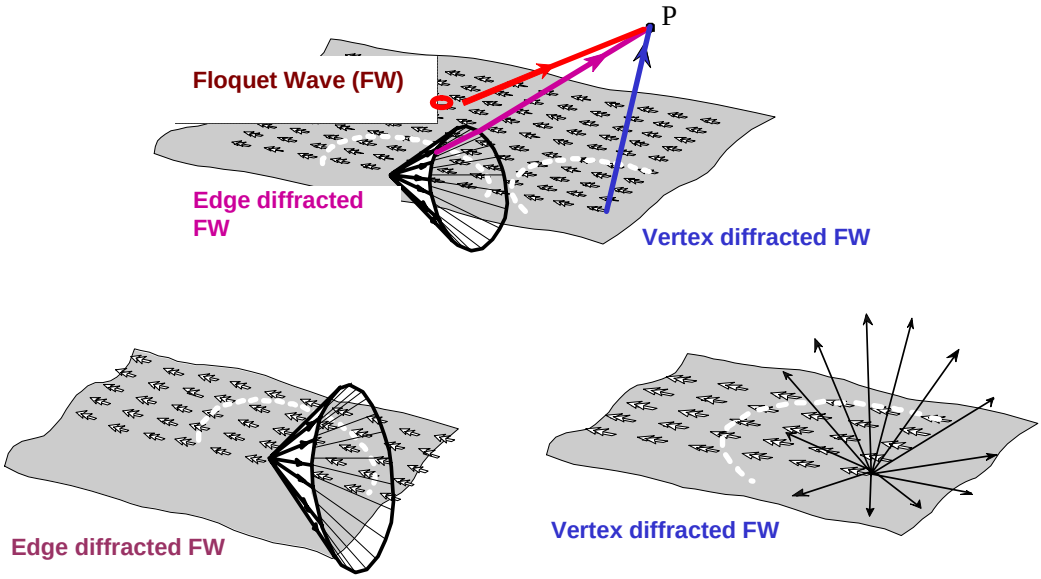

Figure 67. The three wave species, the reflected field, the edge diffracted field, and corner (or vertex) diffracted field arriving at the observation point P. Also shown are the two canonical problems that can be used to determine the mathematical form of these ray contributions.

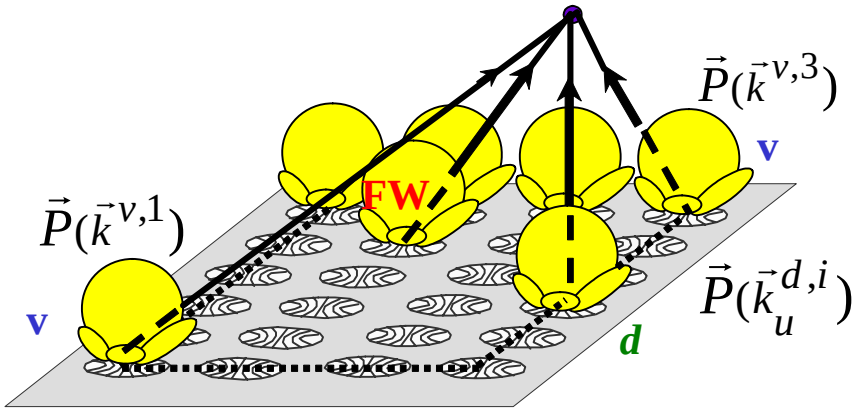

Figure 68. The three wave species that are to be multiplied by the radiation pattern of the elementary array element. The approximation described in the text (the PO approximation) results by assuming that all the element radiation patterns are alike.

$$\vec{E}_{pq}^{FW} = A_{pq}^{FW} \times \vec{P}(\vec{k}_{pq}^{FW})$$

$$\vec{E}_{u}^{d,i} = A_{u}^{d,i} \times \vec{P}(\vec{k}_{u}^{d,i})$$

$$\vec{E}^{v,i} = A^{v,i} \times \vec{P}(\vec{k}^{v,i})$$

In these expressions $\vec{E}$ represents the electric field, A is the scalar potential, and $\vec{P}$ is the radiated pattern from an elementary array element that includes the polarization information, as shown in Figure 68. The indices p,q indicate the various Floquet wave contributions, where here the sums are limited to the propagating-wave components. The U functions bound the domain of existence of the Floquet wave and of the edge diffracted waves, as usually found in ray-optics field representations. The wavenumbers used to evaluate the radiated element patterns of the pq-th Floquet wave are defined as

$$\vec{k}_{pq}^{FW} = k_{x,p}\hat{x} + k_{y,q}\hat{y} + k_{z,pq}\hat{z}$$

where $\vec{k}_u^{d,i}$ is the wavenumber of the diffracted fields (one from the each of the four edges, i=1,...,4), and $\vec{k}^{v,i}$ is the wavenumber of the corner diffracted fields (one from each of the four corners, i=1,...,4). In general, to represent the radiated fields far from a FSS surface with a period smaller than $\frac{1}{2}$ of the wavelength (a standard configuration), only one FW (p=q=0) and one edge diffracted field from each edge ($u = 0$) is necessary.

More specifically, the three wave species can be described by the following expressions.

$$A_{pq}^{FW} = \frac{1}{2jd_1d_2}\frac{e^{-j(\vec{k}_{pq}^{FW}\cdot r)}}{k_{z,pq}}$$

$$A_q^{d,1}\ \frac{e^{-j(\vec{k}_q^{d,1}\cdot r)}}{\sqrt{k_{\rho 1,q}\rho_1}} D_q^{d,1}$$

$$A^{v,1}\ \frac{e^{-jkr}}{r} D^{v,1}$$

Here we have highlighted the plane-wave behavior for the Floquet wave A_{pq}^{FW}, d_1 and d_2 are the two periods along $\widehat{x}$ and $\widehat{y}$, respectively. We have also highlighted the cylindrical and the spherical spreading factors for the edge and corner diffracted fields, whereas $D_q^{d,1}$ and $D^{v,1}$ represent the edge and corner diffraction coefficients that involve the transition function of the Uniform Theory of Diffraction, and a more complicated transition function for the corner diffraction coefficient. Further details can be found in [21] –[23] and are not given here due to space constraints.

We stress again that the above field description assumes that the current on all the FSS elements, illuminated by a plane wave, is the same excluding a phase factor dictated by the specific plane-wave excitation. In other words, we assume that all the array elements produce the same radiated fields. Elements near the edges (or near a seam between two FSS) would, in reality, have different currents, but the overall radiated field in the forward or backward direction is not significantly affected by these current modifications. This is examined in the numerical examples presented below.

4.5.2 Algorithm for the Field Evaluation

We provide here a simple way to approximate the radiated field produced by a truncated FSS for two illuminating conditions: a plane wave and a beam. (The case of a seam formed between two frequency-selective surfaces is analogous.) The approximation is as described above, in that all the FSS elements have the same current besides the phase differences dictated by the incident field.

Plane Wave Excitation

- The currents on an elementary cell (of the array) are found by a solver for periodic structures.
- The radiation pattern of an elementary array cell (a cell of the FSS) can be easily evaluated by using a Fourier transform of the array element current every time it is needed, or it is evaluated beforehand, sampled and then interpolated.
- For each of the 9 ray contributions (associated with 4 corners, 4 edges, and a reflected ray from the flat surface) that reach the observer at finite distance away, we evaluate the radiation pattern (one for each ray) as a function of the observation point. The radiation patterns are then multiplied by the ray field contributions.

Near Field Excitation (e.g., Horn Antenna)

- The direction of incidence of the various 9 rays (for rectangular FSS) are evaluated by a standard and simple ray tracing.
- For each of these 9 incidence angles, the currents on an elementary periodic FSS cell are evaluated by using a solver for periodic structures. Then, the 9 set of currents are stored.
- The 9 radiation patterns can be easily evaluated by using a Fourier transform of the array element current every time they are needed, or they are evaluated beforehand, sampled and then interpolated.
- For each of the 9 rays contributions that reach the observer (at finite distance) we evaluate the radiation pattern (one for each ray) that is a function of the direction of observation. The radiation patterns are then multiplied by the ray field contributions.

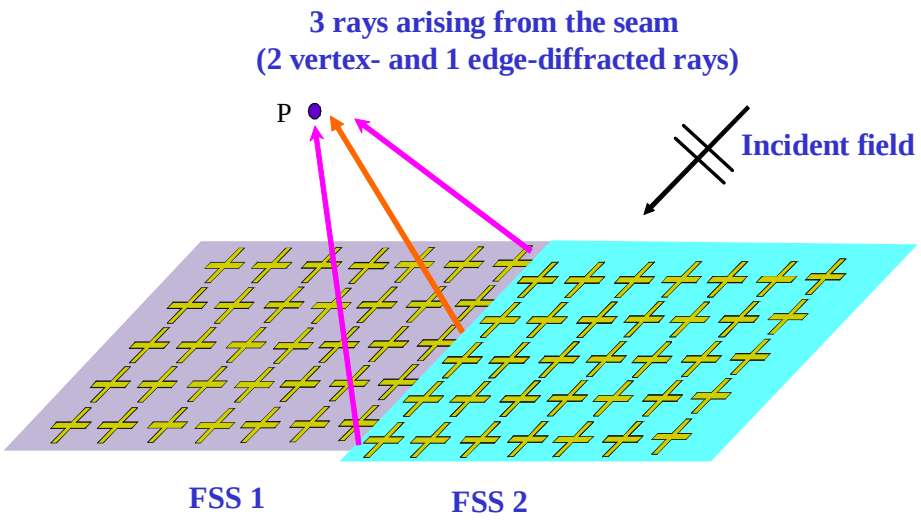

Figure 69. A seam between two frequency-selective-surfaces. Besides the standard reflected and transmitted field contributions associated with the FSS, three rays originate from the seam: one edge-like diffracted field and two vertex-like diffracted fields.

4.5.3 Seam Between Two Coplanar FSS Structures

We now suppose there is a plane wave illuminating two joined FSSs as shown in Figure 69. As discussed previously, besides the usual reflected or transmitted fields associated with the FSS, we have three additional wave species as shown Figure 69. These additional components of radiation are the edge-like diffracted fields described by a cylindrical-spreading function and two vertex-like diffracted fields characterized by a spherical-spreading behavior. This case is analogous to the one with a truncated FSS, but the field expressions are slightly different. In summary, the field produced by the seam is mainly a cylindrical wave arising from a point on the seam that obeys standard laws of geometrical theory of diffraction in terms of path minimization and so forth, plus two other spherical contributions. In the far field, the field produced by the seam can be expressed as a single radiation pattern, like that produced by a traveling wave current with the same length as the seam, and with an amplitude dependant on the geometry of the seam itself. The total amount of power transmitted by a seam between two FSS structures in the stop band has yet to be determined and would require further investigation. In the numerical results that follow we examine the diffraction effects associated with a finite array using the GIFFT technique [11].

4.5.4 The Field Produced by an Edge of a Periodic Structure

A square array of 50×50 PEC strip-dipoles is assumed to be illuminated by a unit-strength plane wave of normal incidence, with the electric field polarized along the length of the dipoles. The wavelength is assumed to be $\lambda = 1$ m and the unit cell of the array is shown in Figure 36.

The radiation pattern along the E-plane (the xz plane) is shown in Figure 70. The curve labeled "Physical Currents" refers to the radiated field produced by the actual current distribution obtained via the GIFFT method when applied to the 50×50 array. The curve "Infinite Array Currents" represents the radiated field produced by the 50×50 array assuming that each array element has the same current as in the infinite array case. This solution is based on multiplying the array factor by the dipole element pattern

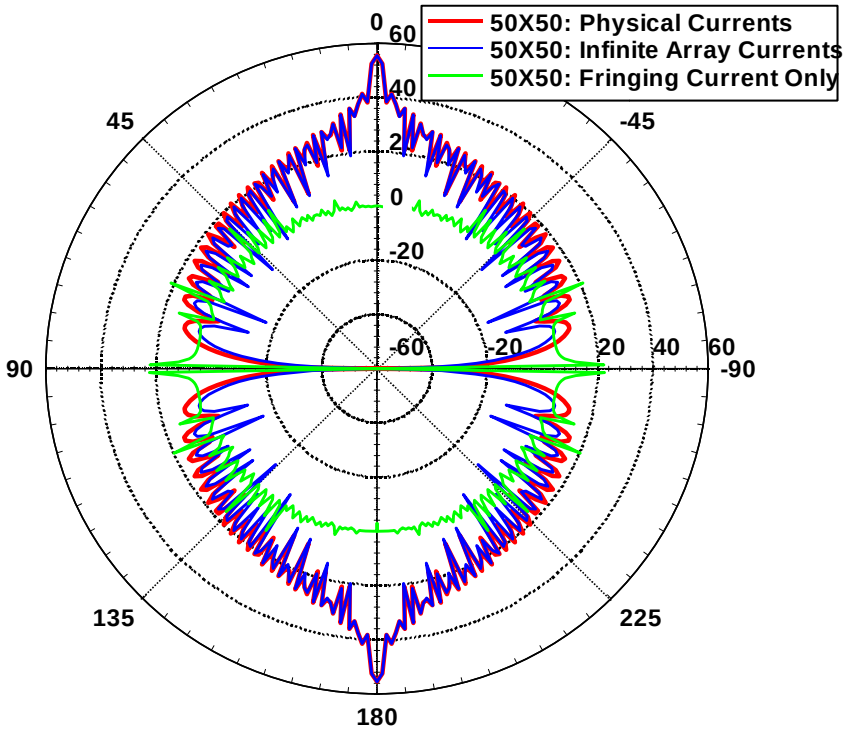

Figure 70. The far-field E-plane radiation pattern produced by the 50×50 dipole array.

in the infinite array environment. The curve labeled "Fringing Current Only" refers to the field produced by the 50×50 array when the strip-dipole elements contain currents equal to the difference between the actual current and the infinite array current solution. The fringing current is dominant near the array edges and tends to zero toward the center where the infinite array current is a good approximation, assuming that there are no surface waves excited in the periodic structure (as should be the situation in the present case). Figure 70 shows that the fringing current produces a negligible field effect away from the plane containing the array. Due to the fact that the fringe current is mainly comprised of a traveling wave with a wavenumber equal to that of free space (grazing propagation), the fringe effect is visible in the angular range between 70 and 90 degrees.. This example also demonstrates that away from grazing the "Infinite Array Currents" solution is an effective tool to predict the field since it avoids the need to grid the entire array.

The near-field behavior can be described in terms of a modified GTD (Geometrical Theory of Diffraction) ray theory, based on the Floquet-wave modulation of the diffraction coefficients [70]. To show this behavior, we plot the electric near field moving away from an edge along the observation scan shown in Figure 71. The observation scan is chosen in such a way to allow us to neglect the field arising from the four corners and the other three edges.

Figure 72 shows the electric field along the scan in Figure 71 produced by the three set of currents associated with the patterns in Figure 70. It is evident that they all decrease with the same trend when moving away from the edge. As already noted in Figure 70, the field produced by the "Fringing Currents Only" is significant at grazing. Along other angular directions this field contribution is in general smaller than the other two contributions in Figure 72. The small ripple may be associated with the diffraction effects due to the other edges and corners.

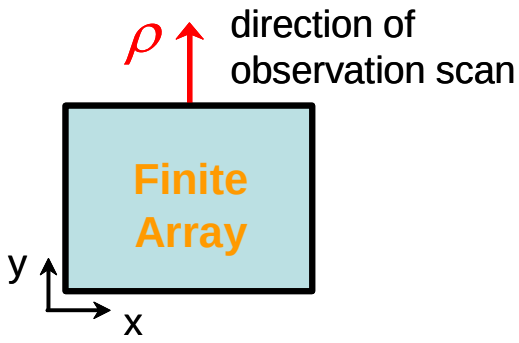

Figure 71. Direction of the observation scan used to highlight the edge-diffracted fields.

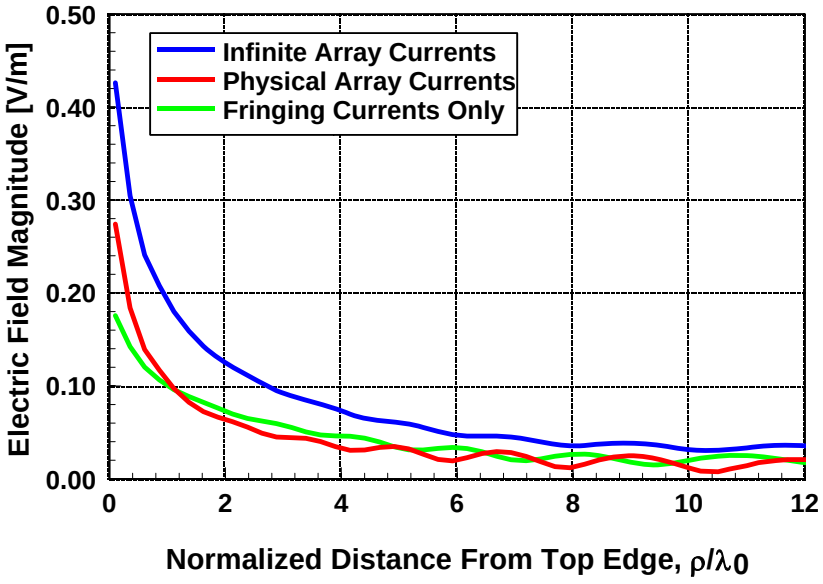

Figure 72. Diffracted field along the observation scan shown in Figure 71.

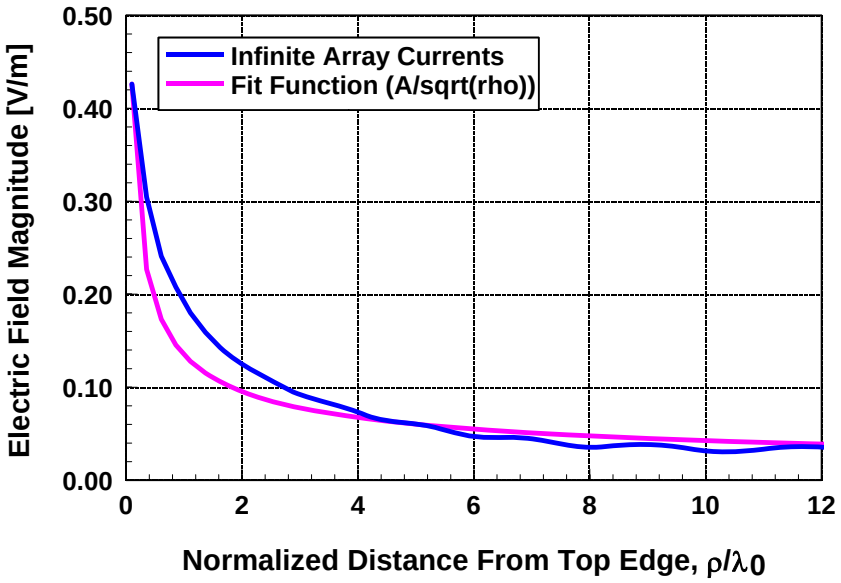

Figure 73. Fit of the diffracted field, along the observation scan of Figure 71, with the curve $\propto 1/\sqrt{\rho}$

Figure 73 shows that the behavior of the field produced by the "Infinite Array Current", evaluated as described previously, is well represented by the trend $1/\sqrt{\rho}$, multiplied by a proper constant that depends on the observation angle (the diffraction coefficient) as predicted in [21] and [22]. Also the field produced by the "Physical Array Currents" exhibits the same geometrical decay $1/\sqrt{\rho}$ away from the edge but its multiplicative constant is different and cannot be simply predicted by the simple model in [21] and [22]. Therefore, in most angular directions the near field produced by the array can be approximated by the field produced by the infinite array current solution and its ray description.

4.5.5 The Field Produced by a Seam Between Two Periodic Structures

A seam in the periodic structure is realized by splitting the 50×50 array in two parts and shifting one part to the other with respect to the $\widehat{y}$ axis as shown in Figure 74. For this preliminary case we show that the presence of the seam does not significantly affect the far field pattern as shown in Figure 75. In addition we show the field difference between the two cases is always negligible except for near grazing. We expect to observe a more significant field difference (associated with the seam effect) for more dramatic misalignments. We also expect the field near the seam to be of the order of $1/\sqrt{\rho}$, where ρ is the radial distance from the seam, when the observation point is positioned far from the two end points of the seam, so that their effect can be neglected. This could also be predicted by deriving a proper seam-diffraction coefficient, which has yet to be developed. The two end points of the seam produce two spherical scattered waves that can be described by appropriate diffraction coefficients, which are also yet to be developed.

4.5.6 Conclusions and Future Work on Seams

1. Repeat the simulations in Figures 72 and 73 for varying observation angles about the edge to confirm the general trend of $1/\sqrt{\rho}$, where ρ is the radial-cylindrical distance from the seam. The observation scan in this case should be far from the end points of the seam to highlight the $1/\sqrt{\rho}$ field decay.
2. The field produced by the end points should decay as $1/r$, where r is the radial-spherical distance from the end point of the seam. This behavior could be highlighted by looking at the difference field along proper observation scans with an origin at the end point of the seam. It is important to note that in

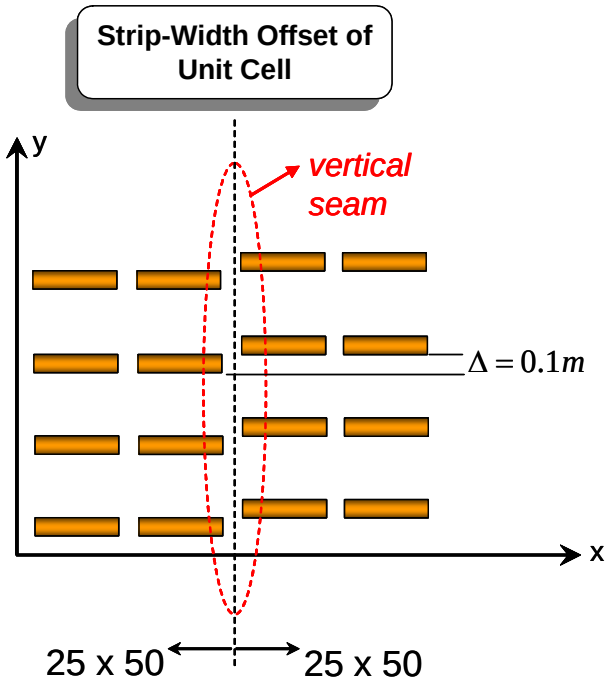

Figure 74. A seam created by a junction between two periodic structures.

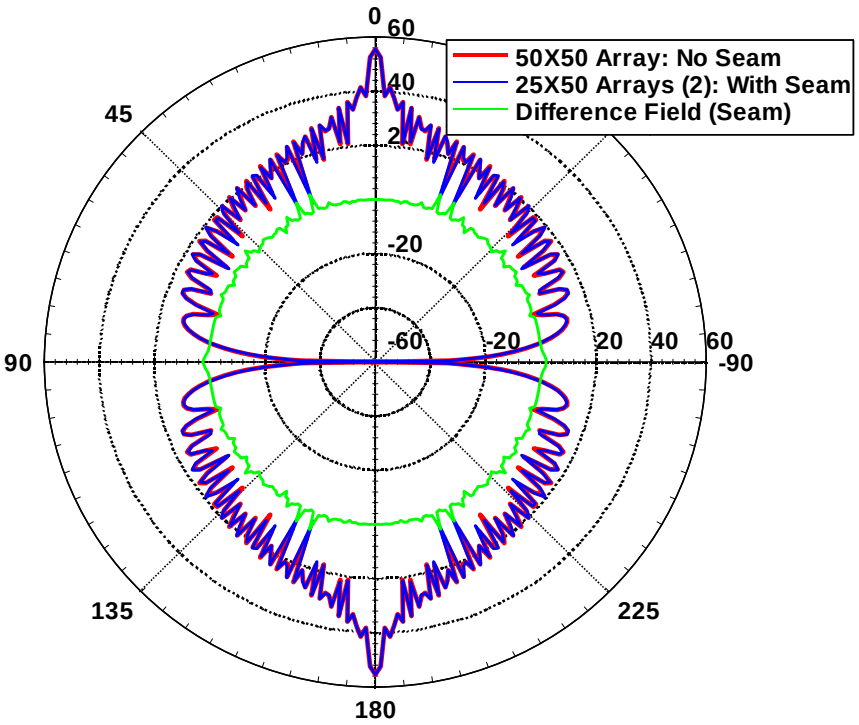

Figure 75. The far-field E-plane radiation patterns produced by a vertical seam in a 50×50 array

practical designs the end points are present and the estimation of effects in this finite array environment (where all the effects are combined) could provide valuable information to the FSS designer.

3. Determine the diffraction coefficient associated with the seam by fitting the numerical results with theoretical predictions.
4. An efficient tool to isolate the seam effect is the linear-array Green's function (see Section 4.2) that allows the modeling of periodic structures that are infinitely long along the $\widehat{y}$ axis, thus removing the end point effects. Since the numerical burden of the problem is that of only one row (along $\widehat{x}$), very wide structures (along $\widehat{x}$) could be easily modeled. This work is currently being carried out via the implementation of the linear array Green's function into EIGER.
5. The simulation of a finite array with one or more defects is easily handled by GIFFT. Using GIFFT, we could estimate the total amount of power that passes through a seam of a particular FSS.
6. Further development is needed in GIFFT to model an FSS where current can flow across unit cell boundaries. At present, current unknowns are confined to reside within a unit cell.

5 Conclusions

In this LDRD we have looked at various techniques to analyze structures that depart from periodicity. We examined single point defects, truncations and seams. A general statement is that compared to the specular reflection or transmission, the scattering from breaks in periodicity plays a minor role. It is only if we are at an observation point where the specular is suppressed that the breaks in periodicity begin to contribute. Scattering from truncation seems to be greater than scattering from seams, which seems to be greater than scattering from a single defect.

We modified GIFFT to handle two types of unit cells on the same periodic lattice. Using this we could analyze single defects (where one unit cell is different from all the rest) or a seam (where a group of half the unit cells differ from the other half). We used GIFFT to confirm the behavior of fields near a truncated edge as being the same as that calculated using diffraction. We are in the process of incorporating GIFFT into EIGER.

An isolated defect seems to be ignorable. If we want to modify the bandgap, it appears that we have to add a periodic defect which can be analyzed using the well-known periodic techniques with a unit cell that encompasses the new periodicity.

To complete the work started here we need to finish incorporating GIFFT and the 1D array of point sources in EIGER. We should then implement techniques in EIGER to analyze the 2d seam and compare to the other techniques developed here (GIFFT and the asymptotic high frequency solution). Both GIFFT and the one-dimensional seam problem indicate that the majority of the seam and truncation effect is modeled by truncating the infinite periodic solution. If that conclusion is unaltered after further testing, we can write software to analyze groups of these patches. Since the patches are all independent of each other, we can use superposition and the various approximations described in Sections 4.4 and 4.5.

6 References

[1] E. Yablonovitch, "Photonic crystals: semiconductors of light," *Scientific American*, pp. 47-55, December 2001.

[2] E. Yablonovitch, "Inhibited spontaneous emission in solid-state physics and electronics," *Physical*

Review Letters, vol. 58. no. 20, pp. 2059-2062, 18 May 1987.

[3] T. Cwik and R. Mittra, "Scattering from a periodic array of free-standing, arbitrarily shaped, perfectly conducting or resistive patches," *IEEE Trans. Antennas and Propagat.,* vol. 35, no. 11, pp. 1226-1234, Nov. 1987.

[4] Y. Rahmat-Samii and A. N. Tulintseff, "Diffraction analysis of frequency selective reflector antennas," *IEEE Trans. Antennas and Propagat.*, vol. 41, no. 4, pp. 476-487, April 1993.

[5] J. S. McCalmont, M. M. Sigalas, G. Tuttle, K. M. Ho and C. M. Soukolis, "A layer-by-layer metallic photonic band-gap structure," *Appl. Phys. Lett.*, vol. 68, no. 19, pp. 2759 - 2761, 6 May 1996.

[6] V. V. S. Prakash and R. Mittra, "Technique for analyzing cascaded frequency selective surface screens with dissimilar lattice geometries," *IEE Proc. Microw. Antennas Propagat.*, vol. 150, no. 1, pp. 23 - 27, February 2003.

[7] E. Yablonovitch, T. J. Gmitter, R. D. Meade, A. M. Rappe, K. D. Brommer and J. D. Jonnopoulos, "Donor and acceptor modes in photonic band structure," *Physical Review Letters*, vol. 67, no. 24, pp. 3380-3389, December 1991.

[8] J. B. Pendry, "Photonic band structures," *Journal of Modern Optics*, vol. 41, no. 2, pp. 209-229, 1994.

[9] M. L. Povinelli, S. G. Johnson, S. Fan and J. D. Joannopoulos, "Emulation of two-dimensional photonic crystal defect modes in a photonic crystal with a three-dimensional photonic band gap," *Physical Review B*, vol. 64, no. 7, article no. 075313, 2001

[10] R. Mittra, C. H. Chan and T. Cwik, "Techniques for analyzing frequency selective surfaces – a review," *IEEE Proc.*, vol. 76, pp. 1693-1615, Dec. 1988.

[11] B.J. Fasenfest, F. Capolino, D.R. Wilton, and D.R. Jackson, N. Champagne, "A fast MOM solution for large arrays: Green's function interpolation with FFT," *IEEE Antennas and Wireless Propagation Letters*, vol. 3, pp. 161-164, 2004.

[12] B. Fasenfest, *Fast Computation for Large Arrays*, Masters Dissertation, Univ. Houston, Houston, TX 2004

[13] E. Bleszynski, M. Bleszynski, and T. Jaroszewicz, "AIM: Adaptive integral method for solving large scale electromagnetic scattering and radiation problems," *Radio Science*, vol. 31, pp. 1225-1251, 1996.

[14] T. Cwik and R. Mittra, "The effects of the truncation and curvature of periodic surfaces: a strip grating," *IEEE Trans. Antennas and Propagat.*, vol. 36, no. 5, pp. 612-622, May 1988.

[15] W. L. Ko, and R. Mittra, "Scattering by a truncated periodic array," *IEEE Trans. Antennas and Propagat.*, vol. 36, no. 4, pp. 496-502, April 1988.

[16] K. O. Merewether and R. Mittra, "Spectral-domain analysis of a finite frequency-selective surface with cross-shaped conducting patches," *1988 International Symposium Digest: Antennas and Propagation*, vol.2, pp. 742-745, 1988.

[17] B. Philips, E. A. Parker, R. J. Langley, "Ray tracing analysis of the transmission performance of curved FSS," *IEE Proceedings on Microwave and Antennas Propagat.*, vol. 142, no. 3, pp. 193-199, June 1995.

[18] H. Ling, R. C. Chou, S. W. Lee, "Shooting and bouncing rays: Calculating the RCS of an arbitrarily shaped cavity," *IEEE Trans. Antennas and Propagat.*, vol. 37, no. 2, pp. 194-205, Feb. 1989.

[19] A. Ishimaru, R. J. Coe, G. E. Miller and W. P. Geren, "Finite periodic structure approach to large scanning array problems," *IEEE Trans. Antennas and Propagat.*, vol. 33, no. 11, pp. 1213-1219, Nov. 1985.

[20] L. Carin and L. B. Felsen, "Time harmonic and transient scattering by finite periodic flat strip arrays: Hybrid (ray)-(Floquet mode)-(MOM) algorithm," *IEEE Trans. Antennas and Propagat.*, vol. 41, no. 4, pp. 412-421, Apr. 1993.

[21] F. Capoliino, M. Albani, S. Maci, L. B. Felsen, "Frequency domain Green's function for a planar periodic semi-infinite phased array: Part I: Truncated Floquet wave formulation," *IEEE Transactions*

on Antennas and Propagation, vol. 48, no. 1, pp. 67-74, Jan. 2000.

[22] F. Capolino, M. Albani, S. Maci, and L.B. Felsen,"Frequency domain Green's function for a planar periodic semi-infinite phased array. Part II: Phenomenology of the diffracted waves," *IEEE Trans. Antennas and Propagation*, vol. 48, no.1, pp. 75-85, Jan. 2000.

[23] F. Capolino, S. Maci and L.B. Felsen, "Green's function for a planar phased sectoral array of dipoles," *Radio Science, Special Issue on the 1998 URSI Intern. Symp. on EM Theory*, vol. 35, no. 2, pp. 579-593, March-April, 2000.

[24] V. V. S. Prakash and R. Mittra, "Convergence studies of plane-wave spectral expansion technique for analyzing truncated frequency-selective surfaces," *Microwave and Optical Technology Letters*, vol. 34, no. 6, pp. 417-421, Sept. 20, 2002.

[25] A. Neto, S. Maci, G. Vecchi, and M. Sabbadini, "A truncated Floquet wave diffraction method for the full wave analysis of large phased arrays – Part I: Basic principles and 2-d cases," *IEEE Trans. Antennas and Propagat.*, vol. 48, no. 3, pp. 594-600, March 2000.

[26] A. Neto, S. Maci, G. Vecchi, and M. Sabbadini, "A truncated Floquet wave diffraction method for the full wave analysis of large phased arrays – Part II: Generalization to 3-d cases," *IEEE Trans. Antennas and Propagat.*, vol. 48, no. 3, pp. 601-611, March 2000.

[27] A. Cucini, M. Albani, S. Maci, "Truncated Floquet wave full-wave $\left(T\left(FW\right)^2\right)$ analysis of large periodic arrays of rectangular waveguides," *IEEE Trans. Antennas and Propagat.*, vol. 51, no. 6, pp. 1373-1385, June 2003.

[28] O. A. Civi, P. H. Pathak, H. T. Chou, P. Nepa, "A hybrid uniform geometrical theory of diffraction – moment method for efficient analysis of electromagnetic radiation/scattering from large finite planar arrays," *Radio Science*, vol. 35, no. 2, pp. 607-620, March-April 2000.

[29] B. A. Munk, D. S. Janning, J. B. Pryor and R. J. Marhefka, "Scattering from surface waves on finite FSS," *IEEE Trans. Antennas and Propagat.*, vol. 49 no. 12, pp. 1782-1792, Dec. 2001.

[30] M. P. Hurst, "Improved numerical diffraction coefficients with application to frequency selective surfaces," *IEEE Trans. Antennas and Propagat.*, vol. 40, no. 6, pp. 606-212, June 1992.

[31] G. Pelosi, G. Manara, G. Toso, "Heuristic diffraction coefficient for plane-wave scattering from edges in periodic planar surfaces," *J. Opt. Soc. Am. A*, vol. 13, no. 8, pp. 1689-1697, Aug. 1996.

[32] S. Q. Li, Y. Yu, C. H. Chan, K. F. Chan, and L. Tsang, "A sparse-matrix/canonical grid method for analyzing densely packed interconnects," *IEEE Trans. Microwave Theory Tech.*, vol. 49, no. 7, pp. 1221-1228, July 2001.

[33] L. Tsang, C. H. Chan, P. Kyung, H. Sangani, "Monte-Carlo simulations of large-scale problems of random rough surface scattering and applications to grazing incidence with the BMIA/canonical grid method," *IEEE Trans. Antennas and Propagat.*, vol. 43, no. 8, pp. 851-859, Aug. 1995.

[34] S. M. Seo, J.F. Lee, "A fast IE-FFT algorithm for solving PEC scattering problems," *IEEE Trans. on Magnetics*, vol. 41, no.5, pp. 1476-1479, May 2005.

[35] Mori, F. De Vita, A. Freni, "A modification of the canonical grid series expansion in order to increase the efficiency of the SMCG method," *IEEE Geoscience and Remote Sensing Letters*, vol. 2, no. 1, pp. 87-89, Jan. 2005.

[36] R. Coifman, V. Rokhlin, and S. Wandzura, "The fast multipole method for the wave equation: a pedestrian prescription," *IEEE Antennas Propagat. Mag.*, vol. 35, no 3, pp. 7-12, June 1993.

[37] W. C. Chew, J. M. Jin, C. C. Lu, E. Michielssen, J. M. Song, "Fast solution methods in electromagnetics," *IEEE Trans. Antennas and Propagat.*, vol. 45, no. 3, pp. 533 – 543, March 1997.

[38] J. Song, C.-C. Lu, W. C. Chew, "Multilevel fast multipole algorithm for electromagnetic scattering by large complex objects," *IEEE Trans. Antennas and Propagat.*, vol. 45, no. 10, pp. 1488 – 1493, Oct. 1997.

[39] R. W. Kindt and J. L. Volakis, "Array decomposition-fast multipole method for finite array analysis,"

Radio Science, vol. 39, RS2018, 2004

[40] S. M. Rao, D.R. Wilton, and A.W. Glisson, "Electromagnetic scattering by surfaces of arbitrary shape," *IEEE Trans. on Antennas and Propagat.*, vol. 30, no. 3, pp. 409-418, May 1982.

[41] A. Erentok, P. L. Luljak, and R. W. Ziolkowski, "Characterization of a volumetric meta-material realization of an artificial magnetic conductor for antenna applications," *IEEE Trans. Antennas and Propagat.*, vol. 53, no. 1, pp. 160-172, January 2005.

[42] W. A. Johnson, R. E. Jorgenson, L. K. Warne, J. D. Kotulski, J. B. Grant, R. M. Sharpe, N. J. Champagne, D. R. Wilton, and D. R. Jackson, "Our experiences with object-oriented design, FORTRAN 90, and massively parallel computations," *1998 Digest USNC/URSI National Radio Science Meeting, June 21-26, 1998, Atlanta, Georgia, Antennas: Gateways to the Global Network*, p. 308, 1998.

[43] L I. Basilio, W. A. Johnson, D. R. Jackson, and D. R. Wilton, "Numerical modeling of finite-size plasmon structures with enhanced optical transmission using EIGER," *Proceedings of Joint 9th International Conference on Electromagnetics in Advanced Applications ICEAA 2005 and 11th European Electromagnetic Structures Conference EESC 2005*, Torino, Italy, pp. 877- 880, Sept 12-16, 2005.

[44] C. R. Simovski, P. de Maagt, I. V. Melchakova, "High impedance surfaces having stable resonance with respect to polarization and incidence angle," *IEEE Transactions on Antennas and Propagat.*, vol. 53, no. 3, pp. 908-914, March 2005.

[45] P. P. Ewald, "Die berechnung optischer und elektrostatischen gitterpotentiale," *Ann. der Physik*, vol. 64, pp. 253–287, 1921. Translated by A. Cornell, Atomics International Library, 1964.

[46] K. E. Jordan, G. R. Richter, and P. Sheng, "An efficient numerical evaluation of the Green's function for the Helmholtz operator on periodic structures," *J. Comp. Physics*, vol. 63, pp. 222–235, 1986.

[47] D. R. Jackson D. R. Wilton and N. J. Champagne, "Efficient computation of periodic and nonperiodic Green's function in layered media using the MPIE," in *URSI Int. Symp. on Electrom. Theory*, Thessaloniki, Greece, May. 25-28. 1998.

[48] M. J. Park and S. Nam, "Efficient calculation of the Green's function for multilayered planar periodic structures," *IEEE Trans. Antennas Propagat.*, vol. 46, no. 10, pp. 1582–1583, October 1998.

[49] Y. X. Yu and C. H. Chan, "On the extension of Ewald's method to periodic structures in layered media," *Microwaves and Optical Techn. Lett.*, vol. 19, no. 2, pp. 125–131, 1998.

[50] D. Wang, E. K. N. Yung, R. S. Chen, D. Z. Ding, W. C. Tang, "On evaluation of the Green's function for periodic structures in layered media," *IEEE Antennas and Wireless Propagat. Lett.*, vol. 3, no. 1, pp. 133–136, Sept. 2004.

[51] A. W. Mathis and A. F. Peterson, "A comparison of acceleration procedures for the two-dimensional periodic Green's function," *IEEE Trans. Antennas Propagat.*, vol. 44, no. 4, pp. 567–571, April 1996.

[52] C. M. Linton, "The Green's function for the two-dimensional Helmholtz equation in periodic domains," *Journal of Engineering Mathematics*, vol. 33, pp. 377–402, 1998.

[53] F. Capolino, D. R. Wilton, and W. A. Johnson, "Efficient computation of the 2d Green's function for 1d periodic structures using the Ewald method," *IEEE Trans. Antennas Propagat.*, vol. 53, no.5, pp. 2977–2984, Sept. 2005.

[54] A. Moroz, "Exponentially convergent lattice sums," *Opt. Lett.*, vol. 26, pp.1119–1121, 2001.

[55] C. M. Linton, "Schlömilch series that arise in diffraction theory and their efficient computation," *Journal of Physics A*, vol. 39, pp. 3325–3339, March 2006.

[56] V. G. Papanicolaou, "Ewald's method revisited: rapidly convergent series representations of certain Green's functions," *Journal of Comp. Analysis and Appl.*, vol. 1, no. 1, pp. 105-114, 1999.

[57] E. Cohen, "Critical distance for grating lobe series," *IEEE Trans. Antennas Propagat.*, vol. 39, no. 5, pp. 677–679, May 1991.

[58] M. J. Park, J. Park, and S. Nam, "Efficient calculation of the Green's function for the rectangular cavity," *IEEE Microwave and Guided Wave Lett.*, vol. 8, no. 3, pp. 124–126, March 1998.

[59] F. Marliani and A. Ciccolella, "Computationally efficient expressions of the dyadic Green's function for rectangular enclosures," *Progress In Electromagnetics Research, PIER*, vol. 31, pp. 195-223, 2001.

[60] T. F. Eibert, J. L. Volakis, D. R. Wilton, D. R. Jackson, "Hybrid FE/BI modeling of 3-D doubly periodic structures utilizing triangular prismatic elements and an MPIE formulation accelerated by the Ewald transformation," *IEEE Trans. Antennas Propagat.*, vol. 47, no. 5, pp. 843–850, May 1999.

[61] M. Bressan, L. Perregrini, and E. Regini, "BI-RME modeling of 3D waveguide components enhanced by the Ewald technique," *IEEE MTT-S Int. Microwave Symp. Dig.*, vol. 2, pp. 1097-1100, 2000.

[62] A. Kustepely and A. Q. Martin, "On the splitting parameter in the Ewald method," *IEEE Trans. Microwave and Guid. Wave Lett.*, vol. 10, no. 5, pp. 168–170, May 2000.

[63] A. Papoulis, *Systems and Transforms with Application in Optics*, R.E. Krieger Pub. Co, Malabar, FL, 1981.

[64] M. Abramowitz and I.A. Stegun, *Handbook of Mathematical Functions*, Dover, New York, 1970.

[65] J. A. C. Weideman, "Computation of the complex error function," *SIAM J. Numer. Anal.*, vol. 31, no. 5, pp. 1497–1518, 1994.

[66] S. Oroskar, D. J. Jackson, D. R. Wilton, "Efficient computation of the 2d periodic Green's function using the ewald Method," *J. Comp. Physics*, in print, 2006.

[67] R. F. Harrington, *Time Harmonic Electromagnetic Fields*, McGraw-Hill: New York, pp.132-134, 1961.

[68] Y. T. Lo and S. W. Lee, *Antenna Handbook*, Van Nostrand Reinhold Company, New York, chapter 11, 1988.

[69] S. Maci, F. Capolino and L.B. Felsen, "Three-dimensional Green's function for truncated planar periodic dipole arrays," *Wave Motion – Special Issue on Electrodynamics in Complex Environments*, vol. 34, no. 3, pp. 263-279, Sept. 2001.

[70] F. Mariottini, F. Capolino, S. Maci and L.B. Felsen, "Floquet wave diffraction theory for tapered planar array Green's function," *IEEE Trans. Antennas and Propagat.*, vol. 53, no. 2, pp. 608-620, Feb. 2005.

Distribution:

1 Prof. Don R. Wilton
University of Houston
Department of Electrical and Computer Engineering
Houston, TX 77204-4005

1 Prof. Filippo Capolino
University of Houston
Department of Electrical and Computer Engineering
Houston, TX 77204-4005

1	MS1082	J. J. Hudgens, 01725
1	MS1082	D. W. Peters, 01727
1	MS1152	R. E. Jorgenson, 01652
1	MS1152	L. K. Warne, 01652
1	MS1152	L. I. Basilio, 01652
1	MS1152	W. A. Johnson, 01652
1	MS1152	M. L. Kiefer, 01652
2	MS9018	Central Technical Files, 08944
2	MS0899	Technical Library, 04536
1	MS0123	D. L. Chavez, 01011